UNIVERSITY OF CALIFORNIA,
IRVINE

Ultra-short Pulse Off-axis Digital Holography and Kerr Effect Ballistic Imaging in Highly Scattering Environments such as Formation Regions of Diesel Sprays

DISSERTATION

submitted in partial satisfaction of requirements
for the degree of

DOCTOR OF PHILOSOPHY

in Mechanical and Aerospace Engineering

by

Ali Ziaee

Dissertation Committee:
Professor Derek Dunn-Rankin, Chair
Professor Manuel Gamero-Castano
Professor Ali Mohraz

2016

DEDICATION

I dedicate my dissertation to my loving parents, Firouzeh Hajiaghaei and Naseh Ziaee without whose support and sacrifice I would not be able to accomplish this work.

TABLE OF CONTENTS

LIST OF FIGURES

LIST OF TABLES

ACKNOWLEDGMENTS

I would like to express my deepest appreciation to my committee chair and academic advisor, Professor Derek Dunn-Rankin, who trusted me with this challenging work despite my little experience in research and the topic at the time I started my journey at UC Irvine. I cannot imagine myself accomplishing this dissertation work without his generous support all through my graduate studies.

I would like to thank my committee members, Professor Ali Mohraz and Professor Manual Gamero-Castano, who kindly accepted to read and judge this dissertation.

Special thanks to MetroLaser Inc., Dr. James Trolinger, and Dr. Colin Dankwart who generously provided their scientific guidance and technical support to this research work.

In addition, a thank you to Dr. Alireza Mirsepassi, who introduced me to the Laser, Flames, and Aerosols Research Group and inspired me with his enthusiasm in optical sciences research.

I thank the National Science Foundation and the University of California, Irvine department of Mechanical and Aerospace Engineering for providing financial support to this research.

CURRICULUM VITAE

Ali Ziaee

2011 B.Sc. in Mechanical Engineering, Amirkabir University of Technology

2012 M.Sc. in Mechanical and Aerospace Engineering, University of California, Irvine

2012-13 Graduate Student Researcher, Lasers, Flames, and Aerosols Research Group

2015-16 Research and Development Engineer, Alcon Labs, Lake Forest, CA

2012-16 Teaching Assistant, University of California, Irvine

2016 Ph.D. in Mechanical and Aerospace Engineering, University of California, Irvine

FIELD OF STUDY

Laser Diagnostics and Digital Holographic Imaging in Multi-phase Flows

PUBLICATIONS

"Time gated holography to provide a glimpse into dense sprays." The international society of optics and photonics (SPIE) electronic newsroom, 2012.

"Picosecond Digital Holography for Multi-Phase Flows." Western States Section of the Combustion Institute, 2013.

"Time-Gated Digital Holography for Dense Sprays using Hydrosols." ILASS Americas 26th annual conference on Liquid Atomization and Spray Systems, Portland, OR, 2014.

"Femtosecond Kerr Effect Time-gated Digital Holography in Scattering Media." Laser Diagnostics in Combustion, Gordon Research Conference, 2015.

ABSTRACT OF THE DISSERTATION

Ultra-short Pulse Off-axis Digital Holography and Kerr Effect Ballistic Imaging in Highly Scattering Environments such as Formation Region of Diesel Sprays

By

Ali Ziaee

Doctor of Philosophy in Mechanical and Aerospace Engineering

University of California, Irvine, 2016

Professor Derek Dunn-Rankin, Chair

Liquid fuel injection in combustion systems involves multi-phase flows generated by fuel sprays. Studying the fluid mechanical phenomena integrated in these flows that influence the fuel's combustion, such as liquid jet break up into droplets, can benefit from experimental approaches for imaging them. Such information can help with design choices to control stability and increase the efficiency of combustion systems. However, the high optical scattering from the cloud of small droplets obscures traditional imaging methods. In addition, conventional imaging does not provide depth information that is often critical in spray understanding. Digital holography (DH) is a well-established and powerful technique for high-resolution 3D imaging. Monochromatic laser beams and digital cameras are used in this technique to record digital holograms (diffracted object wave interfered with the non-diffracted reference wave) of the 3D objects. The object field is then numerically reconstructed using the digital hologram recorded on a CCD detector but it is not clear how the light scattered from small particles, as in the spray situation, will complicate the hologram analysis. Consequently, the current work examines the use of

ultra-short laser pulses for digital holography in multi-phase flows of combustion interest. A state-of-the-art Ti-Sapphire amplified laser system is used, with pulses as short as 100 fs and up to 1mj per pulse energy. Using this system creates the opportunity for coherence filtering and time-gating filtering, which can improve signal-to-noise ratio in highly scattering media like dense sprays. In this work, scattering media with optical conditions similar to the condition in combusting dense sprays is replicated with hydrosols. USAF resolution chart is used as test target to demonstrate quantitatively the imaging resolution and contrast of the system. The atomizing spray diagnostics literature study shows that optical Kerr effect (OKE) time-gating is the only promising technique that has been demonstrated to image the liquid structure inside the transient diesel sprays. Experimental results presented in this dissertation show high potential of ultra-short pulse DH for microscopic imaging though highly scattering media with competitive resolution and quality compared to OKE time-gating, and holography provides the additional feature of resolving the internal structure of dense sprays in 3D. The technique can potentially image an intact liquid core of diesel sprays, veiled behind the optically deep cloud of droplets, which has never been done before.

INTRODUCTION

Fuel injection systems can play an important role in sustainable combustion of fossil fuels. For example, modifying the fuel injection process in power generating systems like diesel or gas turbine engines can increase the efficiency and stability of their combustion. Atomization and injection of liquid fuel into the combustion chamber of power generation systems produces a dense spray (Connon et al. 1996 and Kohse-Hoeinghaus et al. 2002). These sprays are formed when an injected liquid fuel jet breaks up into small droplets in several stages due to the instability which occurs at the interface of gas-liquid flow. The process is complex and so most practical device design relies on empirical correlations. Improved understanding is possible with the fluid mechanical theories that have been developed over many years to explain how the process of liquid jet break up into droplets and atomization occurs (e.g., Sirignano 1999). Experimental data is used to validate these theories, but some controversy remains, particularly regarding the presence of a liquid core in diesel sprays and similar injectors (Paciaroni 2004). This is partly because for most dense sprays it is not possible to look at the core liquid column while it is veiled behind the thick cloud of very small spray droplets surrounding the center column of the liquid. Photography and holography, which have been used for many years in such research (Trolinger et al. 1977 and Cai et al. 2003), have failed to provide clear views because optical noise from multiple scattering obscures the signal needed to acquire a useful recording (Trolinger et al. 2011). This dissertation aims to develop an optical imaging method based on short pulse laser holography to resolve this obscurity challenge.

Technically, the complexity of imaging the core jet is caused by the turbid characteristics of the surrounding cloud. Almost every photon of any imaging beam that penetrates this thick cloud is scattered many times by different droplets on its way out of the spray and therefore is no longer useful to construct an image of the core liquid jet. As a result, advanced imaging technologies need to be designed and developed for this specific application. Among different methods that are used, so called "ballistic imaging" has shown promising outcomes during many years of effort on imaging dense sprays. The idea of ballistic imaging is to make use of the statistically very few photons of the imaging beam that go through the dense spray without being scattered by the mist surrounding the core jet of the dense spray (ballistic photons). The difficulty is, however, that the population of this group of photons is very low (just a fraction of a percent even in the best cases) compared to the enormous number of multiply scattered photons. This causes abysmally low signal to noise ratio for imaging the liquid core. One solution to this problem is to somehow filter the object (imaging) beam in order to block the multiple scattered photons and increase the ratio of clean imaging photons to the noise. In order to accomplish this, we need to use specific characteristics of the ballistic photons that are different from the majority of multiple scattered photons. Two basic characteristics that can be used to filter out the multiple scattered photons are polarization and diffraction angle. Provided that the imaging beam is perfectly collimated before being diffracted by the spray, photons that are not diffracted at all or are just diffracted once or twice, deviate less than those photons scattered many times. Polarization of the multiple scattered photons is also more randomized compared to that of the ballistic photons, provided that a polarized optical beam is used for the imaging. Considering these two characteristics, it is possible to use

relatively simple spatial filters and polarizers to filter out the multiple scattered parts of the beam and to provide a condition that ballistic photons survive for the purpose of imaging the core jet. The most effective filtering technique for ballistic imaging on dense sprays, however, is believed to be time-gating (Linne 2013). The fact that multiple scattered photons travel a longer path through the spray, makes them exit it later than the ballistic and snake photons (snake photons refer to those singly-scattered with negligible path difference from ballistic photons). A typical ballistic imaging setup is described in more detail later, but briefly the idea is to use the Kerr effect of some materials like carbon disulfide, along with ultrashort pulse laser systems, to time-gate the diffracted imaging beam in order to only allow the first groups of photons transiting the spray to proceed to the camera and block most of the diffuse (multiply scattered) photons.

The other complication for imaging the liquid core of the dense sprays is its 3D nature. It is not possible to bring all parts of the jet and its associated ligaments and primary droplets in focus even with traditional ballistic imaging (because this imaging will be a shadowgraph). This is why taking advantage of a 3D imaging technology like digital holography has the potential to improve the visualization outcome significantly. Using digital holography creates the opportunity to record the diffraction pattern of the liquid core and to numerically reconstruct the image of it at various depths. In this way three-dimensional information of the core break up process can be extracted from a single planar record and this information can then be used for fluid mechanics studies of the problem without interpretation of slicing or line-of-sight integrated effects. The other benefit of using digital holography for imaging dense sprays is the natural coherence filtering it provides. The

fundamentals of holography are described in detail later but simplistically digital holograms are interference patterns between a diffracted imaging (object) beam and a reference beam. In the case of using ultrashort pulsed laser systems, the only part of the imaging beam that contributes to the interference fringes, is the part that overlaps with photons from the non-diffracted reference beam; the rest of the stretched imaging beam just causes background noise that degrades the signal but does not eliminate it.

Although pseudo-ballistic imaging (which refers to soft time-gating that permits some snake photons), coherence filtering, and digital holography are proven diagnostics tools in particle and spray research, very little work has been reported in digital femtosecond holography, and only one published work describing the combination of these methods has appeared (Trolinger et al. 2011). The promising result of this earlier work is the starting point and motivation for the current research. In particular, we have seen that the sacrifice of spatial resolution of the digital hologram for the higher signal to noise ratio as a result of filtering the image beam raises an important question about the capability of producing high quality digital holograms with femtosecond pulses. The intention of the current work is to investigate the capability of applying ultra-short pulse digital holography for imaging dense sprays and to study the feasibility of using femtosecond pulsed lasers in order to accommodate this technique for imaging through high scattering media such as dense sprays. In this dissertation the capability of femtosecond digital holography for 3D imaging through highly scattering media similar to diesel sprays is demonstrated and the effectiveness of the technique for filtering multiple scattered noise is examined in

comparison with Kerr effect time gating, which is believed to be the most promising existing method for imaging the formation of diesel sprays.

In the following chapters the fundamental background of the techniques used in this research are discussed, along with experimental results, analysis, and a comparison of their effectiveness for typical proposed applications. In chapter 1 a brief review of fluid dynamic theories that describe spray formation and the difficulties of studying dense sprays is covered. Chapter 2 is a brief literature study of different optical diagnostic techniques that has been tried to look at the formation region of dense sprays. Chapter 3 is dedicated to the theory of digital holography and digital reconstruction in general, and ultra-short pulse off-axis digital holography specifically. Chapter 4 covers Kerr effect ballistic imaging in theory and its application in dense sprays diagnostics. It is in chapter 5 that the characteristic experimental results of different techniques are presented along with discussion and comparison of their effectiveness for imaging through highly scattering media. Chapter 6 summarizes the effort in this research and concludes with the most effective techniques for different conditions, including the proposition of some useful research follow-up for the future.

CHAPTER 1

Spray Formation

Sprays are formed when liquid jet begins to disintegrate into small droplets dispersed into a surrounding gas phase as a result of interaction between inertial, aerodynamic, surface tension, and viscous forces in the flow. Under specific conditions the liquid jet faces perturbations and oscillations which results in complete disintegration of the liquid jet into droplets. Instabilities result from growth of disturbances on the liquid surface that occur when the liquid penetrates the gas phase. Primary breakup, which is the disintegration of the liquid core into ligaments and droplets, is a result of these gas-liquid interfacial instabilities. The harmonic fluctuations of the liquid jet breaks into irregular shaped large droplets (dense region). If the primary droplets are too large, secondary breakup takes place and smaller droplets are formed. Figure 1 shows an illustration of liquid jet breakup.

The liquid volume fraction (LVF) in sprays is close to one adjacent to the injector tip, which shows the presence of the liquid core and decreases in the axial and radial directions, and the LVF is usually smaller than 0.1 in the dispersed regions (Faeth 1995; 1996). Figure 2 shows the LVF measured (Tseng 1992) and predicted based on a Favre-averaged turbulence model under the assumption of Locally Homogeneous Flow (LHF) (Ruff 1989). It's observable that the liquid core length, which is in order of a few millimeters, is decreased as the ambient pressure goes from 1 to 8 atm. The decreasing core length suggests better atomization. In some sprays, like the hollow cone sprays running at high

injection pressure, the atomization begins right at the nozzle tip, and a distinct liquid core is not noticeable. In some other cases, like sprays used in diesel engines, the surrounding fog of atomized droplets is so optically thick that it is not possible to image the internal structure of the liquid phase inside the dense region. The inability to unequivocally image this inner core zone has perpetuated a controversy about the presence of an intact liquid core (Linne 2006).

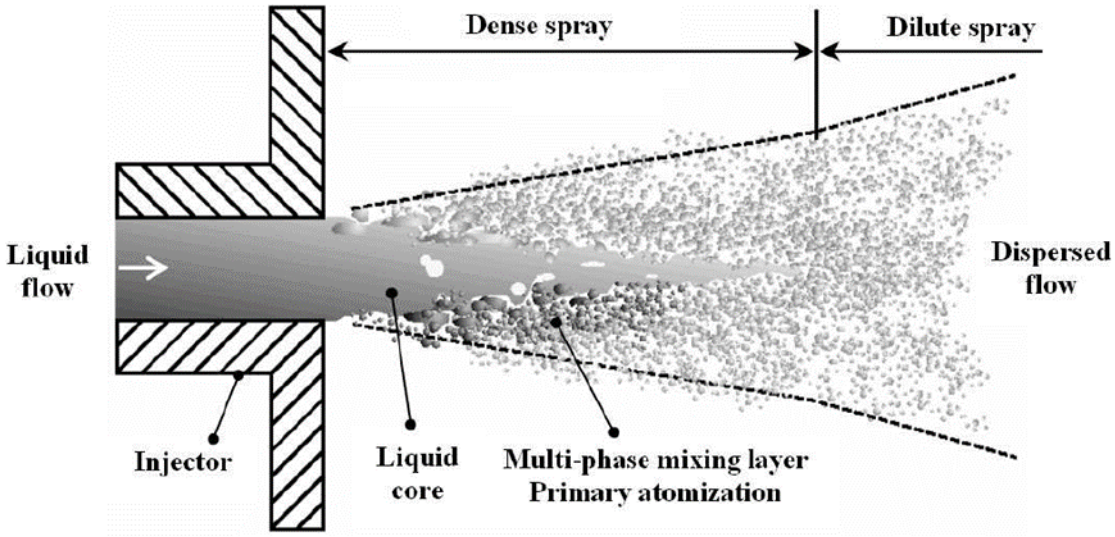

Figure 1- Illustration of the spray structure in the atomization regime (adapted from Faeth et al. 1995).

Figure 3 shows some examples of sprays operating at different conditions (Berrocal 2006). In Figure 3(a) photographs of hollow-cone sprays are generated at 1.2 bar injection pressure for several liquids are presented. It can be seen that the shape of the cone is largely affected by the liquid properties and in particular by the liquid viscosity (Mulhem 2004). In Figure 3(b), shadowgraph images of a diesel spray running at different initial injection pressures are illustrated at 20 ms after injection (the ambient gas is set to 20 kg/m^3 density and 20 C temperature) (Suzzi et al. 2004). Contrary to most other sprays,

automotive sprays run in a single injection regime so that their steady state is never reached. That is, each injection event is short enough in time that the startup and shutdown transient portion of the spray encompasses a majority of the overall injection period. Figure 3(c) shows the influence of the nozzle geometry on the spray pattern of superheated liquids (100-150 C). The use of superheated liquids allows the generation of droplets of a few micrometers while maintaining moderate velocities (Rossmeissl and Wirth 2004). Finally, the sequence of ballistic images in Figure 3(d) shows the effect of the initial jet diameter and gas velocity on a jet in cross flow (Linne et al. 2005).

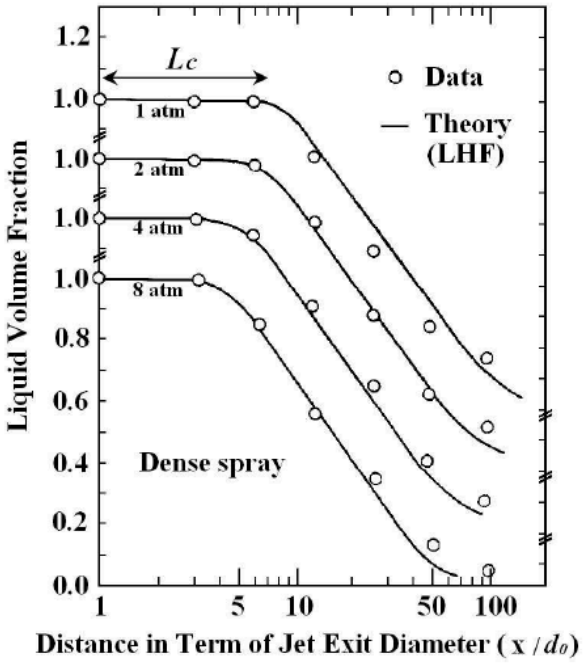

Figure 2- Time averaged liquid-volume fraction along the axis of round pressure-atomized water spray at various pressures for fully developed turbulent liquid flow at the nozzle exit (Tseng et al. 1992).

These examples show that the properties of the injected fluid, environment gas, and nozzle geometry determine the quality of atomization. Viscosity, which is the most effective fluid property on spray disintegration, resists against fluid flow, so by increasing viscosity the

flow rate decreases and the liquid core instabilities are hindered, which results in narrower spray angle, larger droplets and longer liquid core length (Berrocal 2006). As the viscosity decreases with temperature increase in most of the liquid fuels, the atomization is improved in most of the cases with heated liquids (Lefebvre 1989). Surface tension, which is the second most important fluid property in spray generation, resists against the fluid expansion and makes liquid disintegration harder. As surface tension usually is reduced with temperature increase, the

atomization is easier at higher temperatures. Effects of liquid density on spray break up have not been studied as comprehensively as the effects of viscosity and surface tension, but some researchers show weaker atomization for more dense liquid as the inertial forces in the liquid core resist against disintegration and ligament formation (Rizk 1976).

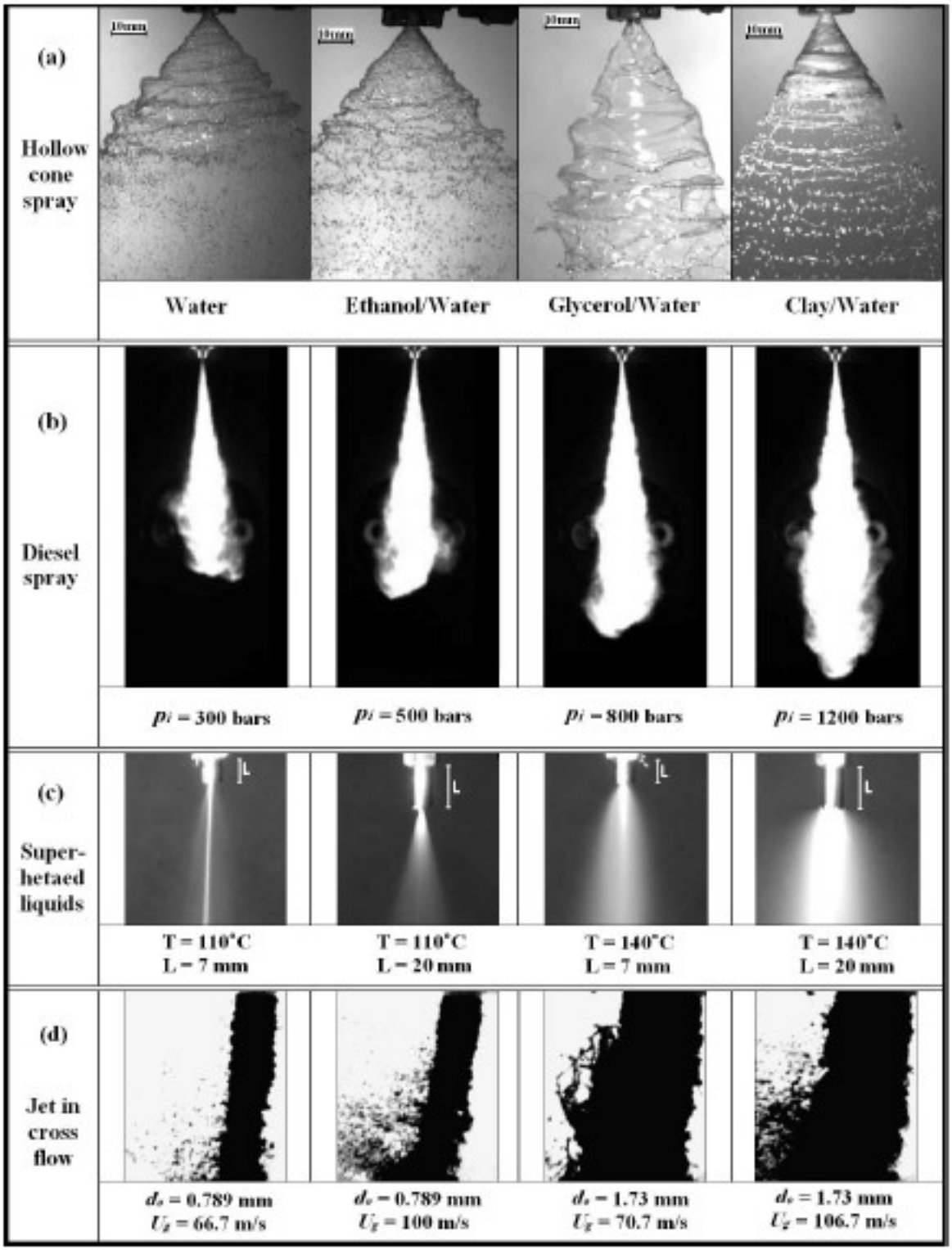

Figure 3- Example of sprays generated at different operating conditions (Berrocal 2006).

The injection pressure and jet velocity are among the fluid flow properties that affect the spray atomization the most. Higher pressure and velocity results in more instability induced in the liquid core and therefore in higher atomization. The turbulence régime of the flow inside the nozzle also influences the atomization quality considerably. Turbulence of the fluid flow contributes to disturbance of the liquid core of the spray and helps the atomization. Reynolds number, which indicates the ratio of inertial forces to viscosity, determines the turbulence regime of the fluid flow. In general, internal flows are considered to be turbulent for Reynolds higher than 2320 (Shiller 1922).

$$R_{\mathrm{e}} = \frac{l_l \rho_l U_l}{\mu_l}$$

l_l is the characteristic length of liquid flow, ρ_l is the liquid density, U_l is the liquid flow velocity, and μ_l is the viscosity. Most practical nozzles have internal flows with Reynolds number in the turbulent regime.

Properties of the environment gas, like velocity, density, temperature etc. affect atomization as well. Denser ambient gas results in smaller droplets, shorter liquid core and shorter penetration, but wider spray angle. In order to investigate the effect of different parameters on atomization, several characteristic dimensionless numbers are defined. The most famous is the Weber number, which indicates the ratio of inertial forces that tend to break up the liquid flow and surface tension that resists this break up:

$$We = \frac{l_l \rho_l {U_l}^2}{\sigma_l}$$

σ_l is surface tension of the liquid. Weber number has been useful for predicting the break up regimes. Table 1 shows different regimes of the spray breakup at various Weber numbers. Figure 4 shows how spray breakup regimes depend on Reynolds and Weber numbers. The third important dimensionless number for characterizing atomization is the Ohnesorge number which indicates the ratio of viscous forces to surface tension forces:

$$Oh = \frac{\sqrt{We}}{Re} = \frac{\mu_l}{\sqrt{l \rho_l \sigma_l}}$$

At high Oh numbers there is more resistance against break up and more inertial forces are required for atomization to occur.

As suggested by the dimensionless numbers, depending on different conditions of the spray generation, the liquid phase breakup into the gas phase has been divided in the classical spray literature into different regimes:

1) Rayleigh Regime: At low jet velocities where the aerodynamic forces are negligible, surface tension plays the dominant role in droplet formation: As far as the wave length of axisymmetric disturbances on jet surface are smaller than initial circumference of the liquid jet (Λ_{min}) , surface tension damps this

fluctuations. However, as soon as axisymmetric fluctuation wavelength exceeds $\Lambda_{min,}$ surface tension amplifies them and the liquid jet finally breaks into droplets. Rayleigh calculated the fastest growing wave length to be $4.51d_0$ (Λ_{opt}) for invicid condition and the volume of the induced droplet to be equal to the volume of a cylinder of the same diameter as the nozzle (d_0) and length Λ_{opt} which results in droplets of $1.89d_0$ diameter. Tyler (1933) confirmed droplets of $1.92d_0$ diameter experimentally. In 1931 Weber extended Rayleigh's theory to viscous flow. He predicted minimum perturbation wavelength for the viscous jet to be the same as inviscid case. The fastest growing wavelength however, was predicted larger than inviscid case.

2) First-wind induced breakup regime: as the jet velocity increases, the aerodynamic forces enhance axisymmetric surface waves which eventually results in liquid jet breakup into droplets of the same diameter as the nozzle and the breakup occurs several diameters downstream of the nozzle.

3) Second wind induced breakup regime: at higher velocities aerodynamic forces become responsible for small wavelength harmonic waves which result in liquid jet breakup into droplets that are in average smaller than the nozzle diameter and have a wide size distribution. The breakup takes place several diameters downstream of the nozzle.

Table 1- (Berrocal 2006) Classification of the disintegration regimes (Source: Lin and Reitz 1998 Pictures: Vahedi *et al.* 2003).

Breakup regime	Picture	Schematic	Dominant droplet generation mechanism	Weber number
Rayleigh		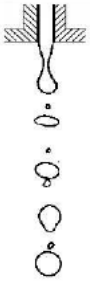	Surface tension force	$We > 0.4$
First wind	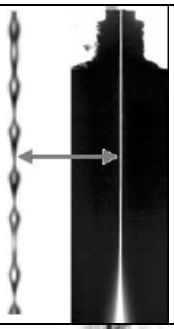		Surface tension Dynamic pressure of ambient air	
Second wind	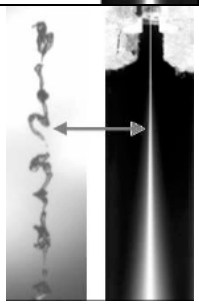		Surface tension Dynamic pressure of ambient air opposed by surface tension initially	$We > 40.3$
Atomization	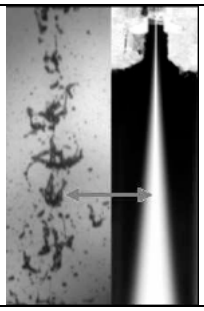	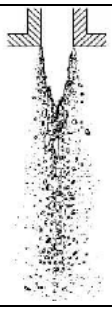	Aerodynamic and shear forces Turbulence Expansion Surface tension force initially	$We \to \infty$

4) Atomization: finally at extremely high jet velocities the liquid breaks up right at the nozzle tip into a multiplicity of droplets much smaller than the nozzle diameter. In most combustion and industrial applications the sprays are designed to run in the atomization regime. In practice atomizers generate droplets from 1 to 500 micron, however, droplets larger than 100 micron are rarely found in sprays with 20 micron mean diameter. Figure 5 shows an example mean diameter distribution in a diesel spray at different times after injection.

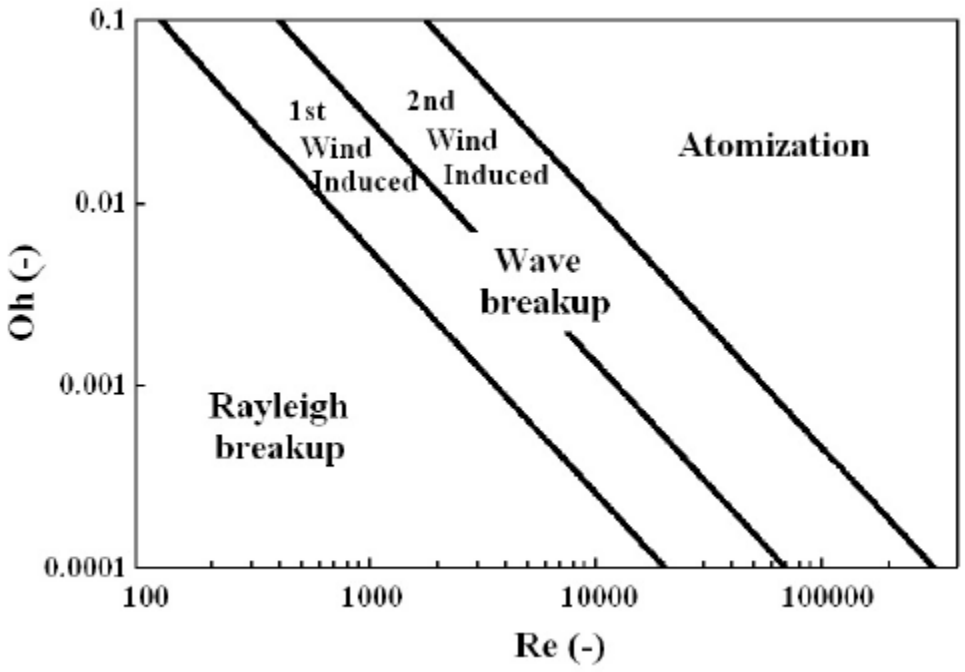

Figure 4- Classification of the disintegration regimes as a function of the Ohnesorge number versus Reynolds number (Reitz 1978).

The physics of liquid breakup in the atomization regime is so complicated that is not still known in detail although different hypothetical models exist. For example, there is

significant disagreement among scientists regarding the existence (or lack) of a liquid core in the dense spray region in atomization regime (Paciaroni 2004). The difficulty in studying this region is that there is an optically thick fog surrounding the dense spray, which then requires special imaging techniques to look into the internal structure of the spray. The imaging objective of looking into the core region of an optically dense spray, which would then resolve the disagreement regarding the intact liquid core, is the focus of this dissertation. Hence, the optical environment that mimics an optically dense spray surrounding an opaque object (the liquid core) is the situation studied. The various technologies which have been applied toward the goal of imaging dense sprays are reviewed in the next chapter.

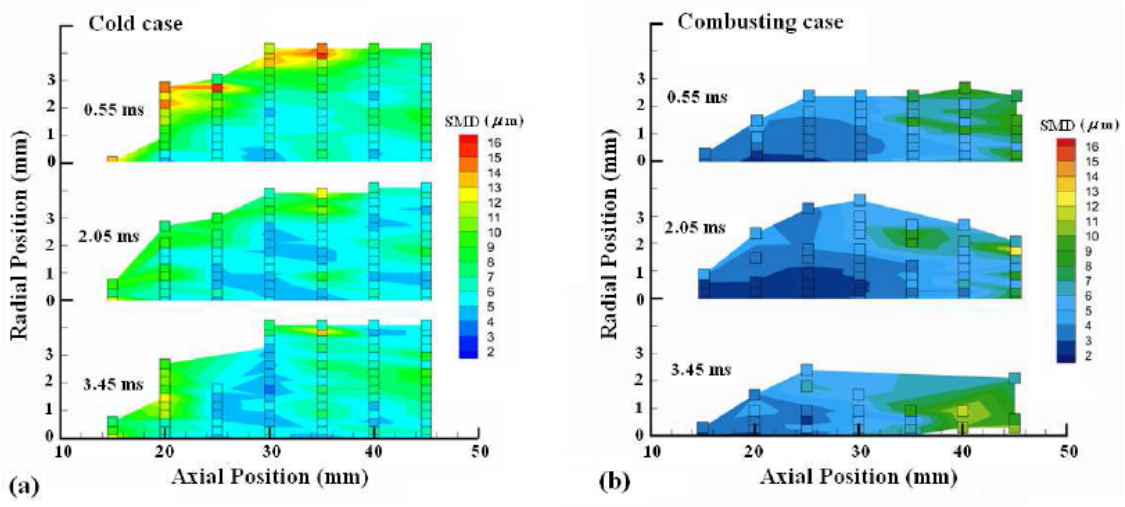

Figure 5- Example of Mean Diameter distribution in a diesel spray at different time after injection (Source: Labs and Parker 2006)

CHAPTER 3

Optical Diagnostics on Dense sprays

In the late 1990's it was believed that the internal structure of the dense region of an atomizing spray could not be observed with non-intrusive diagnostics. The value of such a measurement was presumed to be so high, however, that by the end of the following decade various efforts had been made to use different techniques visualizing this visually impenetrable part of sprays (Linne 2013). First, Powell and his coworkers in Argonne National Laboratory managed to use synchrotron x-ray beam to detect absorption in near field of supersonic sprays (Powell et al. 2000). This technique is capable of providing quantitative information about the fuel mass which includes liquid core, ligaments, and droplets in the dense spray region in 2D and 3D (after reconstruction) and it can also be used to visualize flows inside solid flow channels. An example of results presented by this group is depicted in figure 6.

The next technique applied to dense sprays was Ballistic Imaging (BI), which refers to making use of the statistically very few ballistic photons that are not scattered by the surrounding thick fog of dense sprays for imaging the internal structure buried inside it. First Galland and his coworkers applied ballistic imaging in a very early spray study (Galland et al. 1995). Ballistic imaging had been vastly used in medical applications for imaging in turbid tissues even earlier but the technique had not been used in a two-phase flow enviroment. Alfano and his group suggested using time-gating in ballistic imaging first

(Demos et al. 1996). Later in the early 2000's Linne and Paciaroni developed a new time-gated, fs laser-based single-shot ballistic imaging (BI) instrument for the dense scattering region of sprays, applying it first to a water spray undergoing turbulent primary breakup (Paciaroni et al. 2004). This technique is capable of capturing the liquid-gas boundaries buried inside the dense spray fog (Figure 7). Later, the same group showed that two successive images of a spray can be correlated in a way that velocity vectors of droplets and ligaments can be determined (Sedarsky 2006). Since then, ballistic imaging has been applied to a variety of sprays looking at their internal structure.

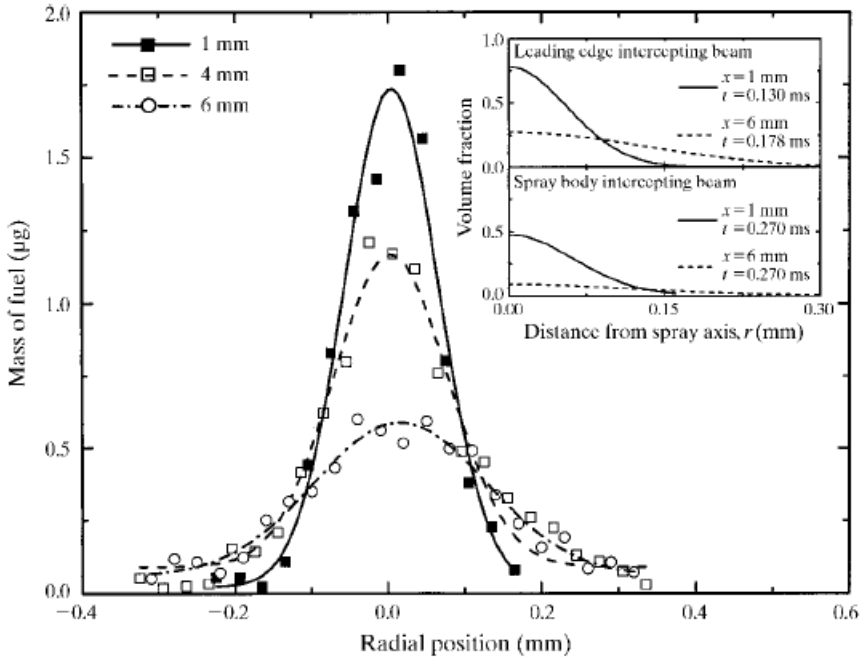

Figure 6 - Measured fuel mass as a function of the radial position at three different axial positions. In this figure, the fuel mass was measured in the main body of the spray at time t = 0.27 ms. The curves are Gaussian fits to the data. The inset shows the calculated volume fraction at distances of 1 and 6 mm for the leading edge (upper panel) and main body (lower panel) of the spray. A volume fraction equal to unity implies the density of pure liquid fuel. The data shown were measured at 500 bar injection pressure and 300 ms injection duration using SF6 as the chamber gas (source: Powell et al. 2004).

In order to improve the spatial resolution of the x-ray technique, the group at Argonne National Lab used short pulsed x-ray beams to acquire single shot images of transient diesel sprays and to correlate successive images to calculate velocity (Wang et al. 2006). This technique, which is called phase contrast imaging, was originally developed for high-resolution electron microscopy, and it is now most commonly used in x-ray microscopy (Linne 2013). Figure 8 illustrates an example of images acquired of dense sprays using this technique. Investigating different results made with phase contrast imaging (PCI) shows that even at moderate visible light optical depth PCI images of the core are highly corrupted. X-ray radiography, however, is capable of providing precise quantitative measurements of the liquid fuel mass per unit area with high resolution in both time and space, and is a unique diagnostic in that manner. Unfortunately this technique has not been applied at high pressure (above 20 bar) and high temperature conditions due to technical limitations. Lab sources can be used for x-ray radiography, but the results are not even close to the quality of those made with a synchrotron like the Advanced Photon Source (APS) at Argonne National Lab, which is a US department of energy visitor facility. Another complexity for x-ray imaging is the need to seed the liquid with an absorber for there to be sufficient absorption. This seeding can change the other properties of the liquid such as density, viscosity, and surface tension, which disturbs studying behavior of the spray under realistic conditions.

The other technique originally used for medical imaging and recently applied in dense sprays by Kristensson, Berrocal and their coworkers is called structured laser-based illumination for planar imaging (SLIPI). This technique is a combination of computer

tomography (CT) and structured illumination. Samples are illuminated with sinusoidal intensity pattern and the multiple scattering is suppressed by local background correction after image acquisition. Therefore, the technique is limited to less optically deep media than those accessible to ballistic imaging and x-ray imaging. However, different kinds of signal filtering such as spatial filtering and time-gating can be integrated with SLIPI to improve the multiple scattering suppression (Kristensson 2012). For SLIPI, in order to reconstruct the extinction coefficient in 3D, at least three single shot images need to be recorded in very rapid succession. So three laser systems and a suitable recording system is required. An example of images made by this group is depicted in figure 9. SLIPI is limited by the dynamic range of current CCD architectures to flows with OD < 6 (Linne 2013). SLIPI is commercially available. It can be used with almost every kind of planar imaging system such as LIF in order to improve their access to optically deep regions of flows.

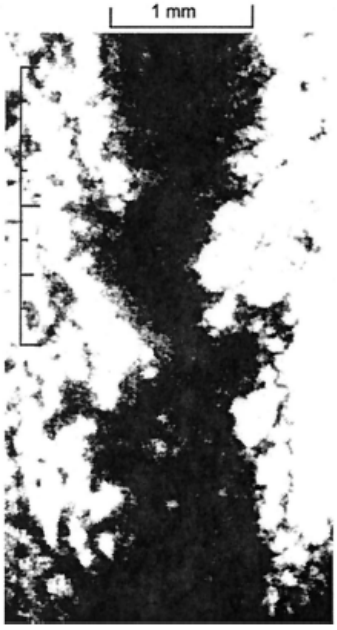

Figure 7- Image of a water jet taken 25 mm from the jet nozzle with first-harmonic OKE gating and a 400 nm spatial filter. The approximate extinction coefficient of the spray at this location is 5 (Source: Paciaroni et al. 2004).

Another potential limitation with SLIPI is that temperature gradients inside the flame can destroy the patterning of the laser sheet. Therefore, this method has not been used extensively for combustion studies as it may be used only for uniform flames.

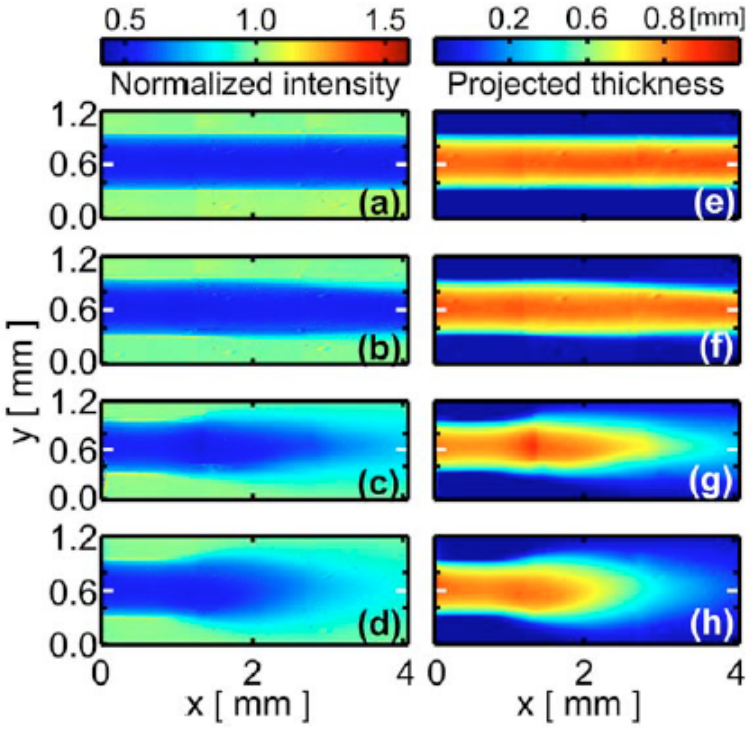

Figure 8- Phase-contrast images (a–d) and the reconstructed 2D projected thickness maps (e–h) at a water flow rate of 2.4 ml/ s or 7.0 m/s and under 0 kPa (a and e) and 68 kPa atomization air (b and f) and 110 kPa (c and g) and 137 kPa (d and h) atomization air pressures (Source: Wang et al. 2006).

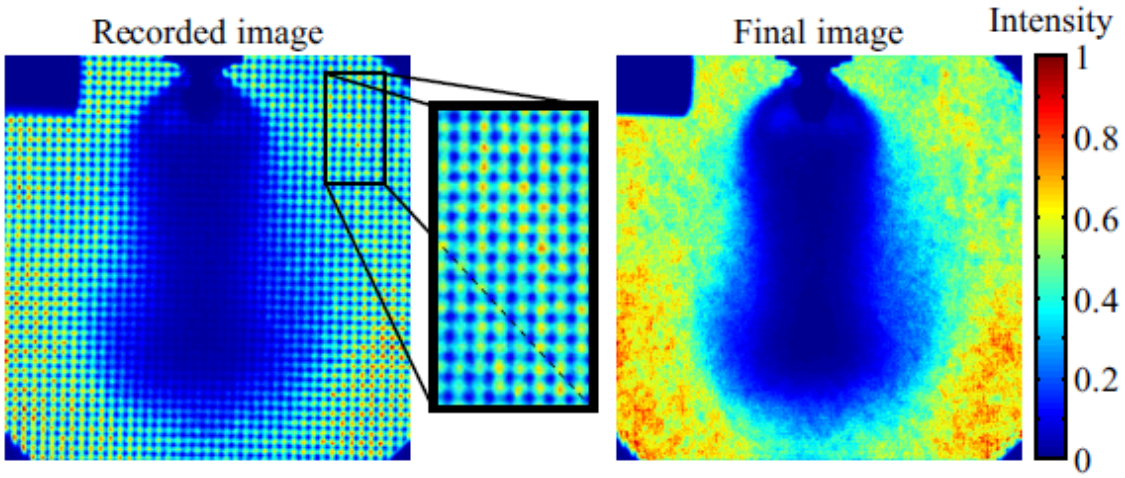

Figure 9- An example of a single modulated transmission image with the corresponding SI-image (Source: Krinstensson et al. 2012).

The other novel technique introduced by Charalampous and his coworkers at Imperial College London is called optical connectivity (OC). This method is used to look at the intact liquid core inside the dense spray region and to measure its length. In order to do so, a fluorescing substance is added to the liquid fuel. A laser beam is then directed into the nozzle by means of an optical fiber. The intact liquid core of the spray acts like an optical fiber itself and the laser beam conducted in it excites the fluorescing substance. Recording the laser induced fluoresce (LIF) provides an image of the intact liquid core of the spray from the inside, and its length can be measured (Charalampous et al. 2009). As illustrated in figure 10, the imaged liquid core with OC is generally shorter than the length obtained by shadowgraphy, and this method works more accurately in spray conditions where the intact liquid core is relatively short. At longer liquid core conditions errors occur due to scattering of the induced fluorescence at the liquid gas boundary. However, it's still promising for intact core length measurements in highly atomizing conditions like in diesel sprays.

Among the different diagnostics mentioned above, all of them are useful for providing specific information under specific conditions. Also, none of them is perfect and they all have limitations. Ballistic imaging, however, seems to be the most promising technique for looking at the liquid/gas interface of the larger structures buried in the dense region of atomizing sprays. BI is capable of generating a line-image of the liquid/gas interface just at the edge of the flow (black inside the flow, white in the gas). Voids at the edge of the flow, ligaments, and primary droplets, as long as they are larger than the size cut-off of the system point spread function, are detected in ballistic images of the spray formation region of atomizing sprays. Using image processing techniques on ballistic images makes it possible to do statistical analysis on interface curvature distributions; together with size distributions for voids, ligaments, and large primary drops. Image processing can also be used for obtaining the velocity vector field inside the spray in the two pulse BI. As time-gating BI is expensive and complicated, trying alternatives seems to be reasonable as long as the optical depth is not too high. For high optical depths ($6<OD<15$), however, there is no obvious alternative for BI to image the liquid core structure (Linne 2013). As the liquid phase appears black in ballistic images, another limitation occurs at high liquid flow rate when liquid-to-gas ratio (LGR) reaches its maximum. In that case the entire image of the internal structure of spray is blackened. This limitation raised the idea of integrating BI with a 3D imaging technique like digital holography, and this combination forms the basis for the work pursued in the current dissertation. The main purpose of using digital holography is adding the capability of resolving the spray structure at different depths and scanning through it by reconstructing the raw hologram at different depth. In this way

instead of having a blackened picture of the liquid core representing the integrated line of sight shadow, individual parts and ligaments at different depths can be resolved.

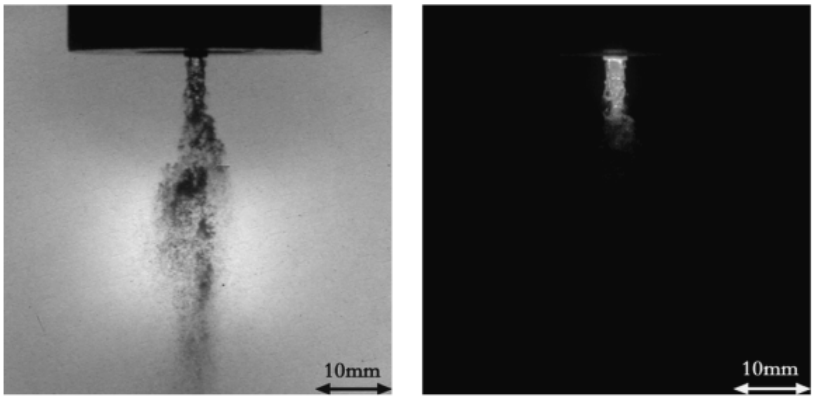

Figure 10- Comparison between simultaneous shadowgraphy and LIF imaging (source: Charalampous et al. 2009)

The above discussion demonstrates that the diagnostics choices for optically imaging in highly scattering environments, particularly those with high speed dynamics and multi-phase refractive interfaces, are extremely limited. At the same time, imaging is powerful source of insight into such flows, and so additional effort expended in developing new techniques is warranted. The following chapter introduces the fundamentals of how accessing the phase information in light waves can provide an opportunity to overcome the significant challenges described.

CHAPTER 3

Ultra-short Pulse Off-axis Digital Holography

Holograms are simply recorded interference patterns of two electromagnetic (usually monochromatic) waves. In the past, this interference pattern was recorded on photographic films, which are called traditional holograms now. On the other hand, if digital recording equipment, like a CCD camera, is used to record the interference pattern, we call it a digital hologram. Digital holography (DH) primarily involves recording digital holograms and reconstructing the original beams with numerical calculations, using previously recorded digital holograms and a computer to back-solve the electromagnetic wave transport equations. Traditional holograms used to be reconstructed physically by illuminating the developed film (hologram) with only one of the beams that had made the original interference pattern in order to resurrect the other beam. Figure 11 and figure 12 depict the apparatus and process of recording and reconstructing a traditional hologram, respectively. A special feature of holography is the capability it gives us to record and reconstruct 3D images as opposed to 2D recording in photography. The reconstructed object beam is identical to the original object beam and it therefore contains all the information the original beam had, including information from different depth planes of the object.

In digital holography, a digital recording device, like a CCD camera is used instead of the photographic film to record the hologram. Physical reconstruction is not common in DH.

Numerical Reconstruction of the virtual image and all the information contained in the original object beam, however, is possible with the aid of computer programming because Maxwell's equations governing the propagation of light are reversible. Hence, the complete image phase/intensity information at any plane can, at least theoretically, be retraced to its source object. In this way we can compute the image of the object at different distances from the camera, which is equivalent to obtaining a 3-D image of the original object.

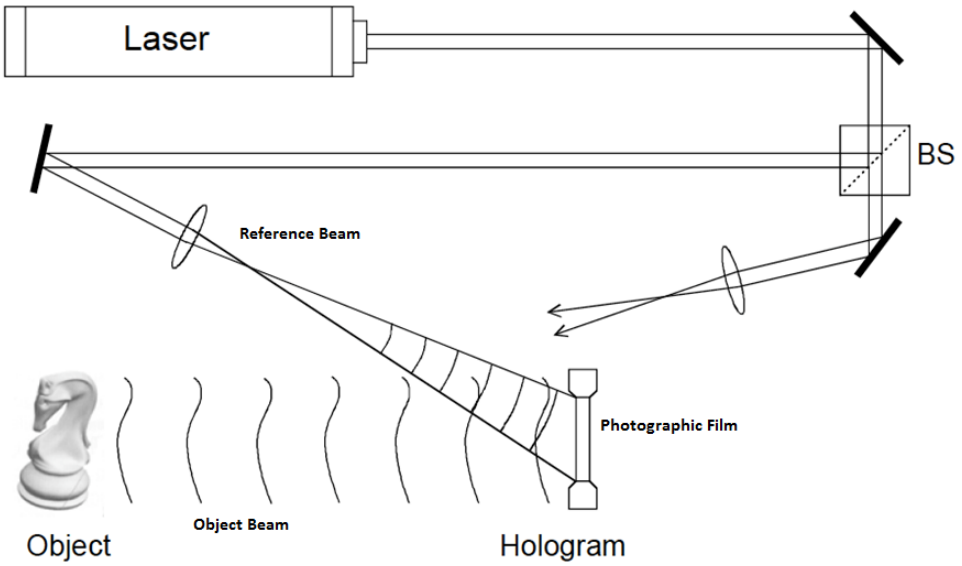

Figure 11- Recording a traditional hologram: The laser beam is split into two identical beams. One is used as a reference beam which illuminates the photographic film after being expanded by the lens. The other beam, which is referred to as the "Object Beam", illuminates the object after being expanded by a lens. The reflected object beam interferes with the reference beam on the plane of photographic film and creates an interference pattern, which we call a hologram (Source: Schnars et al. 2005).

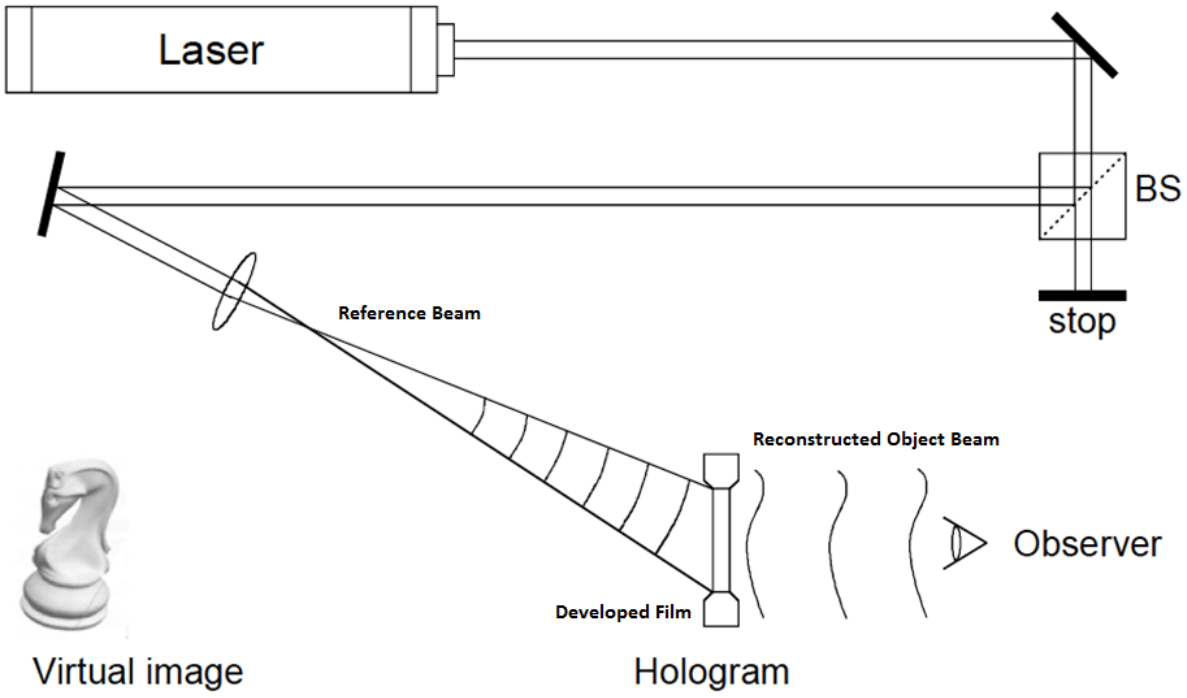

Figure 12- Reconstructing the object Beam from a traditional hologram: Developed photographic film, on which the hologram was recorded, is illuminated by the original reference beam. This time there is no real object. However, as the reference beam is diffracted by the hologram, the original object is reconstructed such that an observer behind the hologram can see a virtual image of the original object identical to the real object both in shape and position (Source: Schnars et al. 2005).

Physical Optics Background

In order to understand the theory behind holography, we begin with some background in physical optics. The equations in the following development are adapted from the book "Digital Holography" (Schnars et al. 2005). As is well known, light is studied from two different points of views, particles and waves. Some phenomena related to light can be justified only by looking at light quanta as particles, called photons. On the other hand, phenomena like diffraction and interference, which are cornerstones in the theory of holography, are only explained by considering light as an electromagnetic wave. Maxwell's

equations govern the relations that describe alternating electric and magnetic fields. The electromagnetic wave equation which is derived from Maxwell's equations is as follows:

$$\nabla^2 \vec{E} - \frac{1}{c^2}\frac{\partial^2 \vec{E}}{\partial t^2} = 0$$

E is the electric field, t is time, and c is the speed of light in this equation. The general solution to this equation is in the form of f(ωt – **k.r**). Since according to Fourier Transform Theory, every integrable function can be decomposed into harmonic function format, we consider the solution to the electromagnetic wave to be described as:

$$E(x, y, z, t) = a\cos\left(\omega t - \vec{k}\vec{r} - \varphi_0\right)$$

In this equation ω is the temporal frequency of the wave, k is the wave number determining the spatial frequency and the direction of propagation of the wave, and ϕ_0 is the initial phase. The following relations can be expressed between these parameters:

$$c = \lambda f \quad \omega = 2\pi f \qquad \left|\vec{k}\right| \equiv k = \frac{2\pi}{\lambda}$$

Intensity (I) is a scalar quantity we define to represent the time average of the energy which passes in space through unit area in unit time:

$$I = \varepsilon_0 c < E^2 >_t = \varepsilon_0 c \lim_{T\to\infty} \frac{1}{2T}\int_{-T}^{T} E^2 dt$$

$$I = \varepsilon_0 c a^2 \left\langle \cos^2\left(\omega t - \vec{k}\vec{r} - \varphi_0\right) \right\rangle_t = \frac{1}{2}\varepsilon_0 c a^2$$

In order to work with the wave function more conveniently, it is generally written as a complex exponential:

$$E(x,y,z,t) = a\exp\left(i\left(\omega t - \vec{k}\vec{r} - \varphi_0\right)\right)$$

$$E(x,y,z,t) = a\exp(i\varphi)\exp(i\omega t)$$

The electromagnetic wave is the real part of these complex functions, but that understanding is implicit and reference to the real part is not written so that expressions are shorter and less complicated.

Since the time dependence of all waves in a monochromatic case (which we assume here for simplicity) is the same, we define the complex amplitude, as follows, and we also derive intensity in terms of it:

$$A(x,y,z) = a\exp(i\varphi)$$

$$I = \frac{1}{2}\varepsilon_0 c|A|^2 = \frac{1}{2}\varepsilon_0 c A^* A = \frac{1}{2}\varepsilon_0 c a^2$$

$$I = |A|^2$$

Since holograms are the recorded interference patterns of two different light waves (monochromatic here), it is necessary to derive the interference pattern of two plane waves, when they are illuminating an object plane with different angles:

$$\vec{E}(\vec{r},t)=\sum \vec{E}_i(\vec{r},t) \qquad i=1,2,...$$

$$A = A_1 + A_2$$

$$A_1(x,y,z) = a_1 \exp(i\varphi_1)$$

$$A_2(x,y,z) = a_2 \exp(i\varphi_2)$$

$$\begin{aligned} I &= |A_1 + A_2|^2 = (A_1 + A_2)(A_1 + A_2)^* \\ &= {a_1}^2 + {a_2}^2 + 2a_1a_2\cos(\varphi_1 - \varphi_2) \\ &= I_1 + I_2 + 2\sqrt{I_1 I_2}\cos\Delta\varphi \end{aligned}$$

The two different waves can be added directly since the wave equation is linear so that the sum of two solutions is itself a solution to the equation.

The intensity pattern of interference of two waves that is calculated here (which is the quantity detected by the human eye, a CCD, or any other optical detector), is a pattern of light and dark fringes that result from constructive and destructive interference of the two light waves. Minimum intensity occurs where the phase difference between the two waves is (2n + 1)π (destructive interference), and maximum intensity occurs wherever the phase

difference of the two light waves is equal to 2nπ (constructive interference). The space between two successive light (or dark) fringes in the interference pattern of two planar wave fronts with identical wavelength of λ and angle of Θ between their directions of propogation is equal to:

$$d = \frac{\lambda}{2\sin\frac{\theta}{2}}$$

The quantity that is detected by the eye or any other optical director is intensity. Holograms are the recorded intensity of the interference between the reference beam and object beam, and this interference intensity can be calculated as:

$$E_O(x,y) = a_O(x,y)\exp(i\varphi_O(x,y))$$
$$E_R(x,y) = a_R(x,y)\exp(i\varphi_R(x,y))$$

$$\begin{aligned} I(x,y) &= |E_O(x,y) + E_R(x,y)|^2 \\ &= (E_O(x,y) + E_R(x,y))(E_O(x,y) + E_R(x,y))^* \\ &= E_R(x,y)E_R^*(x,y) + E_O(x,y)E_O^*(x,y) + E_O(x,y)E_R^*(x,y) + E_R(x,y)E_O^*(x,y) \end{aligned}$$

The developed photographic plate (hologram) that is used in traditional holography to reconstruct the object beam is simply a transparent plate with a transmission function proportional to the intensity of the recorded interference pattern at each point:

$$h(x,y) = h_0 + \beta\tau I(x,y)$$

Here *h* is transmission at point (x,y) of the developed film, h_0 is the transmission of un-illuminated points of the film after development, β is a constant, and τ is the exposure time of the film.

While reconstructing the object beam by illuminating the developed film with the reference beam, the complex amplitude of the diffracted beam at each point of the film is the complex amplitude of the illuminating reference beam multiplied by a transmission function:

$$E_R(x,y)h(x,y) = \left[h_0 + \beta\tau\left(a_R{}^2 + a_O{}^2\right)\right]E_R(x,y) + \beta\tau a_R{}^2 E_O(x,y) + \beta\tau E_R{}^2(x,y)E_O{}^*(x,y)$$

So the diffracted wave front consists of three terms:

1- DC term: the first term on the right side of this equation is the reference wave, multiplied by a factor.
2- Cross term: the second term is the reconstructed object wave, forming the virtual image. The real factor behind it only influences the brightness of the image.
3- Conjugate cross term: the third term generates a distorted real image of the object.

In off axis holography (as is illustrated in figures 1 and 2) the object beam and reference beam propagate in different directions, so the virtual image, the real image and the undiffracted wave are spatially separated. For inline holography (which will be discussed later), however, they all overlap which causes some difficulty since they must then be separated using image processing techniques.

The most interesting part of holography and reconstruction is that although we only recorded the intensity of the interference pattern, and it looks as though we threw away the information related to the phase distribution, the complex amplitude of the object beam, which includes both intensity and its phase distribution, is fully reconstructed. This is possible because the intensity of the interference pattern at different points automatically includes both intensity and phase difference between the object beam and the reference beam at each point.

Digital Holography

In digital holography, however, we don't reconstruct the object beams physically. Numerical reconstruction of the 3-D virtual image using the digitally recorded hologram is our interest. In order to numerically calculate what the virtual image would look like in the case of traditional reconstruction, we must determine the diffraction pattern of the developed hologram illuminated by the reference beam. Understanding this reconstruction requires further discussion of the diffraction phenomenon.

There are two famous (and fundamentally equivalent) interpretations of diffraction. The older one, which is named after Huygens is described as:

- Huygens' principle: *Every point of a wavefront can be considered as a source point for secondary spherical waves. The wavefront at any other place is the coherent superposition of these secondary waves.*
-

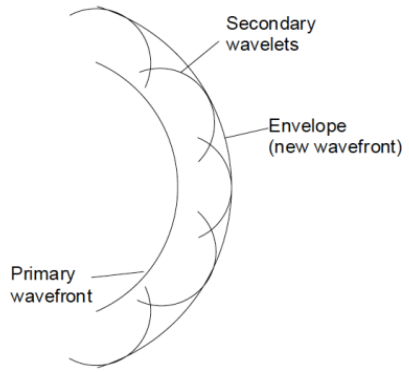

Figure 13- Huygens' Principle (Source: Schnars et al. 2005).

This describes how we can obtain the diffraction pattern of an incident beam diffracted by the developed hologram. We can simply assume that every point on the illuminated hologram is acting like a point source with different amplitude related to the transmission function of each point on the hologram. Then the electric field (complex amplitude) at each point of space behind the illuminated hologram is obtained by integrating the electric field created by each of the point sources on the hologram at that specific point in space. This is exactly what the Fresnel-Kirchhoff integral (derived from Maxwell's Equations), which is the other famous interpretation of diffraction explains:

$$\Gamma(\xi',\eta') = \frac{i}{\lambda}\int_{-\infty}^{\infty}\int_{-\infty}^{\infty} A(x,y)\frac{\exp\left(-i\frac{2\pi}{\lambda}\rho'\right)}{\rho'}Q\,dx\,dy$$

$$\rho' = \sqrt{(x-\xi')^2 + (y-\eta')^2 + d^2}$$

$$Q = \frac{1}{2}(\cos\theta + \cos\theta')$$

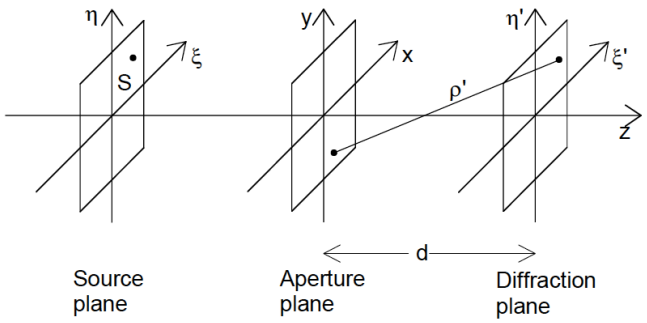

Here Γ is the complex amplitude of the electric field at point (ζ',η') of a plane at distance d from the aperture plane (developed film), and A(x,y) is the complex amplitude of electric field at point (x,y) of the aperture plane (developed film). We can replace A(x,y) with a uniform plane reference wave times the transmission function of the hologram at point (x,y):

$$\Gamma(\xi',\eta') = \frac{i}{\lambda}\int_{-\infty}^{\infty}\int_{-\infty}^{\infty} h(x,y)E_R(x,y)\frac{\exp\left(-i\frac{2\pi}{\lambda}\rho'\right)}{\rho'}dxdy$$

Evaluating this integral numerically is possible. However, since ρ' is inside the exponential, for high resolution holograms an enormous computational power is needed. Fortunately, in the case of large distance between the hologram and the object (or virtual image) compared to the dimensions of the hologram, it is very efficient to use Fresnel's approximation, based on a Taylor's series expansion, to evaluate the integral:

$$\rho = d + \frac{(\xi - x)^2}{2d} + \frac{(\eta - x)^2}{2d} - \frac{1}{8}\frac{\left[(\xi - x)^2 + (\eta - x)^2\right]^2}{d^3} + \ldots$$

If d >> x,y we can neglect higher order terms:

$$\frac{1}{8}\frac{\left[(\xi-x)^2+(\eta-x)^2\right]^2}{d^3} << \lambda$$

$$\rho = d + \frac{(\xi-x)^2}{2d} + \frac{(\eta-x)^2}{2d}$$

$$\Gamma(\xi,\eta) = \frac{i}{\lambda d}\exp\left(-i\frac{2\pi}{\lambda}d\right) \times \int_{-\infty}^{\infty}\int_{-\infty}^{\infty} E_R^{*}(x,y)h(x,y)\exp\left[-i\frac{\pi}{\lambda d}\left((\xi-x)^2+(\eta-y)^2\right)\right]dxdy$$

This equation provides the necessary computational framework with which to analyze digital holograms and extract from them the object information they carry. The following section describes the experimental aspect of the project that was developed to implement and test the analysis strategy described above.

Inline Gabor Holography

Inline holography refers to using a reference beam and object beam that are ideally parallel (though there is a very small angle between them in practice). Since the interference fringe spacing is $d = \frac{\lambda}{2\sin(\frac{\theta}{2})}$ the very small θ between the directions of propagation of the two beams will help to produce a large enough fringe spacing to be detectable with available CCD resolution. The limitation that inline holography causes, is that instead of making holograms of the objects themselves, we can only make holograms of the shadow of the objects since the detector will be placed behind the object. This is not a problem for the

applications of interest since we focus on sizing objects and studying their phase change boundaries.

In Gabor holography, instead of using two beams as reference and object beam, only one beam is used. The part of the beam that is diffracted by the object's boundary acts as the object beam. The rest of the beam, the undiffracted part, has the role of the reference beam. In this way we can avoid the difficulty of separating the beam and we can prevent the need for further adjustments and alignment. Gabor holography works only in media where a reasonable portion of the main beam remains undiffracted. In turbid media, like living tissues, where almost the entire beam is diffracted (often multiply scattered, in fact), using a separate reference beam is necessary. In figure 14 a schematic of a Gabor digital holography setup and example of a digital hologram recorded with it and the reconstructed image of a 400 micron needle is demonstrated.

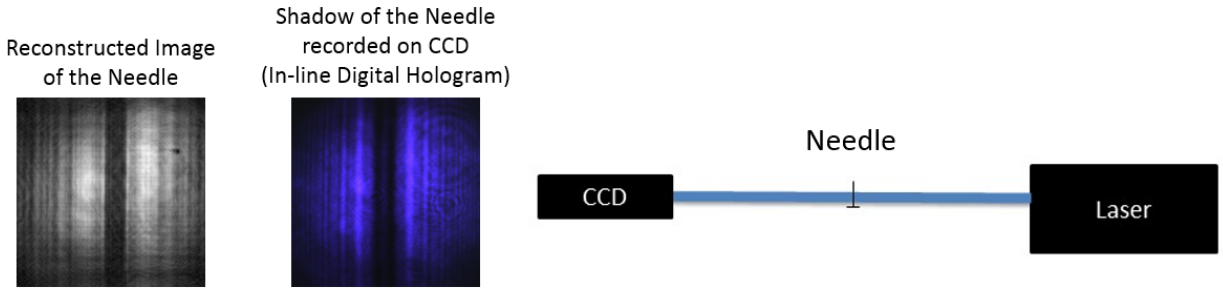

Figure 14- Schematics of a digital inline Gabor holography recording optical setup, an example of a digital hologram recorded from a 400 micron needle using the same setup, and the numerically reconstructed image of the needle.

Figure 15 shows one example of the digital holograms and reconstructed images at different depth by the software. Two 500 micron plastic fibers are used as objects in this example. One fiber is placed approximately 3 inches away from the camera and the other one is placed approximately 6 inches away from the camera. The top left picture in figure 8 is the raw digital hologram recorded by the CCD. The other three pictures are reconstructed images of the same hologram but reconstructed in different depths as indicated above them. The picture in the top right corner is chosen to have the sharpest edges for the left fiber. The depth of reconstruction is 61.3 mm, which matches the distance between the closer fiber and the camera (3 inches = 76.2 mm). In this picture the left (closer to camera) fiber is in focus. The picture in the bottom left corner has a depth of reconstruction of 138.6 mm (this matches the distance between the right fiber and the camera of 6 inches = 152.4 mm). In this picture the right fiber (further from the camera) is in focus and has the sharpest detected edges. Finally, the picture at the bottom right corner is reconstructed at an arbitrary depth (77.1mm) which does not match the actual distance of either of the fibers and therefore both are out of focus, with fuzzy edges.

One interesting fact about this technology (digital holography), is that in situations where focusing on objects is not possible or difficult while taking the picture (e.g., if many particles with different depths are in the picture) it is possible to make an out of focus hologram of all of them and later bring each of them individually into focus using a digital telocentric lens, which is the numerical reconstruction software.

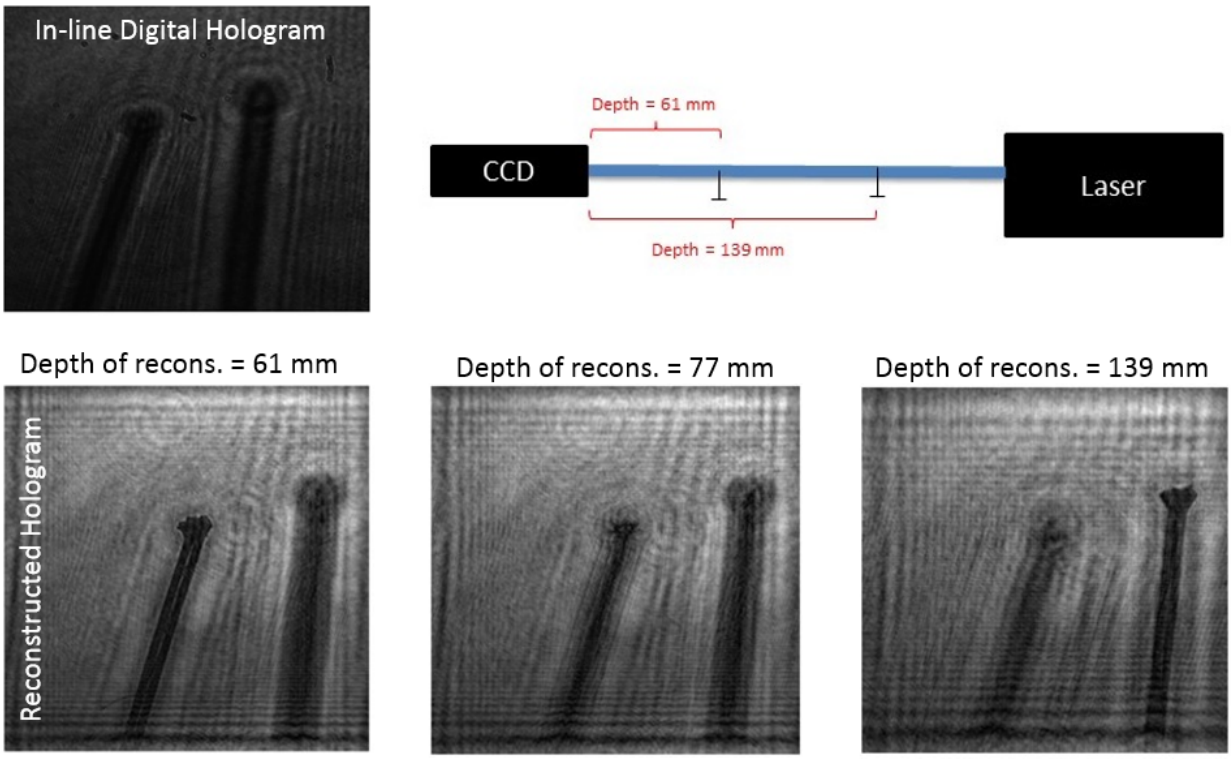

Figure 15- Example of a row digital hologram and reconstructed images at different depths.

In order to predict the resolution of these reconstructed holograms, we need to go back to the theory of interference of coherent light waves. As was mentioned before, fringe spacing for interference patterns between two plane monochromatic waves, at angle θ between the directions of propagation, is $d = \frac{\lambda}{2\sin(\theta/2)}$. While reconstructing a hologram, the largest θ is due to diffraction from the edges of the hologram which is approximately (when d is large) equal to $\theta_{max} = \frac{L/2}{d}$ where L is the length of hologram. This θ_{max} contributes to the highest spatial frequency in the reconstructed image. In digital holography L is equal to the size of each pixel $\Delta x'$ or Dy' times the number of pixels in the desired dimension N. According to the Nyquist Criterion, you need to sample the image with frequency at least twice the highest spatial frequency you want to recover. In other words, the size of the pixels we

need for a reconstructed image is half the fringe spacing. As shown in figure 16, we can summarize these relations as: $\Delta x = \frac{\lambda d}{N\Delta x'}$, $\Delta y = \frac{\lambda d}{N\Delta y'}$. For example, at 400 nm wavelength, recording on a 2000x2000 pixels CCD with 6.45 micron square pixel size, for a reconstructed image at d = 1 inch (25.4 mm), the resolution of the reconstructed hologram would be about 800 nm. These relations show that as we reconstruct the hologram at farther distances we obtain lower resolution in the reconstructed image. In addition, the larger the dimensions of the hologram, the higher the resolution we get in reconstruction. The digital holograms made and reconstructed by the described setup at UCI confirm these theoretically predicted resolutions.

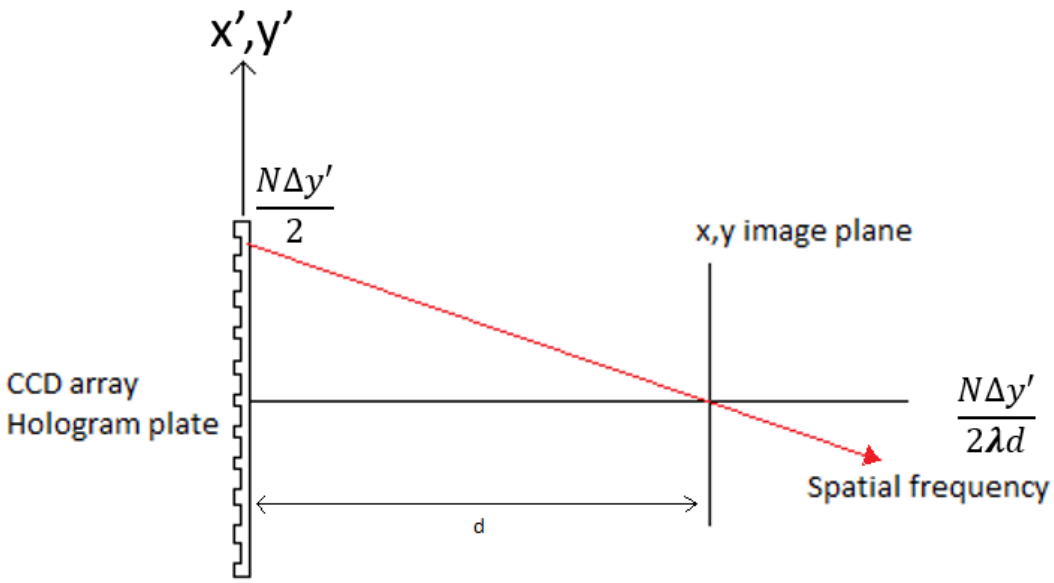

Figure 16- Spatial frequency of the reconstructed hologram (Toal, 2011).

Ultra-short Pulse Off-axis Digital Holography

In the case of imaging through highly scattering media, since there is almost no light left unscattered from the object beam to use as an inline Gabor reference, using a separate

reference beam (off-axis holography) is necessary. To demonstrate the role of an off-axis reference beam, figure 17 illustrates a digital holographic system using an ultrashort pulsed laser. As illustrated in the figure, a diode seed laser followed by a Ti-Sapphire amplifier generates 100 fs pulses of light for hologram illumination. A beam splitter is used to generate a reference beam which goes around the object beam. The object beam goes through an adjustable delay line that is needed to match the path lengths between the object and reference light pulses since the laser pulse is too short to ensure coincidence at the CCD without this adjustment.

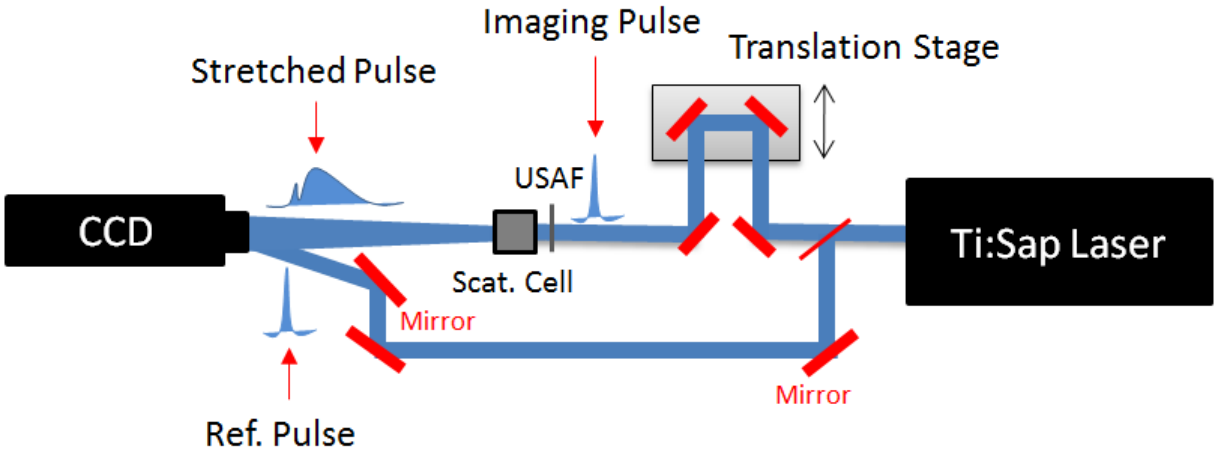

Figure 17- Schematic of the off-axis digital holography setup at UCI.

The object beam is then diffracted by a USAF resolution chart as a test target and goes through a glass cell containing hydrosol of polystyrene particles, which is simulating the scattering condition similar to diesel sprays. A second splitter is used to redirect the reference beam so that the two beams cross each other and interfere right on the CCD. Figure 18 illustrates the interference of the two beams on the CCD. In this case the USAF chart and the scattering cell are removed from the path of imaging (object) beam and the

pattern derives simply from the interference of two planar wave fronts with dark (destructive) and bright (constructive) fringes. In the spatial frequency domain (after fast Fourier transform) the three terms of the interference are separated.

$$A_1(x,y) = a_1 e^{-i\varphi_1(x,y)}, A_2(x,y) = a_2 e^{-i\varphi_2(x,y)}$$

$$|A_1 + A_2|^2 = (A_1 + A_2)(A_1 + A_2)^* = {a_1}^2 + {a_2}^2 + a_1 a_2 e^{-i\Delta\varphi} + a_1 a_2 e^{i\Delta\varphi}$$

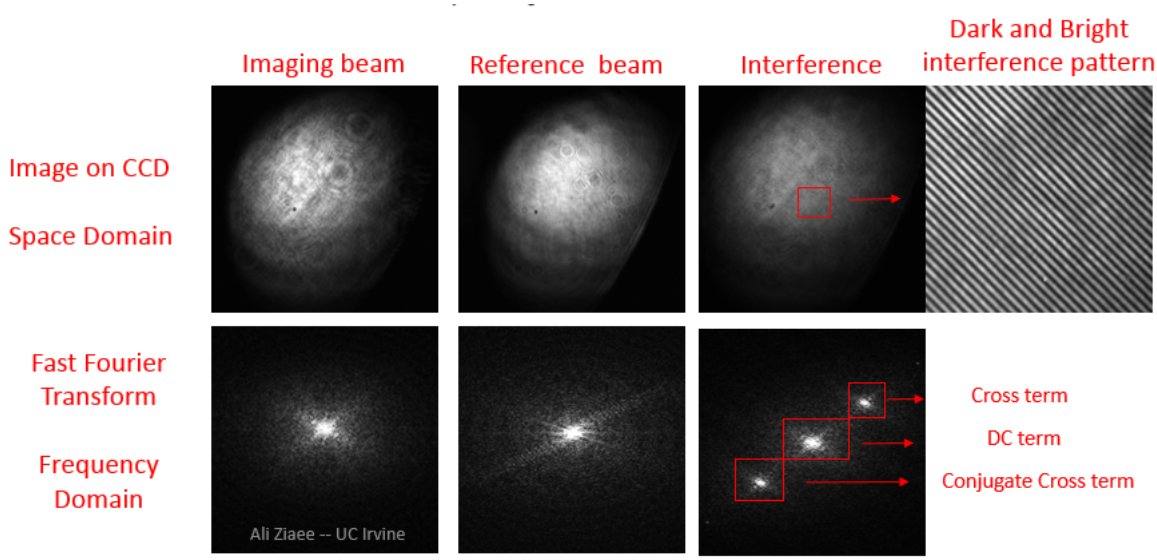

Figure 18- interference pattern of imaging and reference beam in space and frequency domain

At the time when the imaging wave is not diffracted by any objects or scatterers $\Delta\varphi$ occurs only from the small angle between two almost planar wavefronts and the interference pattern looks like equidistant bright and dark stripes. When the imaging wave is diffracted by an object field an additional phase difference occurs on the top of the previous $\Delta\varphi$. The striped pattern is still recognizable but there is an additional pattern visible on top of that (figure 19). In the FFT (frequency domain) of the recorded hologram (recorded

interference pattern) the cross term and conjugate cross term are still separated by the distances as in the interference of two planar wavefronts, but there is also an additional frequency component around the centers (figure 19) as a result of the imaging wave being diffracted by an object field. In order to reconstruct the image of the object field the cross term needs to be cropped from the frequency domain, inverse Fourier transformed, and then reconstructed in the same manner as an inline Gabor hologram, as was explained earlier. Figure 19 shows examples of inline and off-axis holograms recorded from a USAF resolution chart and their reconstructed images. In the case of inline holography all three terms of the interference pattern (hologram) are superimposed on top of each other at the center of the frequency (FFT) plane, whereas in off-axis holography the three terms are separated in the frequency domain and only the cross term is used for reconstructing the object image, as a result of which the reconstructed image looks sharper with less noise.

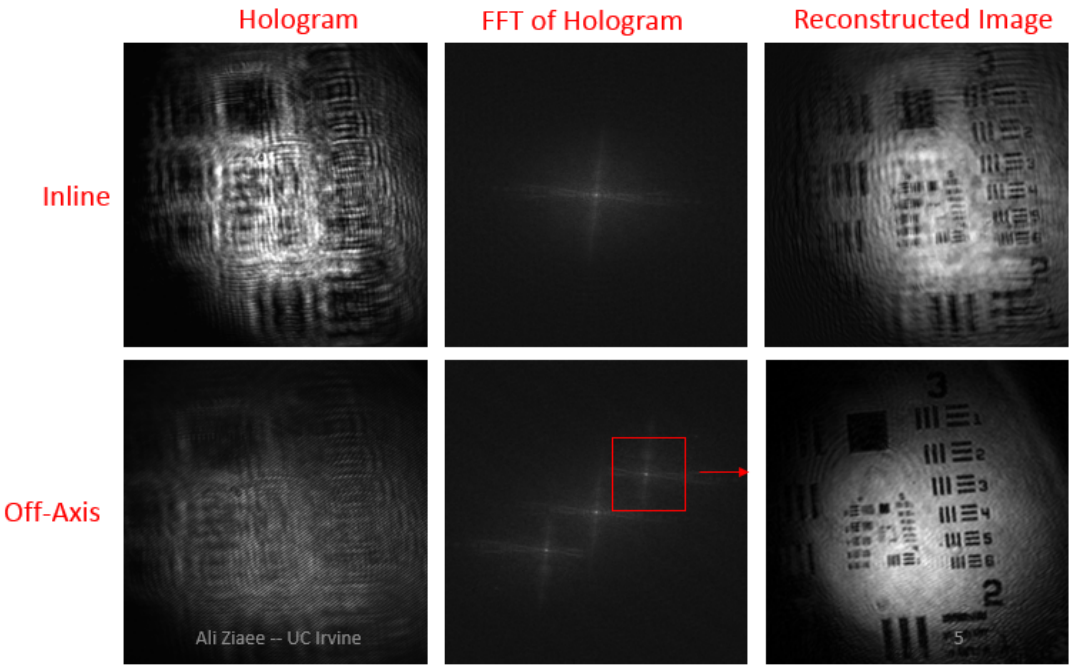

Figure 19 – example of inline and off-axis holograms recorded from a USAF resolution chart and their reconstructed images.

While the theoretical descriptions above are independent of the temporal features of the laser light, all of the holographic work in this dissertation is accomplished exclusively with an ultrashort pulsed laser. The most important limitation of ultrashort pulse holography is the coherence length of the light source. As mentioned earlier, for the results presented in this dissertation a Ti-Sapphire amplifier is used to generate pulses of 100 fs duration, 800 nm center wavelength, 1.2 mj energy, and 1 KHz repetition rate. A doubling crystal is placed at the output of the amplifier, which converts the 800 nm to 400 nm blue pulses with an efficiency of around 50%. The blue light is then used for recording the holograms. The pulse spatial thickness in air is around 30 microns (pulse duration times the speed of light). In the interference pattern of two planar wavefronts the phase difference between the two waves from one bright line to the next is 2π. Since the wavelength is 0.4 micron, the maximum number of high contrast fringes is around 75 (30 microns divided by 0.4 micron). The fringe spacing on the CCD depends on the angle between the imaging (object) and the reference beam: $d = \frac{\lambda}{2\sin(\theta/2)}$. One limitation for θ is that fringe spacing *d* cannot be smaller than twice the pixel size of the CCD (Nyquist criteria). The other limitation is the size of the hologram. If the fringe spacing is too small, the interference pattern of the two beams only covers a narrow band of the CCD, which is the effective size of the hologram. A narrow hologram limits the resolution of the reconstructed images and the size of the reconstructed image will be the same as the effective size of the hologram. If θ is too small and d too large, on the other hand, the three terms of the reconstructed hologram become too close in the frequency domain and the effective separation of the cross term from the DC term is not possible. $\Delta x = \frac{\lambda d}{N\Delta x'}$ determines the resolution of the reconstructed image. In

the case of an off-axis digital hologram, N is limited to the size of the square around the cross term that is extracted from the hologram in the frequency domain (for example, the red square in figure 19). When the cross term is too close to the DC term as a result of θ being too small, the size of the extracted cross term has to be similarly small in order for the DC term not to be included in the extracted information, and that results in a low resolution reconstruction. Hence, the short coherence length of the laser pulse, as explained, causes a serious limitation for digital holography. In addition to the numerical reconstruction degradation, the alignment of such short pulses can be frustratingly difficult. In order for the interference to take place right at the CCD the path lengths of the imaging and reference beam must be precisely matched on scale of microns in addition to precise adjustment of θ.

Despite the limitations imposed by ultrashort laser pulses, there remains a significant benefit in their use, which is the opportunity for coherence filtering. As will be clear as the dissertation results are developed, this coherence filtering helps overcome the multiple scattering noise in cases of imaging through highly scattering media (OD > 5). Photons that are bounced many times off the scattering particles or droplets passing through the scattering environment are no longer coherent with the reference pulse and do not contribute to the frequency shifted cross term which is later extracted from the hologram for reconstruction. This is one other reason to make θ large enough to separate the DC and cross term in frequency domain in a manner that multiple scattering noise is not included in the extracted cross term. The holography setup at UCI is aligned in a way to create maximum separation of the terms in the frequency domain while making sure the effective

area of the recorded hologram is large enough to cover the region of interest for imaging and also wide enough for the reconstruction of the hologram with sufficient resolution. This combination of ultrashort pulsed laser and optimized hologram recording geometry is a unique configuration suitable for quantitative evaluation of holographic imaging performance through highly scattering media.

CHAPTER 4

Kerr Effect Ballistic Imaging

As mentioned before, one main difficulty to image the internal fluid structure of the dense spray region, is the multiple scattering due to presence of small droplets of fuel in the imaging beam pathway. The Lambert-Beer equation which is a special form of the equation of radiative transfer, describes the propagation of light rays in a scattering medium up to a limiting density as follows:

$$\tau = \frac{I_o}{I_i} = e^{-OD}$$

where τ is the fractional transmission through the scattering medium, I_i is the irradiance ($\frac{w}{m^2}$) of the incident beam before entering the medium, and I_o is the irradiance of the non-scattered portion of the beam after passing through the medium. OD is the optical depth of the scattering medium which is defined as:

$$OD = N\sigma_e l$$

N here is the number density of the scattering particles per unit volume (m^{-3}), σ_e is the extinction cross-section (m^2) which is the sum of absorption and scattering cross-sections, and l is the distance that light beam passes through scattering medium. Scattering cross-section of a particle is the area of the incident beam that contains the same power as the power scattered by that particle and can be smaller or greater than the actual cross-section

area of the particle. Similar definition works for absorption cross-section as well. Optical depth of the drop cloud surrounding the near field of typical Diesel sprays is normally between 8 and 10 (Linne 2013). Measuring the optical depth of a medium can be very difficult when it is too dense since the order of the incident and the output irradiance may be so different that they do not stand in the linear range of a single power meter. OD 1-2, which happens usually in the far field of sprays, does not need any specific filtering technique for imaging and can be pictured using white light sources and high speed cameras with shutters fast enough to freeze the motion of the spray droplets. The optical depth of the surrounding cloud at the spray formation region of many different sprays, like hollow-cone sprays and jet in cross flow sprays, stands in a range between OD 2 and 5, where imaging the internal fluid structures requires much more effort. Looking through the dense regions of Diesel sprays with optical depths from OD 5 to 10 requires advanced imaging methods designed specifically for this purpose. The liquid core of some cold Diesel sprays in which the evaporation is slower compared to the sprays into hot air, is veiled behind droplet clouds with depth higher than OD 10 and no imaging technology has achieved to penetrate it so far (Linne 2013).

Depending on the OD of a scattering medium, different scattering regimes exist. For OD smaller than 1, the ballistic photons that have not been affected by the scaterrers are dominant and they exit the medium with the same solid angle as the incident beam. Almost all of the other photons are scattered only once and they exit the medium in directions different than the ballistic photons. This range is called the single scattering regime and it can be accurately solved using particle scattering equations. For $1 < OD < 10$, the average

number of scatters per photons and also the dominant order of scattering is close to OD. This means, for example, if the OD of an environment is 6, each photon is scattered 6 times on average and also the majority of the photons have been scattered exactly 6 times by the scatterers. This is especially true for relatively large diameter scatterers like spray droplets that usually range from 5 to 10 microns in diameter. This region ($1 < OD < 10$) is called the intermediate scattering regime, and no simplifying approximation can be applied in it. For optical depths greater than 10 there is no dominant scattering order and different orders of scattering seem to contribute the same way. The diffusion approximation, in which the medium is assumed as a uniform loss mechanism, can be applied in this region, which is called multiple scattering regime. The optical depth of most of the atomizing sprays in the spray formation region is greater than 6 and they mainly stand in the intermediate scattering region. Numerical simulations can be very helpful in this region and the most promising method is called Monte Carlo (MC) which is based on statistical approximations (Sobol 1974).

An 800 nm laser pulse with 1 mj energy, which is a common choice for ballistic imaging because it comes from a typical fs laser system, contains about 4×10^{15} photons according to the Planck's relation. Only a very small fraction of these photons (depending on OD) make it through a dense scattering medium (like surrounding droplet cloud of a dense spray) without being influenced (scattered) by the scatterers (small droplets). This group of photons, which are called ballistic photons, retain exactly the same characteristics, like polarization and direction, as the original incident beam. Ballistic photons exit the scattering medium with exactly the same solid angle as the incident beam without being

deviated from their original path. They also exit the medium first, since they have travelled the shortest possible path across the medium. Ballistic photons are coherent with the incident beam pulse, which means they are capable of being interfered with the original beam in order to construct interference patterns, which is a critical characteristic for holography. Although this group of photons has perfect characteristics for imaging a shadowgraph of the internal structure of a dense spray, their very low population is not sufficient for recording single shot pictures, which is necessary for studying a transient phenomenon like Diesel spray formation.

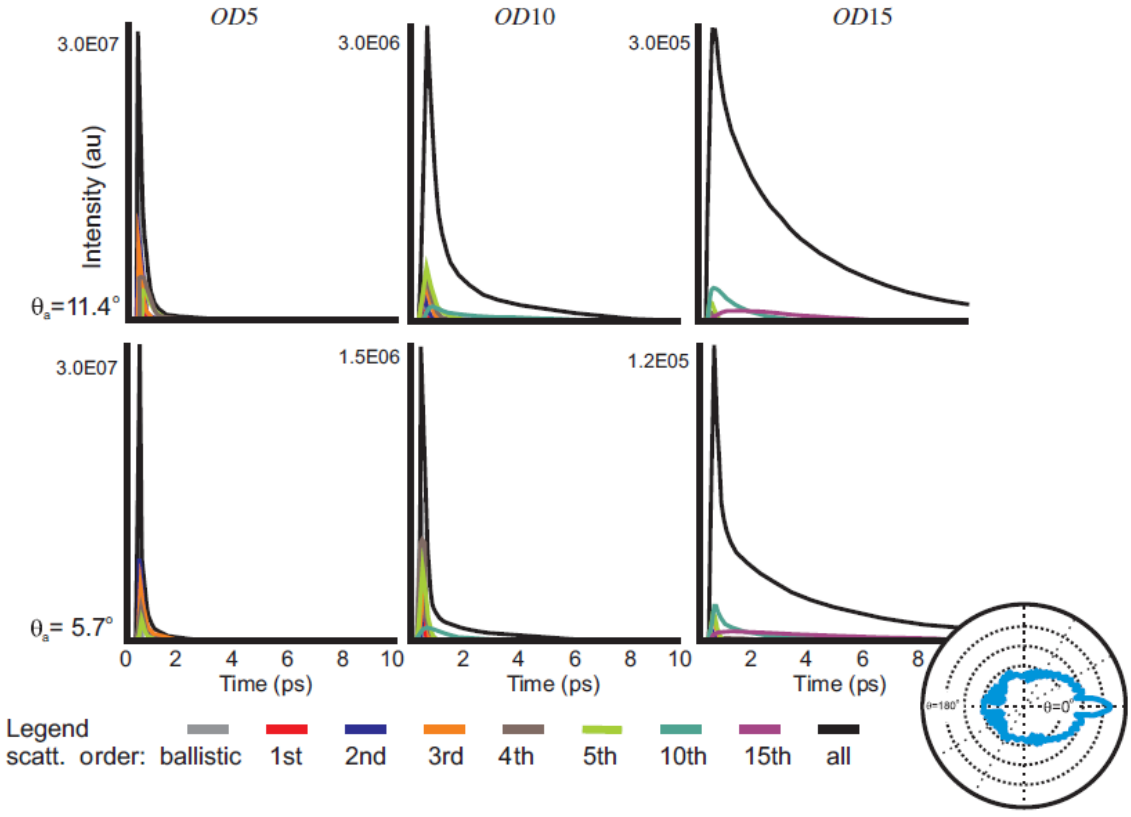

Figure 20- Time dependence of forward scattered light from 5 mm polystyrene spheres in a solution of water, simulated with Monte Carlo method for two optical collection half angles ($\theta_a = 11.4\ and\ 5.7\ degrees$) and three values of OD. Note that the individual orders do not add up to the total represented in black because not all orders are shown. The scattering phase function (logarithmic) for this size is shown in the lower right (source: Linne 2013).

The rest of the photons travelling across a dense scattering medium are scattered once or more by the scatterers. As illustrated in figure 20, for scatterers as large as spray droplets the scattering of visible light is dominant by the forward lobe (Linne 2013). Therefore, photons that are scattered once or only a few times, still exit the medium with a relatively small solid angle variation from the ballistic photons. These slightly scattered photons, which are called quasi-ballistic photons (also snake photons in some literature), deliver a distorted shadowgraph of the structures inside the medium (like intact liquid core is dense sprays) and their polarization is not very much rotated from the original state. Quasi-ballistic photons exit the medium right after the ballistic photons. The longer path they travel through the medium, the later they exit. Therefore, usually those photons which exit earlier, have gone through fewer scattering events, which means they are more capable of constructing high quality undistorted shadowgraphs.

The majority of those 4×10^{15} photons that pass through the scattering environment, however, are scattered so many times that they are no longer useful for imaging internal structures of the medium. These randomly polarized photons, that are called corrupted photons (or diffuse photons in some literature), exit the medium with solid angles spread from zero to 2π. Therefore, using small collecting angles and spatial filtering helps increase the signal to noise ratio by suppressing large fraction of corrupted photons. A similar improvement is possible from using polarizers in the path of the imaging beam (polarization filtering). In order to do a more effective segregation of useful imaging photons in cases of higher OD media, e.g. Diesel sprays, time-gating is believed to be a uniquely advantagous technique. A short laser pulse can be spread out to more than 40

times in time while travelling through a dense scattering medium, according to Monte-carlo simulations. A 100 femtosecond with wavelength of 800 nm laser pulse passing through a scattering medium with optical depth of 10 and scatterers as big as 5 microns in diameter, for instance, is spread out in time up to 4 picoseconds (figure 32). By mitigating a portion of the beam that is at the leading part of the beam and supressing the rest, the idea is to improve the signal to noise ratio and make a better use of quasi-ballistic photons for imaging the larger structure buried inside the medium.

A schematic of the first BI system applied in dense sprays designed by Paciaroni is depicted in figure 21. The output beam of an amplified Ti-Sapphire system with 100 femtoseconds pulse duration and 800 nm wavelength is split into an imaging and a switching beam. The imaging beam goes through a delay line consisting of four mirrors on an adjustable stage, in order to compensate for the extra path length that the switching beam travels going around the spray. A polarizer is placed at the path of the imaging beam right after the delay line in order to make sure the beam is perfectly polarized. A 45 degrees waveplate (rotator) rotates the original polarization of the beam before it is expanded by a set of lenses (telescope) and illuminates the spray. The output light from the spray is collected by a convex lens which focuses the imaging beam into a carbon disulfide (CS_2) cell, where it overlaps the switching beam. The strong switching beam causes the CS_2 dipoles to align along the polarization of the switching beam and create instantaneous birefringence which rotates the polarization of the imaging beam partially back to its original polarization. This non-linear optical behavior of some substances like CS_2 is called the optical Kerr effect. The duration of birefringence is limited to the duration of the switching pulse or the relaxation

time of the Kerr medium (1.5 to 1.8 picoseconds for CS_2 here), whichever is longer. There is a polarizer placed right after the Kerr cell allowing only the light with the polarization perpendicular to the polarization of the polarizer right before the Kerr cell. Using this configuration, 70% to 75% of the imaging beam is transmitted through the OKE gate while the gate is open. Using this setup, one can adjust the delay line so that the gate is open only when the first couple of picoseconds of the stretched imaging beam is passing, supressing photons that arrive later and are mainly corrupted. In this way, the ratio of quasi-ballistic photons (signal) to corrupted photons (noise) is improved and single shut shadowgraphs of the liquid core of the spray can be displayed on the screen and recorded by the CCD camera.

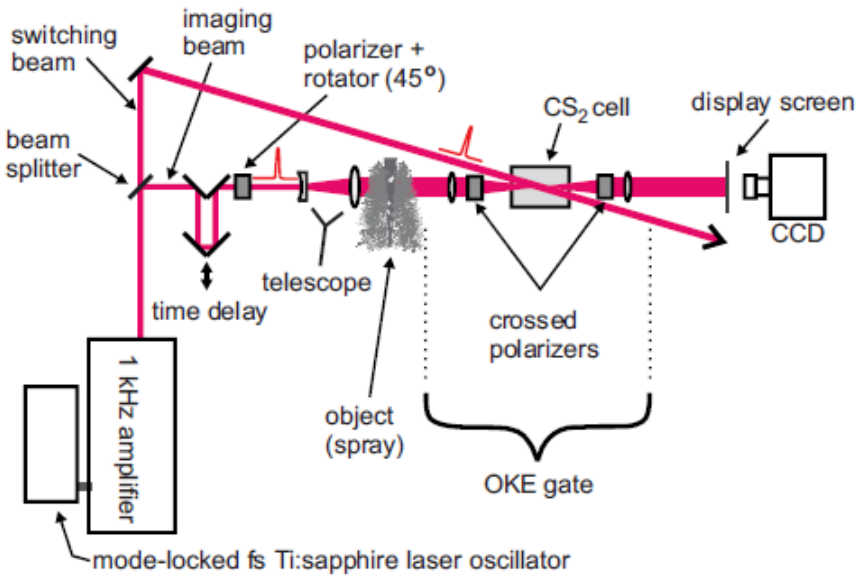

Figure 21- First OKE high-speed shutter experimental configuration applied to dense sprays, designed and set up by Paciaroni (Paciaroni et al. 2004).

Figure 22 shows a typical ballistic image of the first fuel spray studied with optical Kerr effect (OKE) time-gating BI which was a diesel jet injected into the atmosphere from a 155

microns diameter nozzle. The liquid phase appears black in ballistic images, mainly because the light that is scattered by the liquid phase is redirected from the main beam and is not collected for BI. The gas phase, on the other hand, usually appears white since the rays of the beam passing through entirely the gas phase are less deviated from the main beam and build a larger portion of quasi-ballistic photons that are used for BI. So, the gas/liquid interface of the internal structure of the spray is detectable in ballistic images as the boundary between dark and light regions. Looking at a BI shadowgraph like the one depicted in figure 22, one can observe periodic structures at the surface of the liquid fuel and also faint evidence of some ligaments. Formation of the primary droplets, however, is not observable, probably because they are smaller than the spatial resolution of the system (in order of 30 microns here). At the edges of the liquid phase there are some voids also detectable that probably exist all around the spray but the ones that are veiled behind the spray are not detected here (Linne 2013). So, although BI is capable of revealing different valuable details regarding the spray formation at the edges of the spray, the liquid core is still not detected in ballistic images currently made. Therefore there still exist serious doubts whether an intact liquid core inside the diesel sprays formation region, and how it might contribute to the primary breakup process. One significant advantage of digital holography over ballistic imaging is the capability of reconstructing the digital holograms made with ultra-short laser pulses, at various depths, instead of looking directly at the shadowgraphs obtained from BI. In this way, the 3D structure of the liquid core inside the transient diesel sprays is resolved and we can address the fundamental uncertainties regarding this region. The other benefit is that by using a separate reference beam, the coherence filtering nature of two beam holography improves the spatial resolutions of the

reconstructed images so that the formation of smaller primary droplets can be investigated as well.

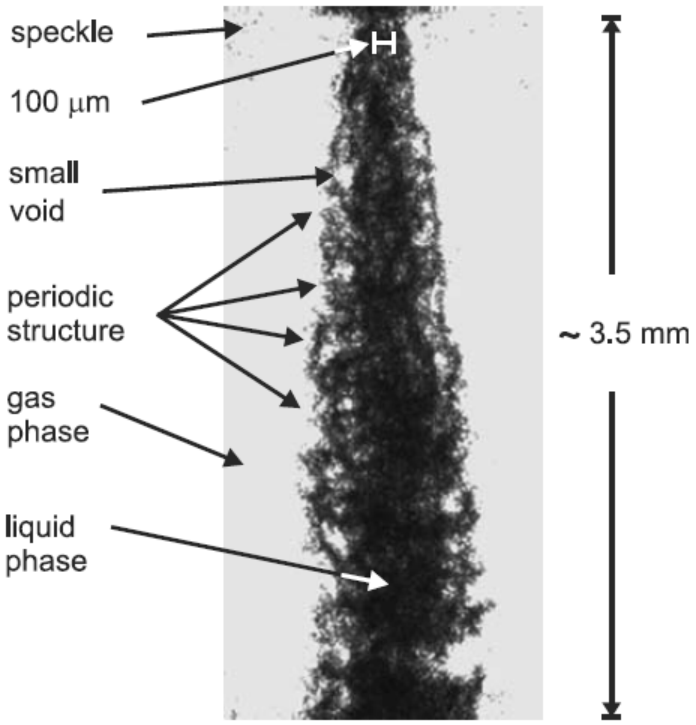

Figure 22- A typical ballistic image of the first fuel spray studied by OKE tme-gated BI which is a diesel jet injected into atmosphere with nozzle diameter of 155 microns (Linne et al. 2006).

In a recent review on imaging techniques in the optically dense regions of a spray, Linne lists different sprays that have been studied using ballistic imaging as follows (Linne 2013): "primary breakup of a turbulent water jet (Paciaroni et al. 2004); the liquid core in an atomizing Diesel spray issuing into air at ~1 bar (Linne et al. 2006 and Idlahcen et al. 2012), 10-15 bar (Linne et al. 2013), 20 bar (Parker et al. 2012), and at 60 bar (Falgout et al. 2013); a laminar water jet in a cross-flow of air (Linne et al. 2005 and 2010); a rocket injector (Galland et al. 1995 and Schmidt et al. 2009); and an effervescent spray (Linne et al. 2010)." He also mentions all the locations where ballistic imaging instruments exist in:

"Two existing systems are capable of acquiring two images in rapid succession so that the images can be correlated to provide velocity of the liquid gas interface. These are located at Air Force Research Labs in Dayton, Ohio (USA) and at CORIA in Rouen, France. Currently, Chalmers is setting up a system capable of acquiring three images in rapid succession, in order to acquire two velocity images. The errors in the velocity images have been shown to lie within 1%-4.5% (Sedarsky et al. 2009), meaning that the two such images could be used to extract acceleration of the liquid/gas interface. Single image systems exist at Iowa State University in the US, RWTH University of Aachen in Germany, and at the Colorado School of Mines (CSM) in Colorado (USA). All of these systems use time-gating and so most of them are based upon short pulse Ti:sapphire lasers (the picosecond Nd:YAG-based system at the Colorado School of Mines is the exception (Parker et al. 2012))."

Numerical Simulation of the Kerr Effect Time-gating

After primary investigations on effectiveness of Kerr effect time gating, we realized that in order to reach a significant improvement in image quality, careful design of the Kerr cell optical configuration needs to be conducted. In order to design the OKE (Optical Kerr Effect) shutter, a numerical model of the OKE time-gating was developed.

At the first step birefringence inside the cell was simulated. As a result of the strong electric field of the switching pulse, CS_2 molecules align with the polarization of the switching pulse, which result is a difference in the propagation velocity of the imaging pulse along two orthogonal axis, one parallel to the polarization of the switching pulse and the other

normal to that. Equation (1) predicts the difference in the refractive indices at position r is as a function of time (Idlahcen 2012):

$$\Delta n(\vec{r},t) = n_2 \int_{-\infty}^{t} I_p(\vec{r},t) \exp\left[-\frac{t-\tau}{\tau_0}\right] \left\{1 - \exp\left[-\frac{t-\tau}{\tau_r}\right]\right\} d\tau, \quad (1)$$

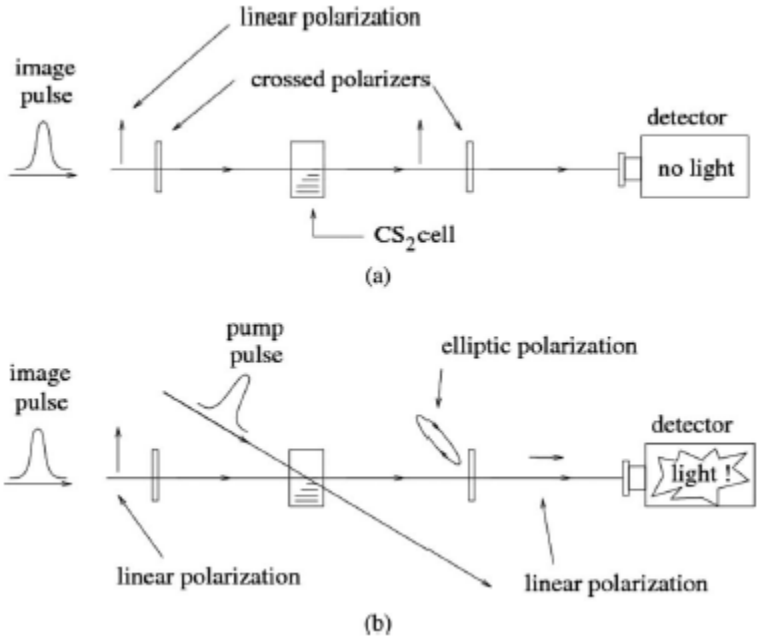

Figure 23- Principle of OKE time gating: (a) gate is closed, (b) gate is opened by pump pulse (source: Idlahcen 2012).

where n_2 (m^2/W) is the nonlinear optical index; τ_r corresponds to the rise time (response time of the molecules to the pump pulse electric field) and τ_0 to the relaxation time of the birefringence effect. I_p is the time-averaged envelope of the pump intensity. The pump pulse is Gaussian in time and space can be written as equation (2). I_{p0} is the maximum switching pulse intensity, and r_p and τ_p are, respectively, the spatial radius and time width of the switching pulse.

$$I_p(\vec{r},t) = I_{p_0} \exp\left[-\frac{r^2}{r_p^2}\right] \exp\left[-\frac{t^2}{\tau_p^2}\right], \qquad (2)$$

Inserting equation (2) into equation (1) and replacing the position vector with a (x,y,z) coordinates system in which z is the direction of propagation for the switching pulse , and calculating the integral results in equation (3).

$$\begin{aligned}\Delta n(\vec{r},t) = \frac{\sqrt{\pi} n_2 I_{p0} \tau_p}{2} \exp\left[-\frac{x'^2 + y'^2}{r_p^2}\right] \exp\left[\frac{\tau_p^2}{4\tau_0^2} - \frac{t - z'/v_p}{\tau_0}\right] \\ \times \left\{ \operatorname{erfc}\left[\frac{\tau_p}{2\tau_0} - \frac{t - z'/v_p}{\tau_p}\right] - \exp\left[\frac{\tau_p^2}{4\tau_r^2} + \frac{\tau_p^2}{2\tau_0\tau_r}\right. \right. \\ \left. \left. - \frac{t - z'/v_p}{\tau_r}\right] \operatorname{erfc}\left[\frac{\tau_p}{2\tau_r} + \frac{\tau_p}{2\tau_0} - \frac{t - z'/v_p}{\tau_p}\right] \right\}, \qquad (3)\end{aligned}$$

(x',y',z') here are deduced from any point (x,y,z) in the cell by a rotation of angle θ around axis y and v_p is the group velocity of the pump pulse, which can be calculated from equation (4) where c is the speed of light, $n(\lambda)$ is the refractive index of CS_2, and n_g is the group refractive index.

$$v_p = \frac{c}{n(\lambda_1) - \lambda_1 (dn/d\lambda)_{\lambda_1}} = \frac{c}{n_g(\lambda_1)}, \qquad (4)$$

As a result of the birefringence inside the Kerr cell, a phase difference, ΔΦ, occurs between two components of the imaging beam electric field along the polarization of the switching beam and orthogonal to it. The portion of the imaging pulse which transmits through the polarizer after the kerr cell can be calculated using the integral described in equation (5).

$$S(x,y,\Delta t) = \int_{t_1}^{t_2} I_i(x,y,t - z_e/v_i)\sin^2\left[\frac{\Delta\Phi(x,y,z_e,t,\Delta t)}{2}\right]dt, \tag{5}$$

The phase ΔΦ difference is calculated using Δn and integrating along the propagation path of the imaging pulse :

$$\Delta\Phi(x,y,z,t,\Delta t) = \frac{2\pi}{\lambda_1}\int_{-\infty}^{t} v_i dt' \Delta n(\vec{r},t' + \Delta t), \tag{6}$$

The parameter which determines the performance of the Kerr gate is the spatio-temporal transmission profile of the gate, which predicts the portion of the imaging pulse transmitting through the gate with respect to the delay and spatial coordinate from the center of the cell:

$$G(x,y,t) = \sin^2\left[\frac{\Delta\Phi(x,y,z_e,t,\Delta t)}{2}\right], \tag{7}$$

Figure 24 illustrates a calculated transmission curve of the imaging pulse through the Kerr gate we have been using in our experiments prior to the numerical simulations as a function of delay with respect to the switching pulse. At zero delay, when the imaging pulse

crosses the switching pulse right at the center of the cell, about 5% of the imaging pulse is transmitted through the Kerr cell. The parts of the imaging pulse that are delayed with respect to the switching pulse, which means they reach to the center of the cell after the switching pulse, are transmitted in a lower degree. The full width at half maximum (FWHM) of the transmission curve of the cell is 6 picoseconds, which is too long for effective scattering noise reduction, because most of the multiply scattered photons are still transmitted through the gate even though they are delayed for a few picoseconds because of the longer path they travel through the scattering medium. This finding indicated that it would be important to use different parameters for the cell in order to increase the peak transmission and reduce the temporal FWHM of the transmission curve.

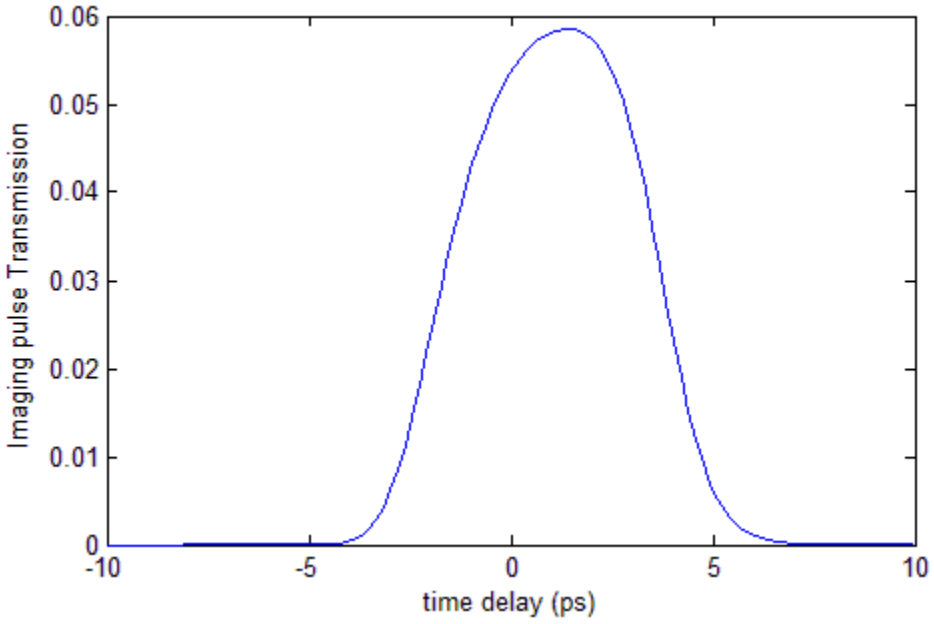

Figure 24- Numerical calculation of the transmission curve of a Kerr gate. Switching pulse properties: wavelength = 800nm, Energy = 0.5 mj, beam diameter = 5mm Imaging pulse wavelength: 400 nm, switching and imaging pulse duration: 2ps, CS_2 cell light path length = 10mm, Angle between imaging and switching beam = 10deg.

Figure 25 illustrates the same computations for Kerr gates with the same specifications except for shorter imaging light path length inside the Kerr cell. The results show that as shorter path lengths are used, the time for which the gate is open decreases, which is good for filtering scattering noise. However, the peak transmission also decreases, which results in smaller amounts of imaging light transmitting through the gate, and in the case of imaging through optically dense scattering medium this reduction might mean that there will no longer be enough

light to be recorded on the CCD detector. We can go from FWHM of about 5 ps for a 10mm long cell to about 2 ps for a 2mm long cell, but at the same time the peak transmission goes from 6 down to 1 percent. One way to compensate for the poor transmission of the Kerr gate could be using shorter duration switching pulses. Using shorter or more focused pulses increases the peak intensity at each pulse, which results in a greater transmission of the imaging pulses.

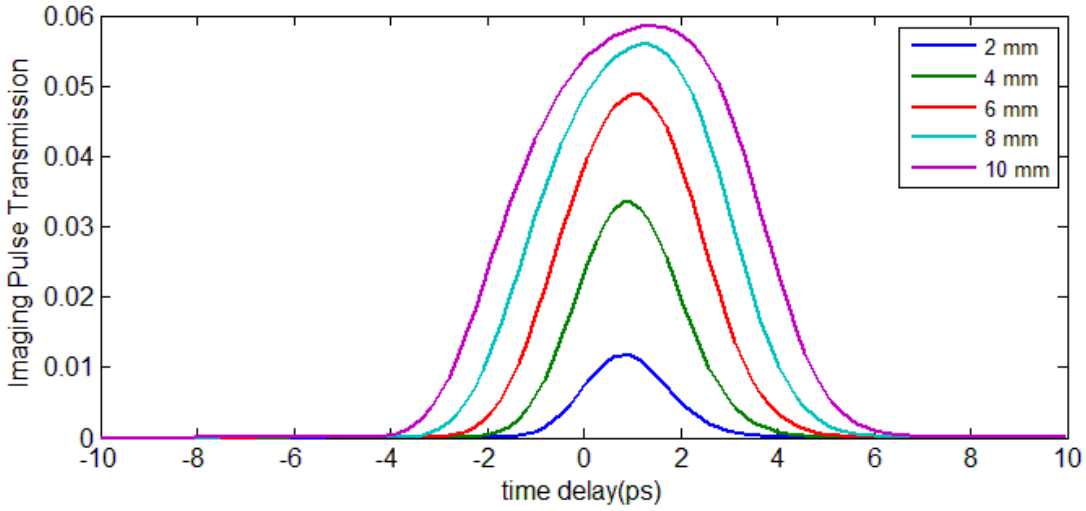

Figure 25- Numerical Calculation of the transmission curve of a Kerr gate with properties the same as figure 1 but with shorter light path lengths.

Numerical simulation of the Kerr cell transmission using different switching pulse durations for a 2mm long cell with the same switching pulse energy of 0.5 mj and 5 mm beam diameter is illustrated in figure 26. It is clearly observable that using shorter pulses increases the transmission of the imaging pulse up to three times while the time window for which the gate transmits imaging pulses gets even narrower.

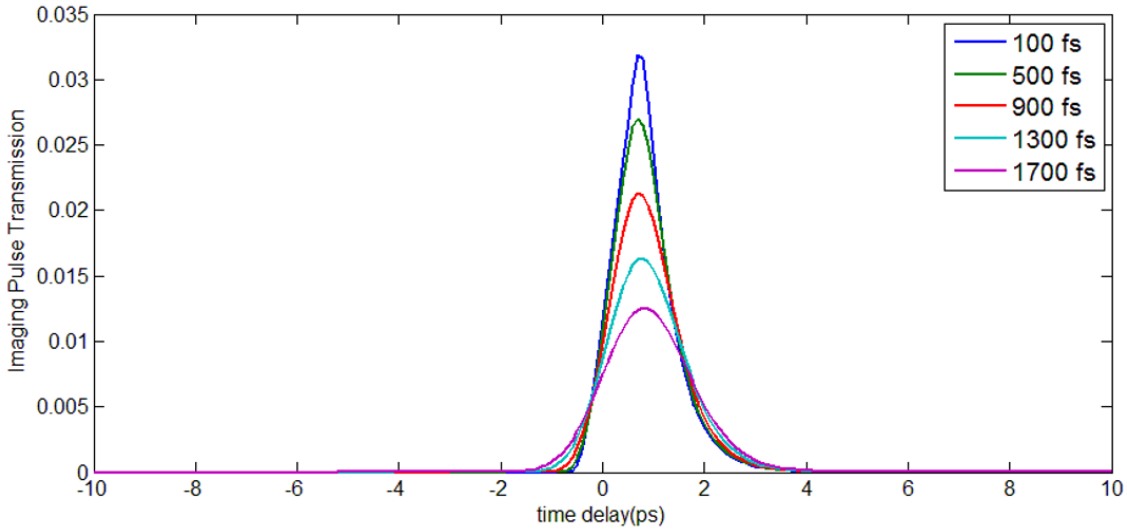

Figure 26- Numerical simulation of the Kerr cell transmission curve using different switching pulse durations for a 2mm long cell with the same switching pulse energy of 0.5 mj and 5mm beam diameter.

Another more effective way of increasing imaging pulse transmission through the Kerr gate is focusing the switching beam into the cell. In that situation the peak intensity of the switching pulse goes higher and results in higher transmission of the imaging pulse. As illustrated in figure 27, by focusing the switching beam down to 1 mm beam diameter, theoretically we should be able to get up to 90 percent transmission of the imaging pulse at the peak using a 2mm long Kerr cell and 1800 fs switching pulse. However, in addition to broadening the transmission window of the Kerr gate in time, focusing the switching beam

results in a smaller area of effective switching performance. In other words, as the switching beam cross section inside the Kerr cell gets smaller, we may need to focus the imaging beam inside the cell too in order to have a larger portion of it transmitted through the limited active switching area of the cell. This focusing action of both beams into the Kerr cell might result in sacrificing transmission of higher spatial frequency components of the imaging beam as they are positioned at further distances from the beam center while the imaging beam is focused into the cell, which is in fact performing a form of spatial filtering on the imaging beam. The inherent spatial filtering of this design can improve the scattering noise filtering, which increases the contrast of resolved images of the object field.

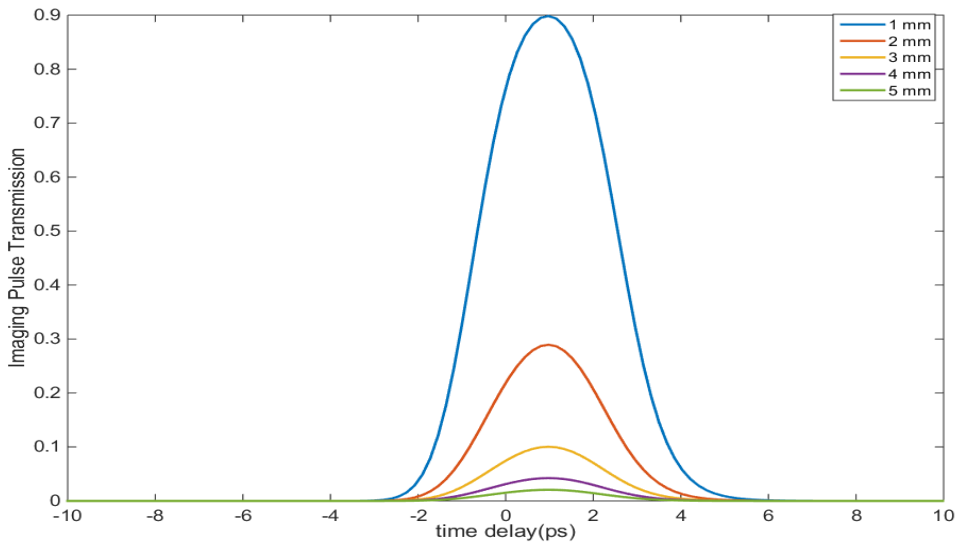

Figure 27- Numerical simulation of the kerr cell transmission curve using different switching pulse diameters for a 2mm long cell with the same switching pulse energy of 0.5 mj and 1800fs pulses.

All these numerical simulations demonstrated the value of a redesign of the Kerr gate setup in order to get higher imaging beam transmission and narrower transmission time window

for more effective filtering of the scattering noise. One improvement was to modify the Kerr cell from a glass precision cell to a design with glass flat windows and aluminum cell body with adjustable light path-length to test different cell length and find the optimum.

Experimental Measurements of the Kerr Effect Time-gating

Figure 28 demonstrates the experimental setup of Kerr effect ballistic imaging at UC Irvine. The light source is a Ti-Sapphire laser amplifier generating pulses of 800 nm center wavelength, 100 fs duration, and 1.2 mj energy with repetition rate of 1 kHz. A doubling crystal (DC) with conversion efficiency of about 50% generates pulses of the same duration but at center wavelengths of 400nm. Using these converted blue pulses for imaging has several benefits including improving the diffraction limit of the imaging system, but the most important reason to use two different wavelengths for imaging (400 nm) and switching (800 nm) is to be able to avoid the scattering light noise from the switching pulse inside the Kerr cell (KC) from degrading the image recorded on the CCD by placing a color filter (F) in the system, which only lets the blue light to transmit and reach the CCD while blocking the scattered IR light. M1-2 are the dichroic mirrors that are used to separate the blue light from the IR after the doubling crystal. Almost half of the original pulse (0.6 mj) is converted to blue light and is used as the imaging pulse, and the rest remains IR and serves as the switching pulse. Polarization of the IR beam coming out of the doubling box is mostly horizontal (p-polarized). Polarization of the blue light, on the other hand, is mostly vertical (s-polarized). Maximum transmission of the imaging pulse through the Kerr gate occurs when the angle between the polarization axis of the imaging pulse and switching pulse is 45 degrees. Therefore, a half-wave plate (WP) is used at the output of the doubling box to

rotate the polarization of the blue pulse 45 degrees. Mirrors M3-M5 are used to direct the imaging beam through the delay line. M4-5 are mounted on a translation stage (TS2) in order to adjust the pathlength of the imaging beam. P1-2 are Glan polarizers. P2 is adjusted 45 degrees from the plane of incidence and P1 is used to adjust the intensity of the imaging beam in order not to saturate the CCD. A USAF resolution chart is used as a test target with different spatial resolution components to be imaged on the CCD. A 1cm long glass scattering cell (SC) is placed right after the test target in order to simulate s the cattering condition in the formation region of a Diesel spray. The glass cuvette contains hydrosol of polystyrene particles. In the scattering cell depicted in figure 28, the 400 micron diameter metal needle at the center is veiled behind the scattering particles. The blue image on the right shows how the scattered beam hits a screen placed after the cell. The scattered slight is then collected with a lens (L1) which is placed twice the focal length apart from the USAF chart. There is an adjustable aperture (A) placed behind the lens to reduce collection of light scattered by the particles at larger angles (spatial filtering) and to adjust the numerical aperture of the imaging system. The light collected by the lens is then focused inside the Kerr cell (KC). The Kerr cell consists of an aluminum housing with two parallel glass windows. The space between the windows is filled with carbon disulfide (CS_2) liquid. A Glan polarizer (P3) is placed right after the lens allowing the transmission of light with polarization parallel to P2. Use of P3 is necessary since the lens slightly alters the polarization of the imaging beam whereas for Kerr effect gating we need the light to be perfectly polarized entering the Kerr cell. After transmitting through the Kerr cell, the imaging beam goes through another Glan polarizer (P4) which is set perpendicular to P3, as a result of which, the imaging beam is completely blocked in the absence of the

switching pulse. The switching beam is also directed through a delay line (TS1) and focused inside the Kerr cell. The path lengths of the two beams must be precisely matched using the delay lines in order for the imaging pulse and the switching pulse to cross each other inside the Kerr cell at the same moment. The strong electric field of the switching pulse aligns the CS_2 molecules with itself and the liquid acts like an instantaneous wave plate which rotates the polarization of the imaging pulse, as a result of which, some portion of the switching pulse transmits through P3 at the presence of the switching pulse. The detector used in this setup is a 1.3 megapixel cooled Hamamatsu CCD array.

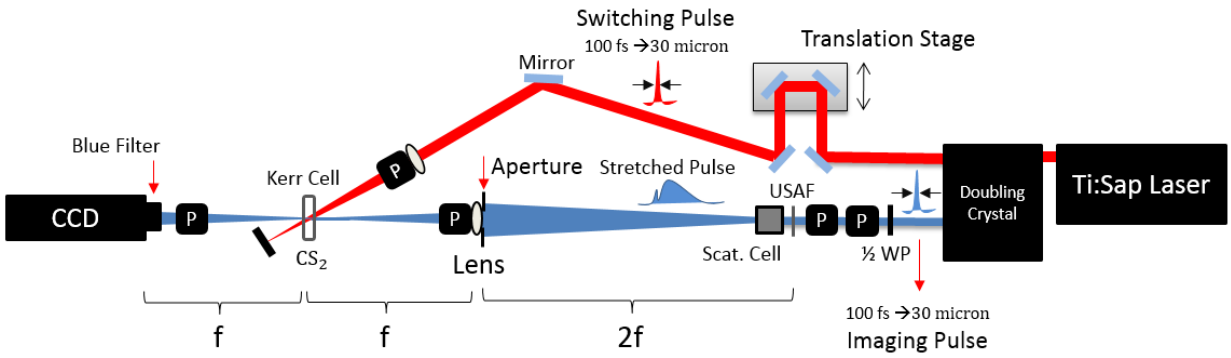

Figure 28- Schematic of the Kerr effect Ballistic imaging Setup at UC Irvine

After conducting the numerical simulation studies on the Kerr cell design parameters we also investigated various cell design parameters experimentally to figure the most practical cell design. Figure 29 illustrates the transmission curve for Kerr cells with different imaging light path lengths. Glass cuvettes of various lengths were used as CS_2 containers. For all of the experiments the same switching pulse with 1800 fs pulse duration, 5 mm beam diameter, 0.5 Joules per pulse energy, and 800 nm center wavelengths were used.

The imaging pulse properties was also similar in all cases with the same 1800 fs pulse duration, 4 mm beam diameter, 100 μw beam power at open gate condition, and 400 nm center wavelength with a 10 degree angle between the switching and imaging beam. At this stage the lenses were removed from the imaging and switching beams' path and the two beams crossed each other in the Kerr cell without being focused inside the cell. As expected from the simulations, decreasing the imaging light path lengths inside the cell from 10 mm to 1 mm reduces the peak power transmission from 25 percent to 2.5 percent while shortening the full width at half maximum (FWHM) transmission from 11 ps to 2 ps.

The pathlength inside the Kerr cell is especially important when the two waves have different wavelengths and therefore different group velocity in the CS_2 liquid. For the case of an 800 nm switching wave and 400 nm imaging wave the blue wave travels faster in the Kerr cell than the IR pulse and therefore the imaging pulse catches up with the switching pulse even when it is delayed. This phenomena results in a longer transmission window for the imaging wave through the Kerr cell. A short path length inside the cell helps to shorten this transmission window since the imaging pulse has only a short time and space to catch up and pass through the switching pulse inside the cell in CS_2 liquid.

A 2 mm Kerr cell seems to be a compromise choice with a maximum transmission of 11 percent and FWHM transmission of 4 ps. However, both the maximum and FWHM transmission still are poor compared to what is required for efficient scattering noise reduction. Therefore we decided to work on another critical design parameter which is the switching pulse duration. We had our Ti-Sapphire amplifier redesigned to shorten the

delivered pulse durations to 100 fs with the same pulse energy which makes the switching peak power more than 20 times higher than the previous design. As illustrated in Figure 30, with all the other Kerr gate design parameters the same as the previous design, we were able to get more than twice the transmission out of the Kerr gate using 100 fs pulses compared to the old design with 1.8 ps pulses. FWHM transmission at the same time is reduced by a factor of two which makes the 100 fs design a significantly more efficient choice for the highly scattering noise reduction time-gating.

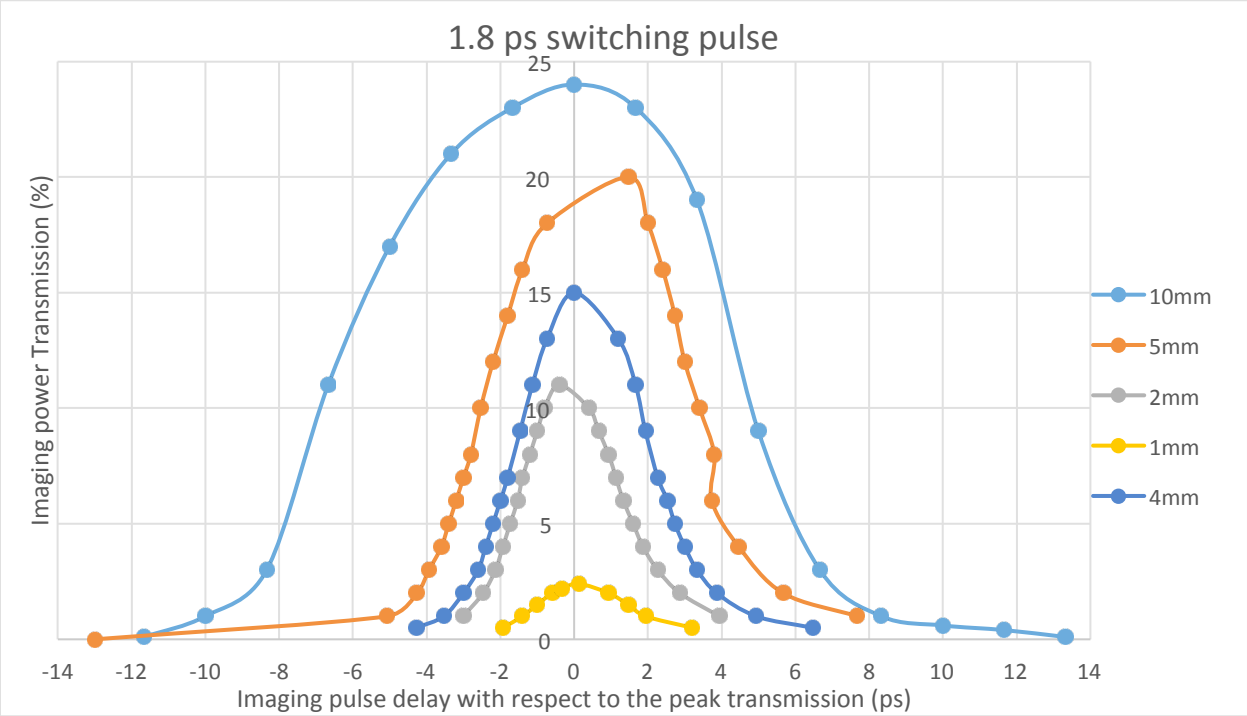

Figure 29- Transmission curve of Kerr gates using 1.8 ps switching pulses and various cell lengths.

In order to get even higher transmission rate out of the Kerr gate one further possibility is to reduce the effective switching area by focusing the two beams into the cell. Figure 31 demonstrates that by focusing the two beams into 1mm diameter cross section area the

transmission improves by a factor of 5, which is convenient especially for cases of imaging through ultra-high density scattering media where the amount of transmitted light can fall below that needed for single shot imaging in case of low transmission rate of the Kerr gate. The FWHM transmission time on the other hand is increased, which is a sacrifice in the case of high scattering noise.

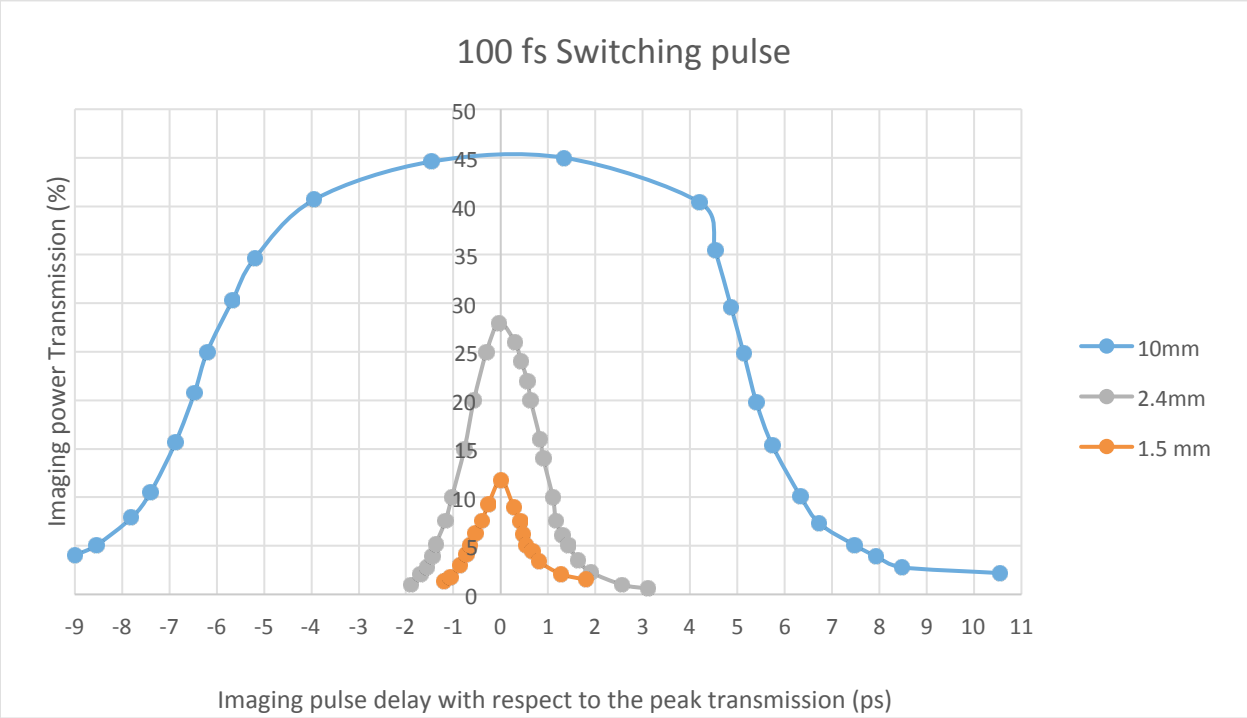

Figure 30- Transmission curve of Kerr gates using 100 fs switching pulses and various cell lengths

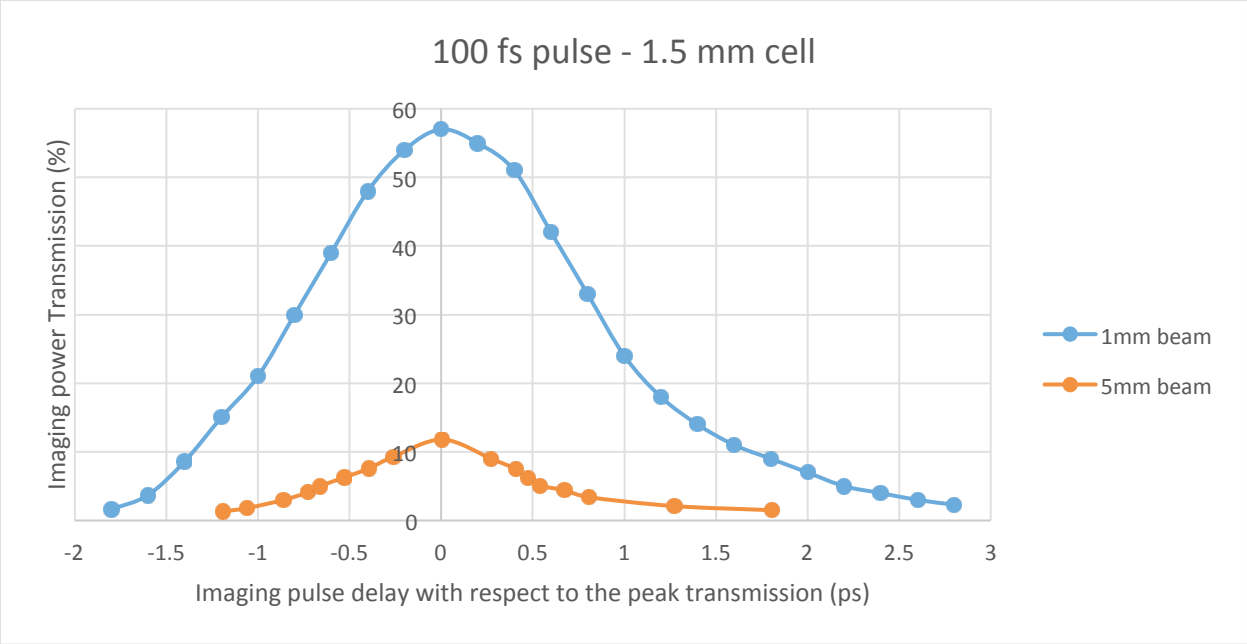

Figure 31- Transmission curve of Kerr gates using 100 fs switching pulses and 1.5 mm long cell with two beams being focused into a smaller cross section area (1mm) in the blue curve case.

The measured transmission of the final Kerr cell design with 1.33 mm cell length, 100 fs pulse duration and focused beams inside the cell, and the corresponding numerical simulation of it is depicted in figure 32. Maximum transmission of the imaging pulse is around 40% in both the simulation and experimental measurement, while the temporal FWHM transmission window is around 1.1 ps in both cases. This final design is used for imaging through scattering cells with various characteristics to investigate the effectiveness of Kerr effect ballistic imaging through highly scattering media and to compare the BI performance with other methods, such as spatial filtering and ultra-short pulse digital holography. The results of these methods and the comparison are presented in the following chapter.

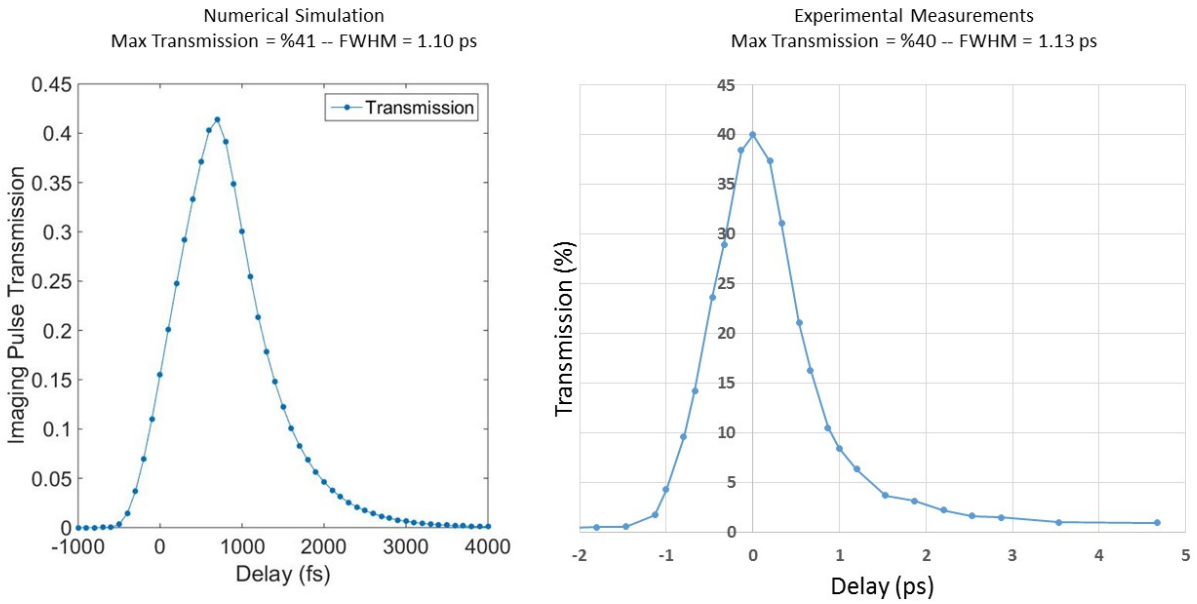

Figure 32 – The measured transmission of the final Kerr cell design (right) with 1.33 mm cell length, 100 fs pulse duration and focused beams inside the cell, and the corresponding numerical simulation (left).

CHAPTER 5

Results and Discussion

In this chapter the results are presented of imaging a USAF resolution chart veiled behind highly scattering media contained in an optical cuvette cell. The media characteristics were varied, including scattering particles' size, number density of scattering particles, and optical depths. Four different optical techniques were explored: (1) inline digital holography, (2) off-axis digital holography, (3) spatial filtering imaging using an optical lens and aperture, and (4) time gating with the optical Kerr effect for ballistic imaging with and without an aperture. The ultimate goal is, for the first time, to compare between the effectiveness of these techniques to overcome the scattering noise in different quantifiable light scattering situations. More than 10 different scattering cells using polystyrene particles of different sizes suspended in water were generated and used to obtain the results. This type of scattering media is commonly used in studying multiple-scattering effect of droplet clouds in the spray diagnostics community (Linne 2013) because they are steady, reproducible, and sufficiently uniform for theoretical analysis and prediction. The optical depths of scattering cells (OD) were determined both analytically, using the scattering cross-section of the polystyrene particles in water and their number density according to the Beer-Lambert law, and experientially, measuring the ratio of non-scattered transmitted light to the incident light using optical power meters. Due to the the inherent difficulties and errors of measuring the true local number density of scattering particles and the intensity of non-scattered light (e.g., separating forward scattered light

from unscattered light ending up at the same detector location), the measured optical depths have an error of up to OD $\pm$1. Despite this absolute uncertainty (a characteristic rarely mentioned in the literature) these optically dense solutions provide a comparative environment capable of demonstrating the effectiveness of any of the tested techniques relative to each other as the very same scattering cells were used to obtain the results in all the techniques. The OD measurement inaccuracy makes it difficult to compare between the results of different experiments presented in the literature especially because the details of measurement methods used and error analysis for optical depth are rarely included. For example, one key characteristic of the scattering condition, in addition to the optical depth, is the size of scattering particles, which is not carefully addressed in most of the literature. All the above mentioned difficulties in creating absolute criteria for similar scattering conditions in laboratories, makes it extremely valuable to set up different techniques at the same laboratory in order to use the very same scattering conditions as the basis for comparison between the effectiveness of different imaging techniques. This inter-method comparison is one of the key contributions of this dissertation research.

Ultra-short Pulse Off-axis Digital Holography in Scattering Media

The first technique discussed here is ultra-short pulse digital holography. 100 fs doubled frequency (from 800 nm doubled to 400 nm wavelength) pulses of a Ti:Sapphire amplifier are used to record digital holograms of a USAF resolution chart on a CCD detector. A scattering cell disturbs the imaging (object) wave on its path from the target to the CCD to simulate highly scattering conditions. Figure 33 demonstrates examples of holograms and reconstructed images of USAF test target when no scattering cell is placed in the path of

imaging beam. A normal optical shadow lens image of the test target made with the same light source is also included for comparison. This comparison image is what typical optical camera approach would produce. The focal length of the lens is 50 mm and the target and the CCD are placed 100 mm from the lens on opposite sides (i.e., a 4f setup). In reconstruction of any inline Gabor hologram the out of focus twin (conjugate) image of the object degrades the contrast of the reconstructed image. In off-axis holography, however, the conjugate wave is eliminated by filtering in the frequency domain, which results in better contrast reconstruction.

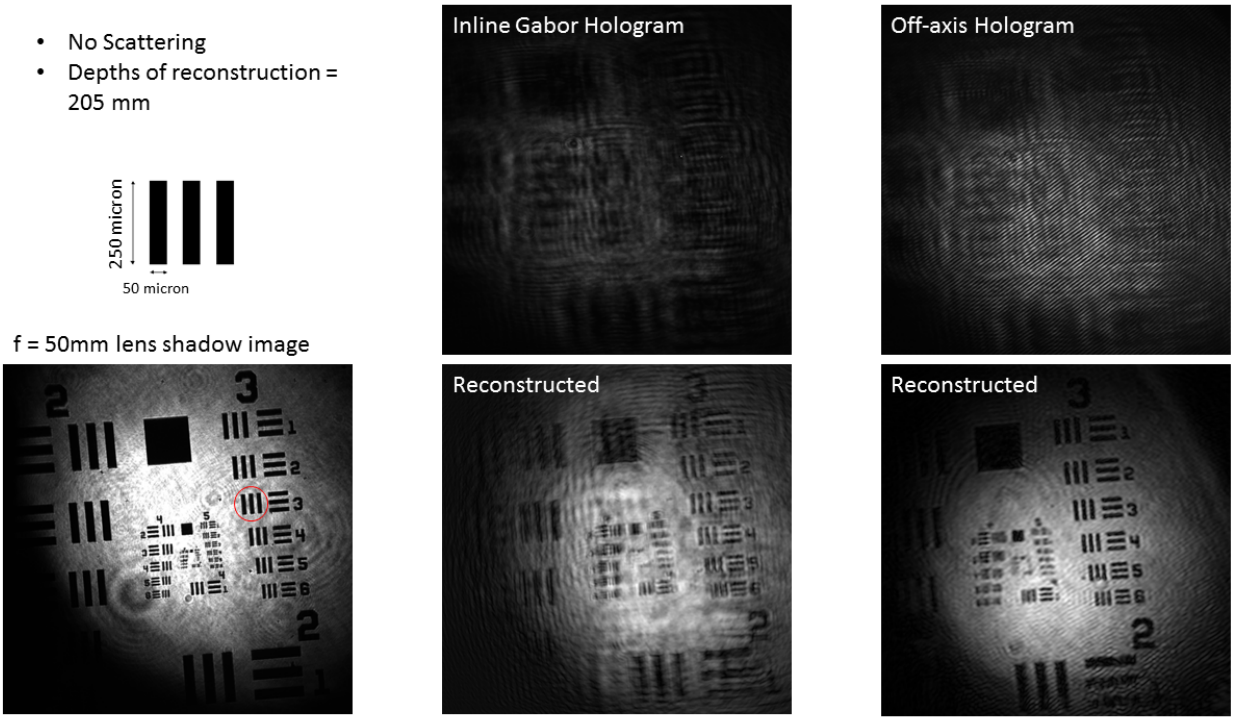

Figure 33 – Holograms and reconstructed images of USAF test target.

Figures 34, 35, and 36 show a comparison between shadow imaging using an optical lens, inline Gabor digital holography, and off-axis digital holography, all using 100 fs pulses of

blue (400 nm) light, looking at the USAF test target through a highly scattering environment. Even though in the case of no scattering cell the shadow images made with the lens look clearly better compared to the reconstructed holograms (figure 33), when the scattering cell is added, holography results in a considerably better image contrast. The higher the optical depth of the scattering cell is (as a result of greater number density of scattering particles), the difference between holography and shadow imaging with a lens is more significant. Because there is relatively sparse literature in ultra-short pulse holography, the reason for the contrast improvement has not been discussed in detail. Based on the work contained in this dissertation, however, it appears that the ultra-short coherence lengths of the light source can explain the improvement in contrast. In imaging the shadow using a lens, the light scattered by the particles reduces the signal to noise ratio of the recorded image on the CCD, which results in poor contrast. Holograms are shaped when the imaging wave interferes with the undisturbed reference wave:

$$(1) I_{hol} = |Img + Ref|^2 + |S|^2 = |Img|^2 + |Ref|^2 + Ref^* \times Img + Img^* \times Ref + +|S|^2$$

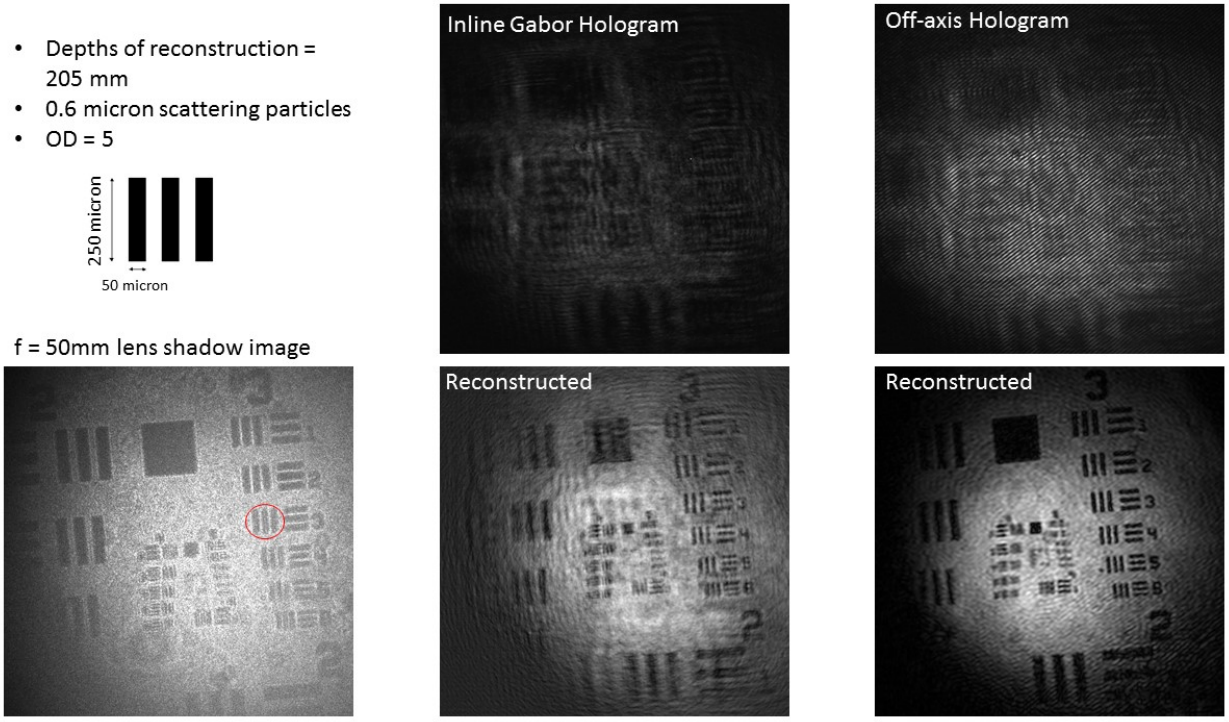

Figure 34 – Holograms and reconstructed images of USAF test target veiled behind OD 5 scattering hydrosol of 0.6 micron polystyrene particles.

S in equation (1) is the light scattered by the particles which is assumed to be no longer coherent with the imaging and reference wave and therefore it is just added to the intensity recorded on the hologram and does not interfere with the other waves. In the case of off-axis holography $Ref^* \times Img$ can be separated from the other terms in the frequency domain (figure 19) and from there the imaging beam phase and amplitude can be retrieved and the image of the object can be reconstructed. In the case of inline Gabor holography there is no separate reference beam, but the imaging wave itself consists of a part diffracted by the object, Img_O, and a part which is undisturbed that acts like a reference wave, Img_R. These two parts of the imaging wave interfere with each other and form a hologram which is recorded on the CCD:

$$I_{hol} = |Img|^2 + |S|^2 = |Img_R + Img_O|^2 + |S|^2$$
$$= |Img_R|^2 + |Img_O|^2 + Img_R^* \times Img_O + Img_R \times Img_O^* + |S|^2.$$

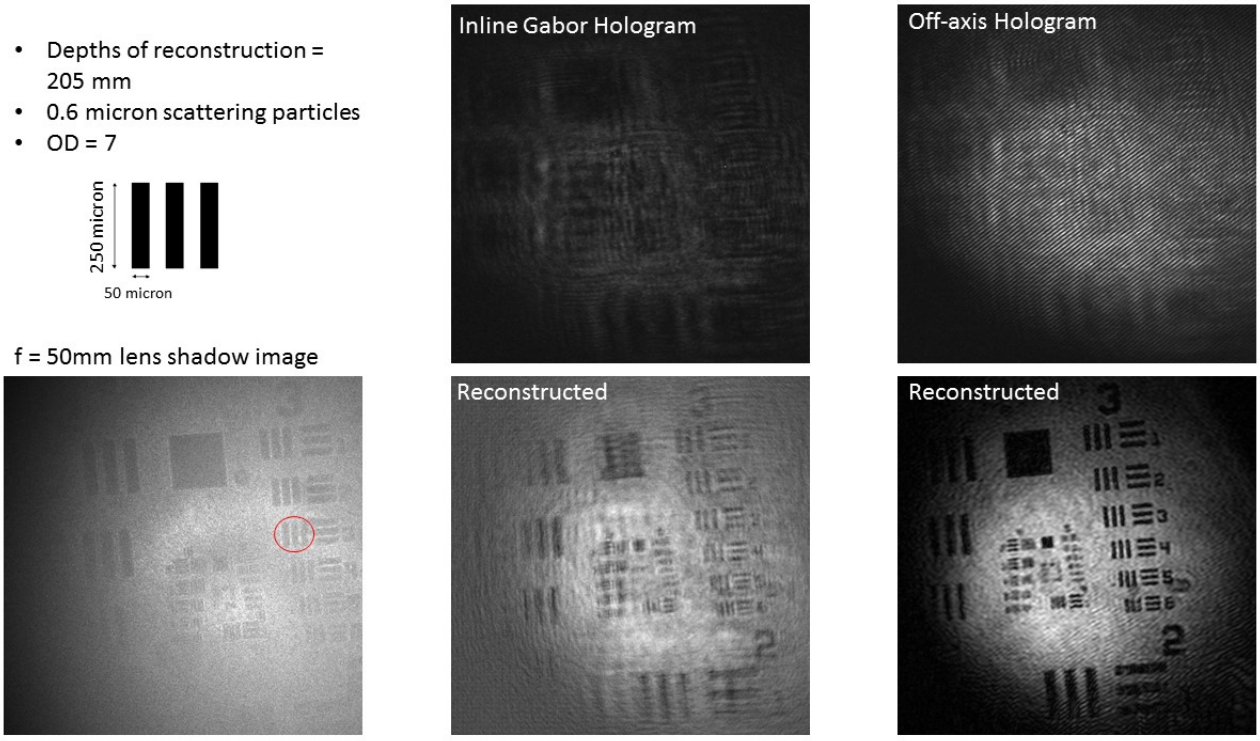

Figure 35 – Holograms and reconstructed images of USAF test target veiled behind OD 7 scattering hydrosol of 0.6 micron polystyrene particles.

This time though, as opposed to the off-axis hologram, the DC and conjugate cross terms are not separated in the frequency domain and they degrade the reconstruction. In low or moderate scattering condition Img_R is relatively large compared to S and Img_O. Therefore, all DC terms are relatively small compared to the terms that are multiplied by Img_O. This explains how inline holography helps to improve the signal to noise ratio in low and moderate scattering conditions (figures 34 and 35). In cases of severe scattering conditions though, S is much larger than Img. This is when the use of a separate off-axis reference wave becomes necessary to increase the amplitude of the reference and to be able to separate the cross term in the frequency domain and filter out most of the scattered noise in the reconstruction process. In the case of OD 9 scattering (figure 36) the USAF chart is completely covered by the scattering cell when being imaged using a lens. Making an inline

Gabor hologram is not sufficient to retrieve the lost image of the object, even though it helps. Using a separate off-axis reference wave, however, significantly improves the contrast of the reconstructed image. Figure 37 demonstrates similar results for 6 micron diameter scattering particles. The most important difference between these particles and the 0.6 micron particles that were previously discussed for this problem is their Mie scattering profile. The size factor of 6 micron particles for 400 nm wavelength light is 15, whereas it is 1.5 for 0.6 micron particles.

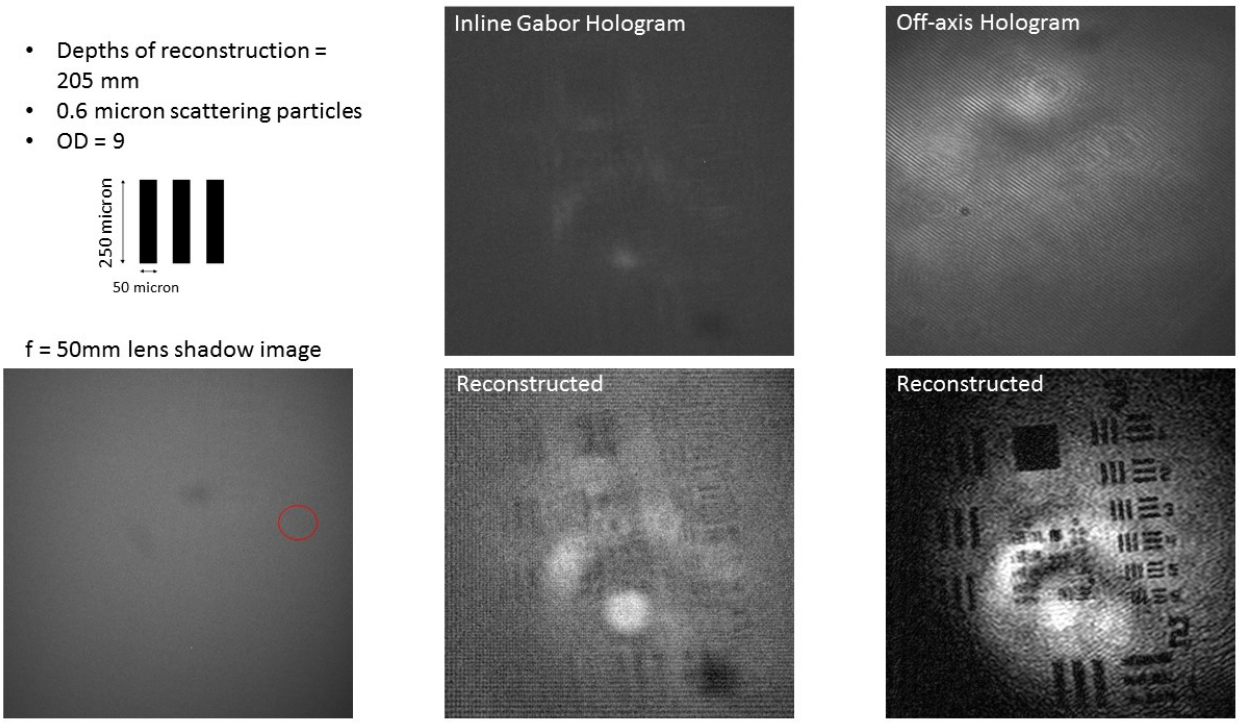

Figure 36 – Holograms and reconstructed images of USAF test target veiled behind OD 9 scattering hydrosol of 0.6 micron polystyrene particles.

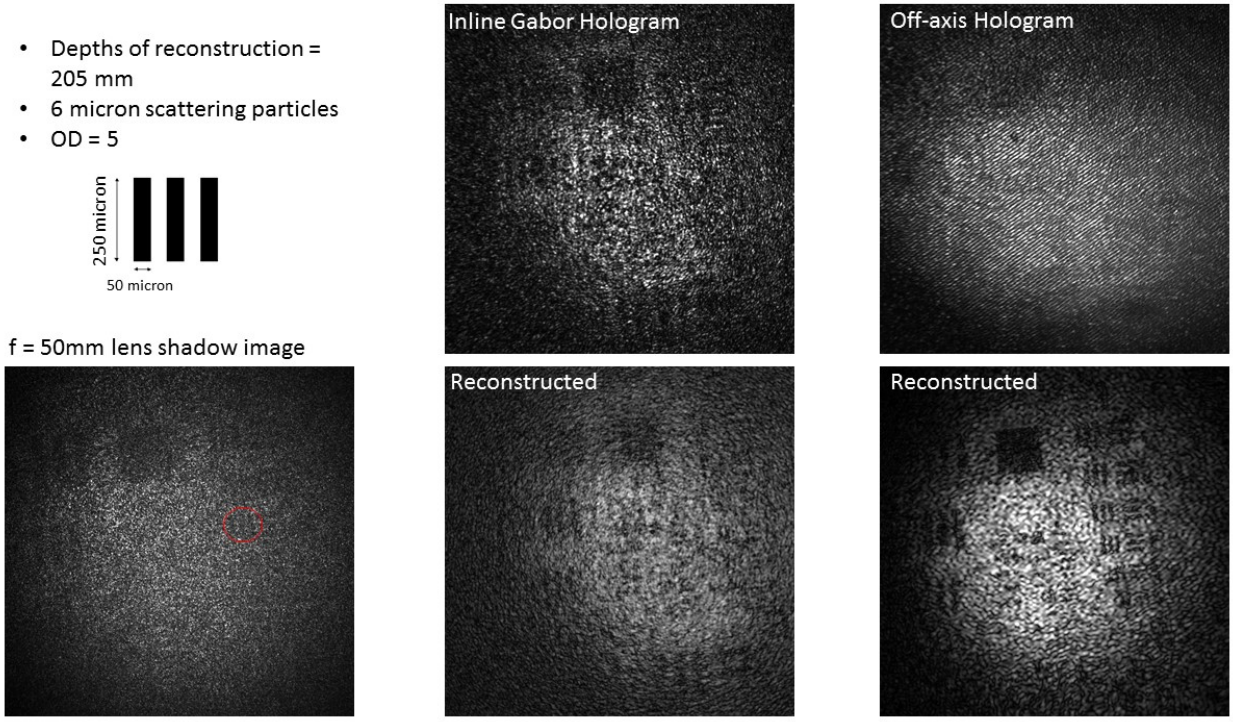

Figure 37 – Holograms and reconstructed images of USAF test target veiled behind OD 5 scattering hydrosol of 6 micron polystyrene particles.

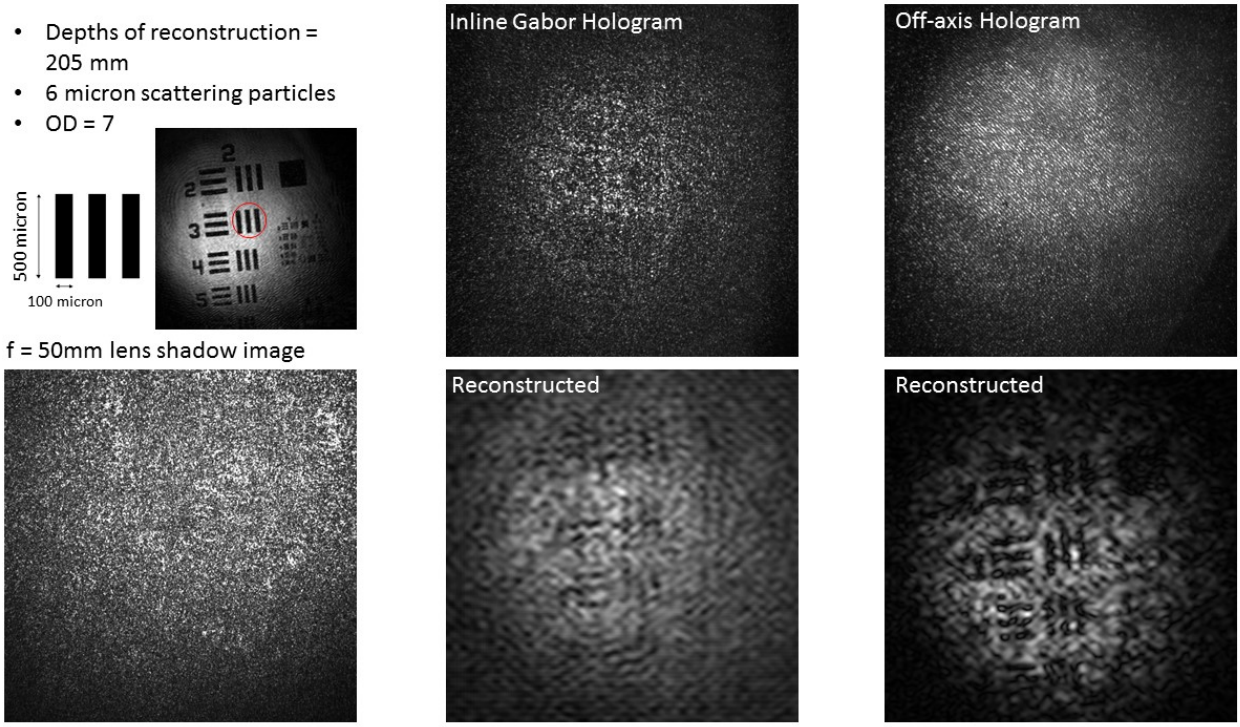

Figure 38 – Holograms and reconstructed images of group 2 of USAF test target veiled behind OD 7 scattering hydrosol of 6 micron polystyrene particles.

This relatively large size factor results in a much greater forward scattering lobe in the Mie scattering profile of the particle. Forward scattered photons travel a shorter path through the scattering medium and many of them are still partially coherent with the undisturbed reference wave. These group of photons interfere with the reference wave and some of the other scattered photons, which makes the coherence filtering less effective. The speckles observable in both inline and off axis holograms and their reconstructed images are a result of this random interference. The other difficulty associated with relatively large scattering particles is their relative size with respect to the features in the object field (e.g. liquid core structure in Diesel sprays, or the USAF test target in the results presented here). Smaller ratios of target feature size to scattering particles' size make spatial filtering inherent in the reconstruction process less effective to resolve the target. That is because, in the process of extracting the cross term from the recorded hologram in the frequency domain (figure 19), the size of the evaluation square area around the cross term signal in the frequency domain determines the smallest feature resolved in the reconstructed image. That is, the larger the square including the cross-term, the higher the resolution. Therefore, the referred-to square should be chosen big enough to contain high frequency components of the object beam needed for resolving smaller target features in the object field. At the same time, higher frequency components, which contain noise from the scattering particles and speckles, should be avoided by not choosing a square larger than is needed. Choosing a properly sized zone of exclusion for extracting the cross term is not feasible if the ratio of target size to scattering particle is small especially when the scattering environment is very dense (OD > 6). Therefore in the result presented in figure 38, for instance, group 2 of the USAF resolution chart, which contains larger elements

compared to group 3, is used as a target. In comparison with lens shadow imaging and inline Gabor holography, the off-axis holography has resolved the target elements with a significantly higher contrast.

Going to higher optical depths (like OD 10) with 6 micron scattering particles, a 400 micron diameter needle is used as target in the results presented in figure 39. The problem of imaging through such a dense scattering environment is more than multiple scattering noise, which is mostly overcome with coherence filtering. The other barrier in such cases seems to be that the scattering media is so dense that the scattering 6 micron particles are placed close enough to each other that their collected clusters form an opaque wall that covers objects as large as a few hundred microns. That is, even if the multiply scattered photons are perfectly filtered, the single scattered photons off the scattering particles in such a dense environment cannot penetrate the larger composite obstacles, which prevents the image of the target object to be resolved properly. In the reconstructed image of the off-axis hologram in figure 39, only a vague shadow of the target needle is visible behind the randomly shaped threads comprised of scattering particles.

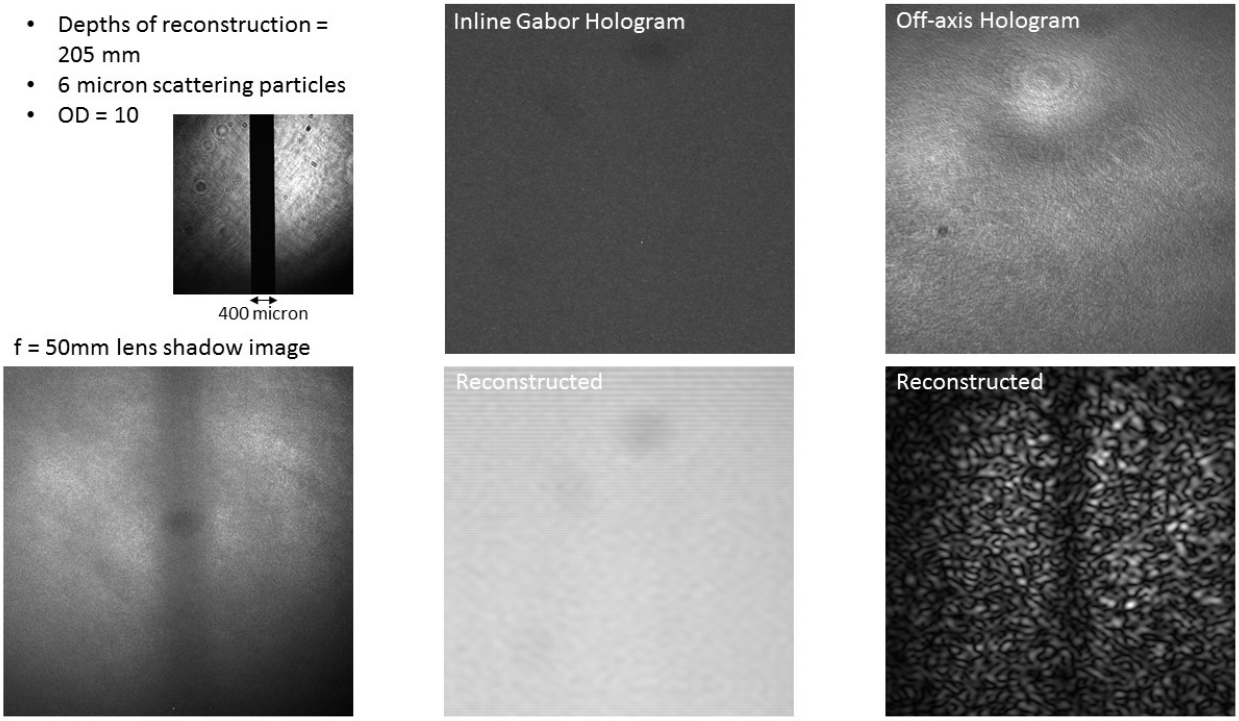

Figure 39 – Holograms and reconstructed images of a 400 micron diameter needle veiled at the center of an OD 10 scattering hydrosol of 6 micron polystyrene particles.

Coherence Filtering versus Spatial Filtering

As explained earlier, there is low pass spatial frequency filtering inherent in the process of reconstructing an off-axis digital hologram. On top of that, as a result of the limited size of an ultra-short pulse digital hologram (explained in chapter 4), the numerical aperture and resolution of the reconstructed image are also limited. In order to investigate how much of the improvement observed in DH (previous section) is because of the inherent low pass spatial frequency filtering in off-axis DH, and how much of it is a result of ultra-short pulse coherence filtering, shadow images of the USAF test target were recorded using an adjustable aperture placed at the optical lens plane. This permitted the system to match the numerical aperture of the lens images with that in the reconstructed digital holograms. Results demonstrated in figure 40 show the comparison between shadow images made

with the aperture, shadow images made without the aperture, and reconstructed digital holograms. The numerical aperture is matched for DH and aperture lens imaging. In addition to that, the same low pass filters have been applied in the frequency domain of all images in order to demonstrate a fair comparison between them. Using an aperture at the lens plane reduces the numerical aperture of the imaging system. The aperture used to capture the images in the 2nd is adjusted to a diameter of 2.25 mm. An optical lens with focal length of 50 mm is used to form the images. The test target and CCD detector are placed 100 mm apart from the lens at opposite sides, which forms a 4f imaging setup with magnification of 1 and numerical aperture of 0.01125. The size of the holograms used for reconstruction are matched with the diameter of the aperture, and the depth of reconstruction is matched with the distance between the lens plane and image plane (100 mm) in order to acquire the same numerical aperture as the aperture lens system. The angle between the object wave and the reference wave constructs a fringe spacing of 25 microns in the off-axis digital holograms, which is large enough for the interference pattern to cover all of the hologram. The Abbe diffraction limit ($d = \frac{\lambda}{2NA}$) for this imaging system is equal to 18 microns, which matches the size of the smallest element in group 4 of the USAF test target. Group 4 of the USAF chart is resolved in all cases in figure 40 showing that the imaging systems are diffraction limited. Using an aperture improves the contrast of images captured through highly scattering media compared to the ones made with no aperture. However, this improved contrast is achieved by sacrificing the spatial resolution, as some smaller elements of the test target are not resolved in aperture lens images. In reconstructed digital hologram images (bottom row), on the other hand, both good

contrast and diffraction limited resolution are achieved at the same time as a result of the coherence filtering inherent in off-axis DH, as explained earlier.

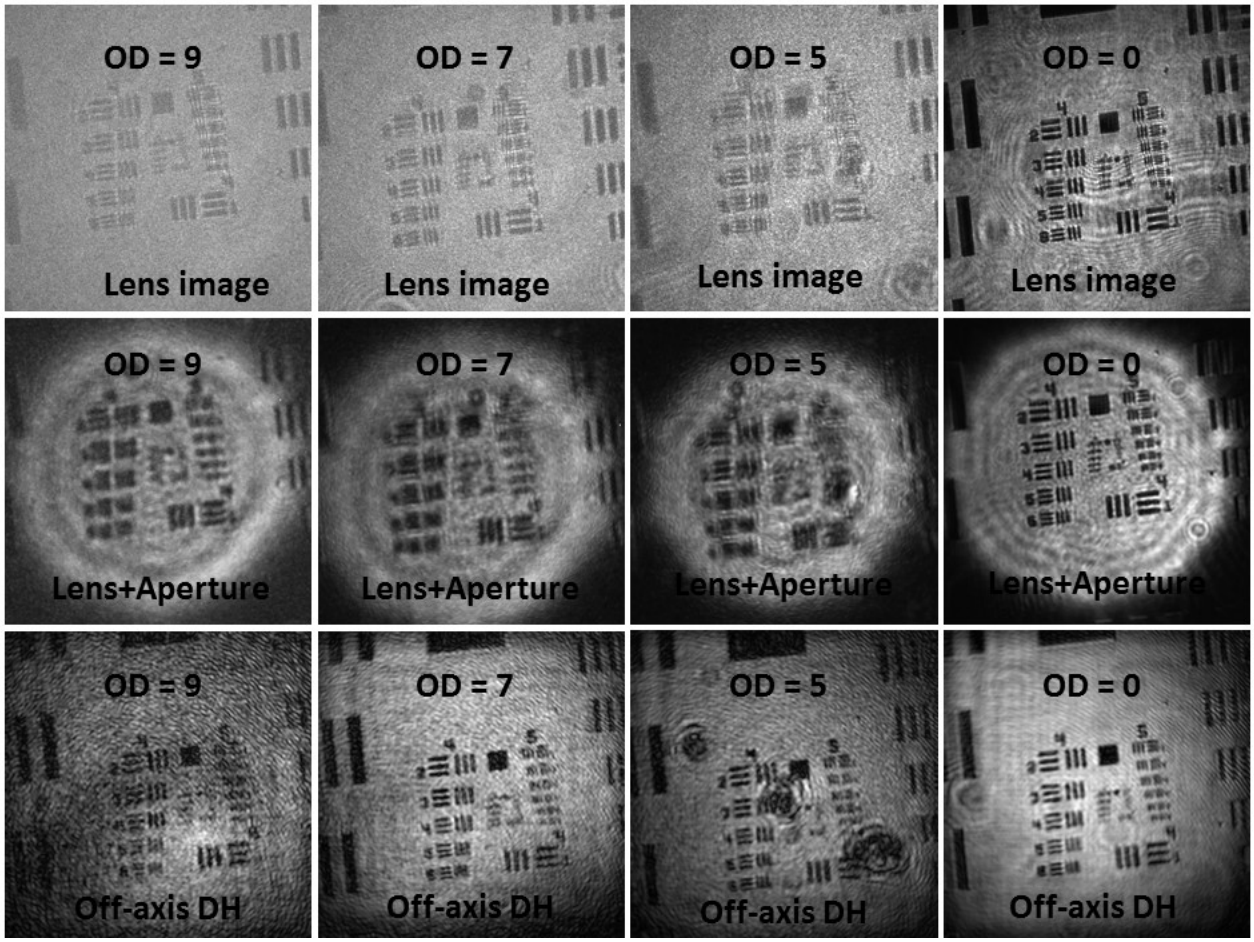

Figure 40– Holograms and reconstructed images of group 4 of USAF test target veiled behind scattering hydrosol of 0.6 micron polystyrene particles compared with shadow images made with a f = 50 mm lens (4f setup) and an aperture placed at the lens plane. Numerical aperture of both holograms and aperture lens system is matched at 0.01125.

Figures 41 and 42 demonstrate similar results made using 6 micron scattering particles and different groups of elements on the USAF resolution chart. The results show clearly that off-axis digital holography provides better contrast and resolution compared to shadow imaging using an optical lens with identical numerical aperture especially at harsh scattering conditions.

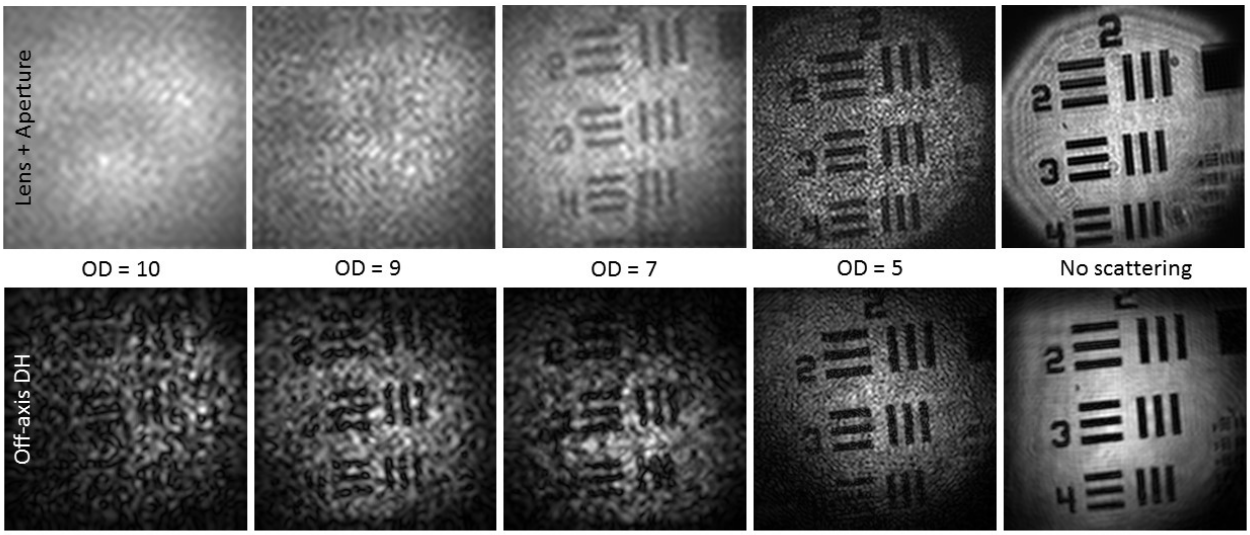

Figure 41– Holograms and reconstructed images of group 2 of USAF test target veiled behind scattering hydrosol of 6 micron polystyrene particles compared with shadow images made with a f = 50 mm lens (4f setup) and an aperture placed at the lens plane. Numerical aperture of both holograms and aperture lens system is matched at 0.015.

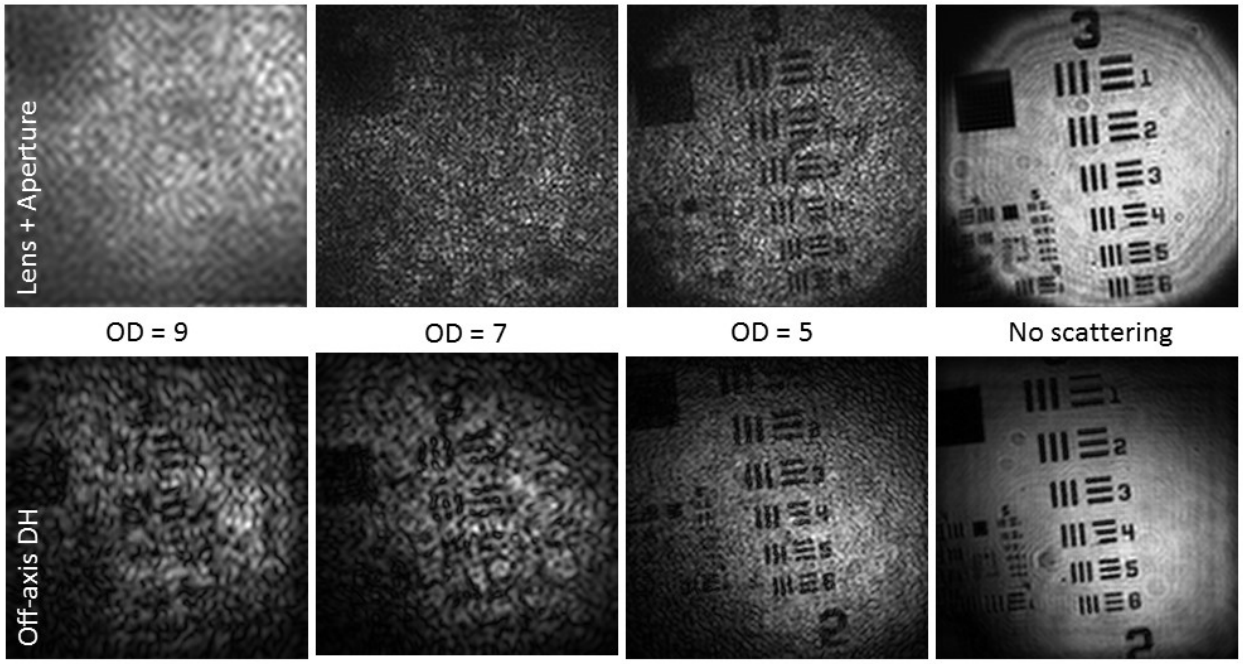

Figure 42– Holograms and reconstructed images of group 3 of USAF test target veiled behind scattering hydrosol of 6 micron polystyrene particles compared with shadow images made with a f = 50 mm lens (4f setup) and an aperture placed at the lens plane. Numerical aperture of both holograms and aperture lens system is matched at 0.015.

3D Imaging Capability of Digital Holography

One significant advantage of digital holography over optical imaging using a lens is the capability of reconstructing a single digital hologram at various depths and creating a 3D image of the object field. Figure 43 demonstrates a digital hologram of a field of 40 micron glass particles in water reconstructed at two different depths. At each reconstruction depth some particles are resolved in focus and others are out of focus. By detecting the depth at which each particle is in its best focus, a 3D model of the particle field can be reconstructed. While the top row in figure 43 is captured in a condition where only 40 micron particles are in the field, the bottom row is acquired at a condition where 40 micron particles are surrounded by 0.6 micron polystyrene particles which partially simulate the turbid medium of dense sprays. The number density of small polystyrene particles is much higher than for the larger glass particles. The optical depth generated by the small particles is measured to be approximately OD 8.

The results indicate that even in harsh scattering conditions the off-axis ultra-short pulse digital holography technology is capable of depth detection for the relatively large objects in the field. This 3D feature is especially important for looking at the 3D structure of the liquid core in the formation region of dense sprays.

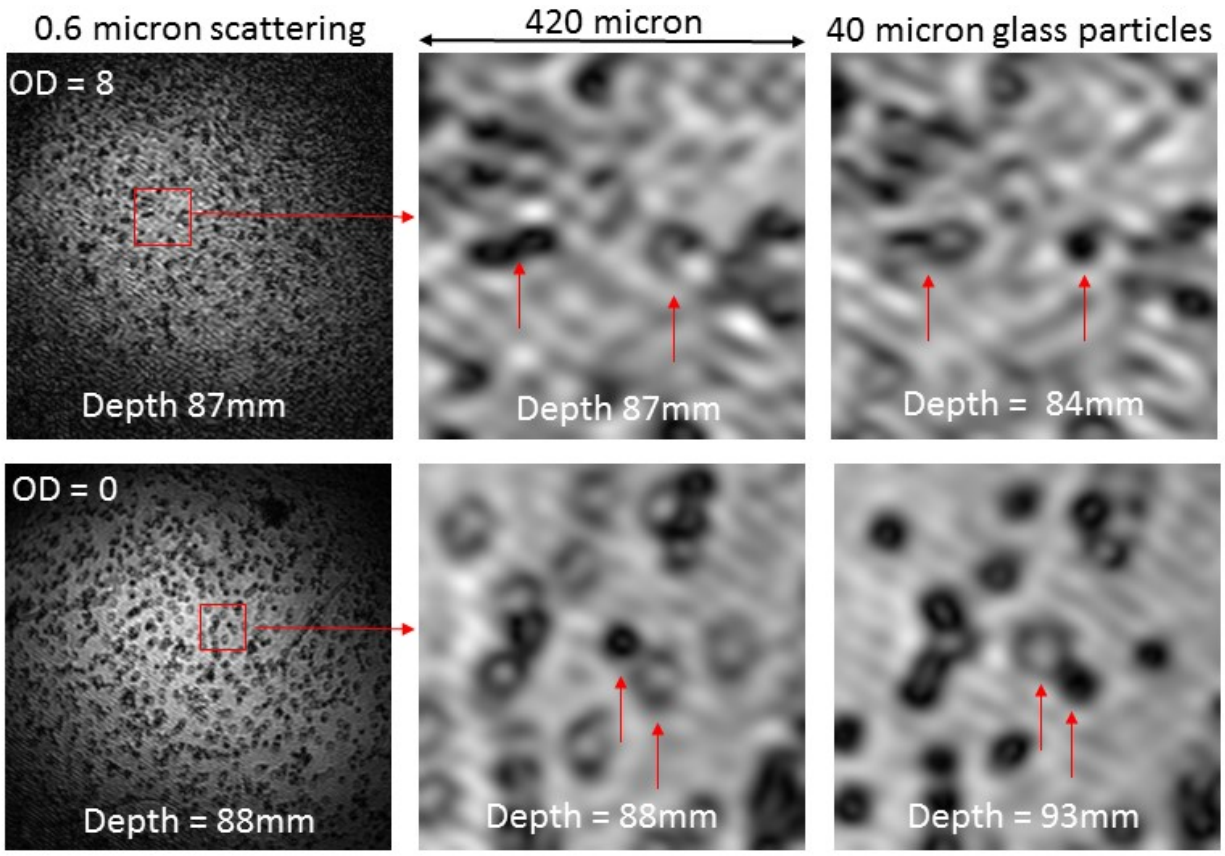

Figure 43- reconstructing an off-axis ultra-short pulse digital hologram of a field of 40 micron glass particles in water at different depths.

Kerr Effect Ballistic Imaging in Scattering Media

As mentioned in previous chapters, Kerr effect ballistic imaging is the most promising state of the art technology being used at various research labs around the world for imaging the fluid structure inside the formation region of dense sprays (Linne 2013). Ultra-short pulse off-axis digital holography that is proposed for the same application in this dissertation has never been mentioned in the literature as an effective technology to overcome the multiple scattering noise in the formation region of dense sprays. In order to prove the effectiveness of the proposed technology, a state of the art Kerr effect ballistic imaging setup was designed and built at UC Irvine. The setup has been optimized using numerical simulations and experimental investigations in order to show the best possible performance for the

goal application (details in chapter 5). Figure 44 demonstrates images made with the ballistic imaging setup. A 4f imaging setup with magnification of 1 using a 1 inch diameter convex optical lens with focal length of 200 mm is used to record the presented images. The row on the bottom is made when the polarizers before and after the Kerr cell (P3 and P4 in figure 28) are set parallel and the switching beam is blocked before the cell. This mode of the system is called 'open gate', which means that most of the light transmitted through the scattering cell can continue on its path to the CCD detector. The 'open gate' mode is actually a shadow imaging system making use of an optical lens. An adjustable aperture is placed at the lens plane to limit the numerical aperture and perform spatial filtering (the column on right). The polarizers before and after the cell also perform polarization filtering for rejecting photons with a considerable polarization change as a result of scattering. The images on the top row of figure 44 are captured through the 'Kerr gating' mode of the apparatus. The polarizer after the Kerr cell is set orthogonal to the one before the cell, which means almost no light transmits through the Kerr gate when the switching beam is blocked. At the presence of the switching pulse, however, there is a 1 picosecond transmission window (figure 32), letting only the first group of transmitted photons which are not delayed more than 1ps through the scattering environment make their way to the CCD detector. All the images presented in figure 44 are acquired at a condition when no scattering cell is placed in the path of the imaging pulse. These images are just references to show how the system performs in an uncompromised regular condition.

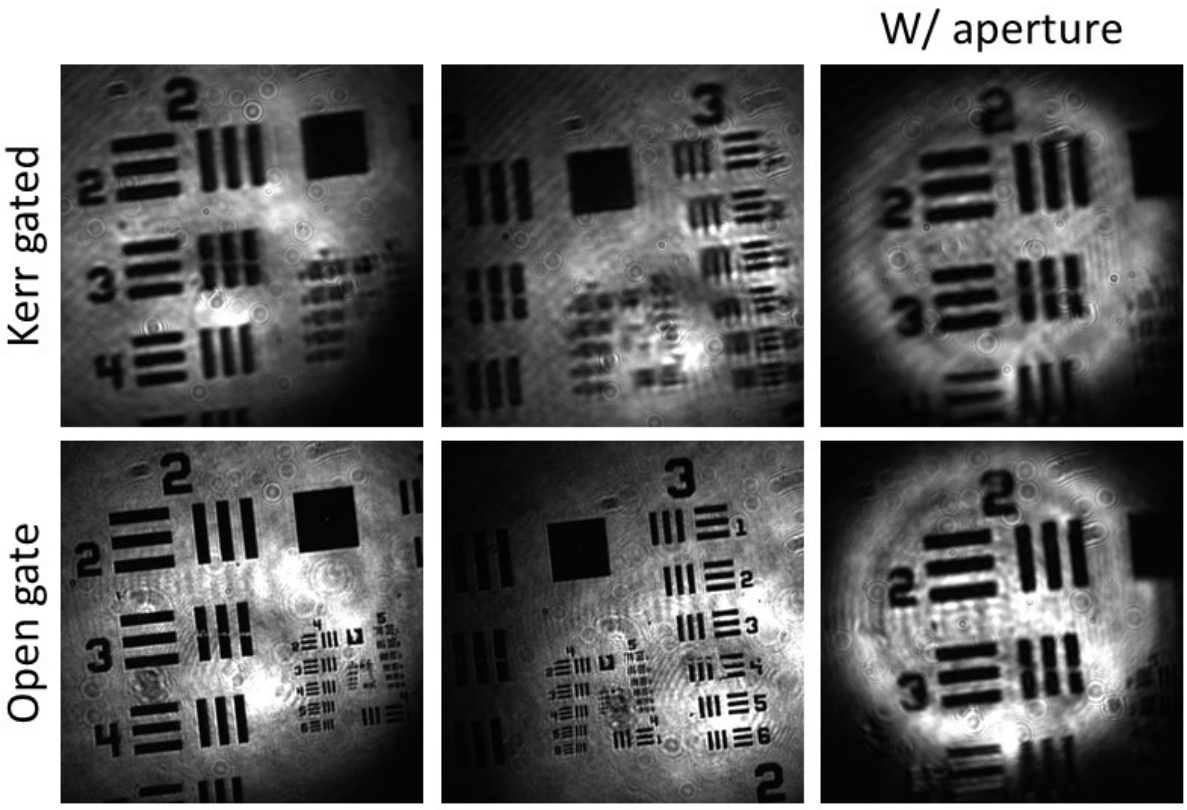

Figure 44- Kerr effect ballistic imaging performance in no scattering condition at 'open gate' and 'Kerr gated' modes.

The images made in open gate mode have clearly achieved better resolution. Smaller elements are resolved in open gate mode and edges of larges elements are sharper in these images. The resolution degradation in time gating mode is not a surprise as the numerical aperture is limited by the switching beam diameter at the Kerr cell. The transmission through the Kerr gate is proportional to the intensity of the switching beam at each point in the Kerr cell (chapter 5) and the switching beam intensity decays exponentially in the radial direction because of the Gaussian beam profile. Since the Kerr cell is placed at the Fourier plane of the lens (focal distance) the lower frequency components of the wave are transmitted through the center of the switching with higher transmission and the higher frequency components are transmitted further from the center with lower transmission

rate. This frequency dependent transmission acts like a low pass filter which reduces the numerical aperture of the imaging system in time gating mode and sacrifices the resolution and sharpness of the acquired image. When an aperture is used at the lens plane to reduce the numerical aperture of the imaging system (right column) to level comparable to that caused by the intensity effects of the gating pulse, the open gate and Kerr gated modes acquire images more similar in terms of edge sharpness. Since the aperture acts like a low pass filter itself, the low pass filtering inherent in Kerr gating mode has a smaller effect and makes less changes to the outcome.

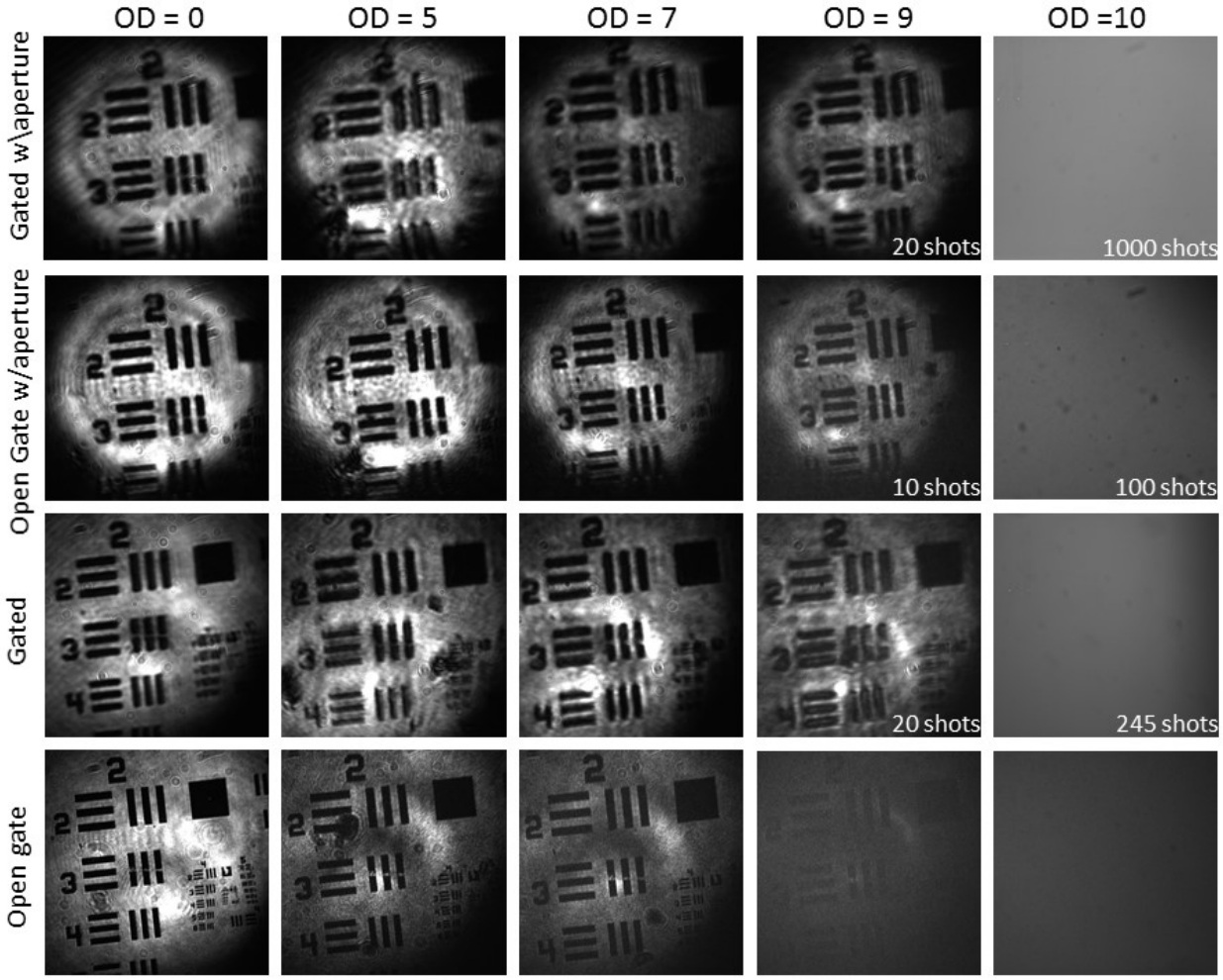

Figure 45- Kerr effect ballistic imaging of group 2 USAF resolution target through 0.6 micron scattering particles media of various optical depths at 'open gate' and 'Kerr gated' modes.

Figure 45 demonstrates images of the USAF resolution chart group 2 elements veiled behind glass cells containing hydrosols of 0.6 micron polystyrene particles with various optical depths. Gated mode images show better contrast compared to open gate mode especially in denser scattering conditions. However, the difference between gated and open gate mode when an aperture is used seems less significant, which indicates that most of the improvement in contrast of the images acquired through time gating mode is a result of its low pass nature rather than the 1 ps time gating. This natural low pass filtering effect of time gating has not been appreciated in the ballistic imaging literature. Figure 46 demonstrates similar results for the case of 6 micron scattering particles. As with the previous set of results, there is more significant improvement observable between gated and open gate mode when the aperture is removed from the lens plane. One way to improve the resolution of the Kerr gated imaging mode and resolve smaller features is to use a stronger optical lens for imaging with shorter focal lengths. Using the same switching beam profile means the instantaneous virtual aperture inside the Kerr cell remains the same size. Therefore, using a shorter focal length lens for imaging improves the effective numerical aperture of the imaging system inversely proportional to the imaging focal length. For a more complete evaluation, it is important to test smaller target elements, as Kerr effect ballistic imaging is believed to be more effective in harsh scattering conditions when other simpler filtering techniques such as spatial filtering are not sufficient. These smaller elements are examined in the following results.

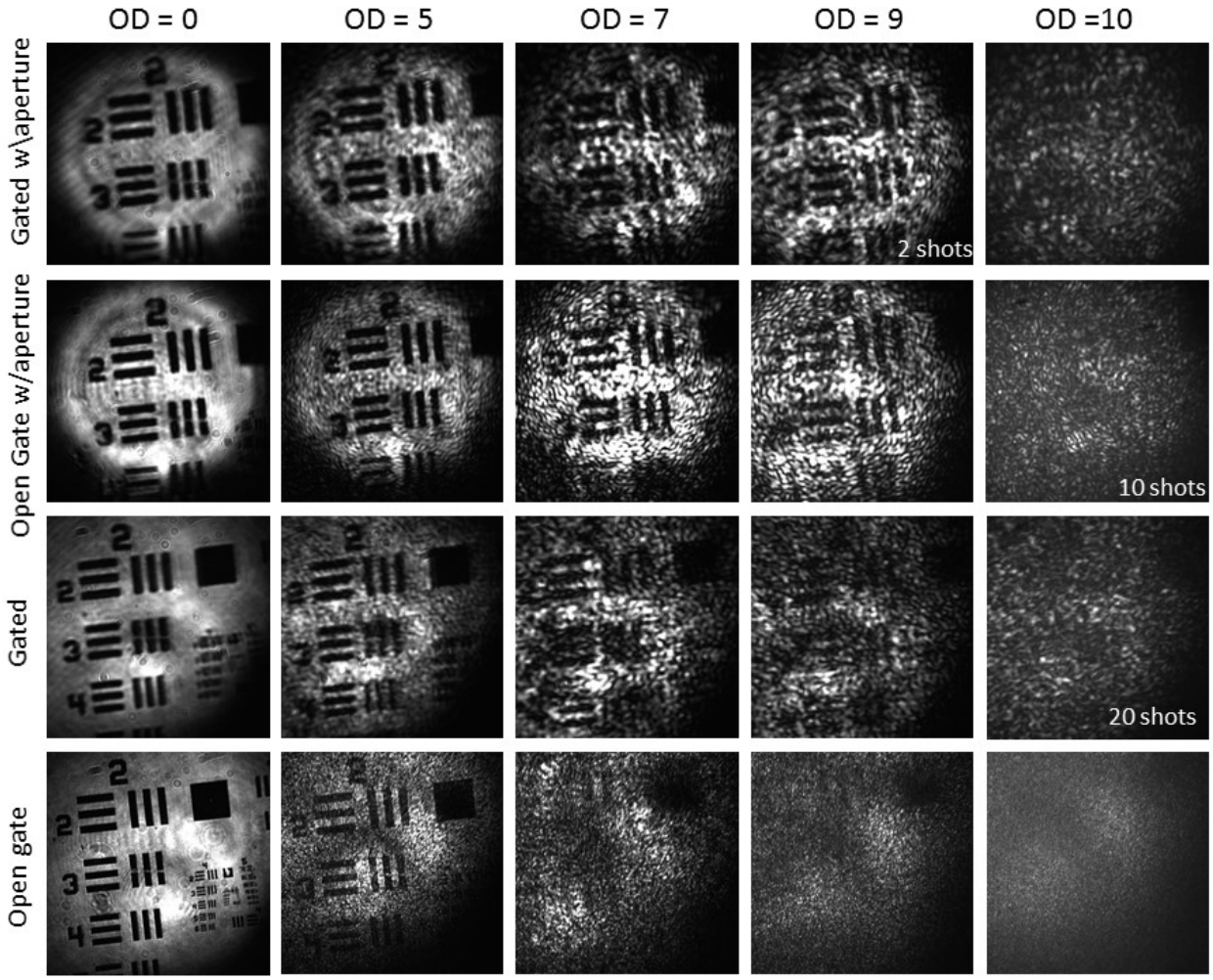

Figure 46- Kerr effect ballistic imaging of group 2 USAF resolution target through 6 micron scattering particles media of various optical depths at 'open gate' and 'Kerr gated' modes.

Images presented in figures 47 and 48 were captured using an optical lens with focal length of 100 mm in a 4f imaging setup which creates a numerical aperture twice as large as compared to the imaging system used in figures 45 and 46. Figure 47 illustrates results of Kerr effect ballistic imaging of group 4 on the USAF test target through 0.6 micron particles scattering cells in gated and open gate modes. In the case of no scattering and (OD = 0) the open gate mode clearly provides higher resolution and better contrast images. In moderate scattering (OD = 5) when the aperture is not used to limit the numerical aperture, gated mode shows better contrast compared to open gate mode even though in the open gate

case smaller elements are resolved with sharper and more recognizable edges. When an aperture is used in both modes, however, open gate mode still results in better contrast. In the high scattering condition (OD =7) when an aperture is not used the gated image has better contrast compared to the open gate image. When the aperture is used, both gated and open gate images are of about the same quality.

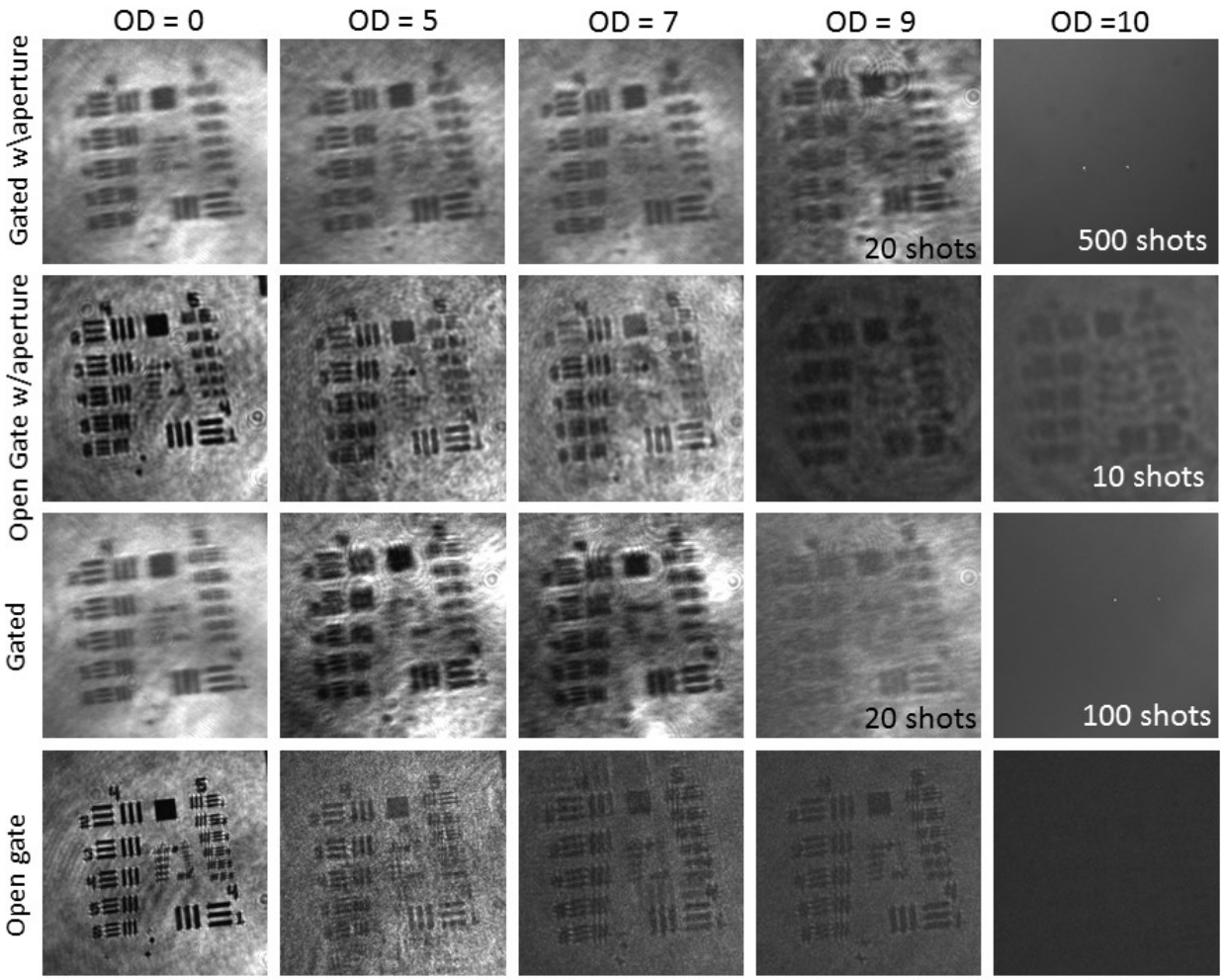

Figure 47- Kerr effect ballistic imaging of group 4 USAF resolution target through 0.6 micron scattering particles media of various optical depths at 'open gate' and 'Kerr gated' modes.

In harsh scattering (OD = 9) when an aperture is not used the chart elements are not resolved clearly in gated mode. With an aperture the gated image looks considerably

improved compared to the open gate image. In ultra-harsh scattering conditions (OD > 10) almost all the modes of the imaging system fail to resolve the target except for a vague shadow observable in the open gate with aperture mode. Figure 48 illustrates a similar comparison for 6 micron scattering particles and group 3 on the USAF chart. It is observable that in no and moderate scattering the open gate mode demonstrates better image quality while in high and harsh scattering conditions the target is more clearly resolved in gated images. In the ultra-harsh scattering environment again all modes of the imaging system fail to resolve the test target. These results show that in general Kerr effect ballistic imaging can be effective to partially overcome the multiple scattering noise in environments with optical depth between 7 to 10 with scatterers having particle size factors of 1.5-15.

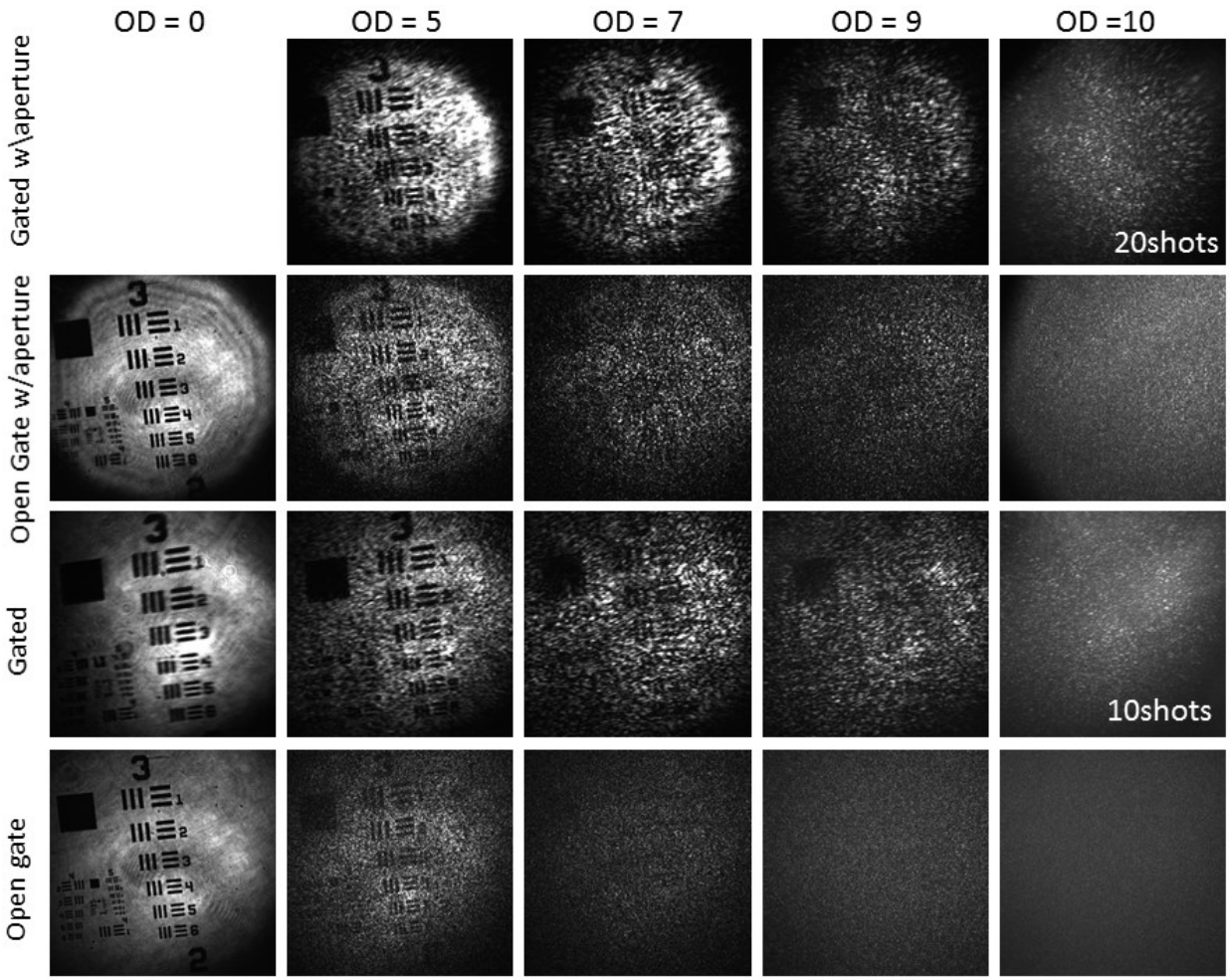

Figure 48- Kerr effect ballistic imaging of group 3 USAF resolution target through 6 micron scattering particles media of various optical depths at 'open gate' and 'Kerr gated' modes.

Ultra-short Pulsed Digital Holography versus Ballistic Imaging

Based on the results presented in this chapter so far, both ultra-short pulse off-axis digital holography and Kerr effect ballistic imaging were proven effective to partially overcome the multiple scattering noise caused when imaging through highly scattering media. In order to compare between these two techniques, images made from the same test targets and through the same scattering cells were made by both of these techniques. These images are illustrated in figures 49 through 51. Images illustrated in figure 49 are made from group 4 of the USAF test target through scattering cells containing 0.6 micron

particles. Ultra-short pulse off-axis digital holography images show clearly better contrast compared to Kerr effect ballistic images in this group of results. The time gate applied through coherence filtering in ultra-short pulse off-axis holography is on the order of the coherence length of the light source (100 fs), which is one order of magnitude shorter than the Kerr effect time gate (FWHM = 1.1 ps). This shorter time gate results in more effective filtering of the stretched imaging pulse in order to improve the signal to noise (multiple scattered) ratio. Images in figures 50 and 51 are made from group 3 and group 2 on the USAF test target scattered through hydrosols of 6 micron polystyrene particles. Images reconstructed from digital holograms still demonstrate better contrast compared to Kerr effect ballistic images especially in higher optical depths. The contrast advantage of reconstructed holograms over ballistic images is more significant for smaller scattering particles in figure 49 compared to larger scattering particles as were used in figures 50 and 51. As explained earlier in this chapter, 6 micron particles have much greater forward scattering lobes, which results in more speckle corruption in the recorded holograms. Speckles consist of higher frequency components compared to uniform noise, which makes the filtering process in numerical reconstruction less effective.

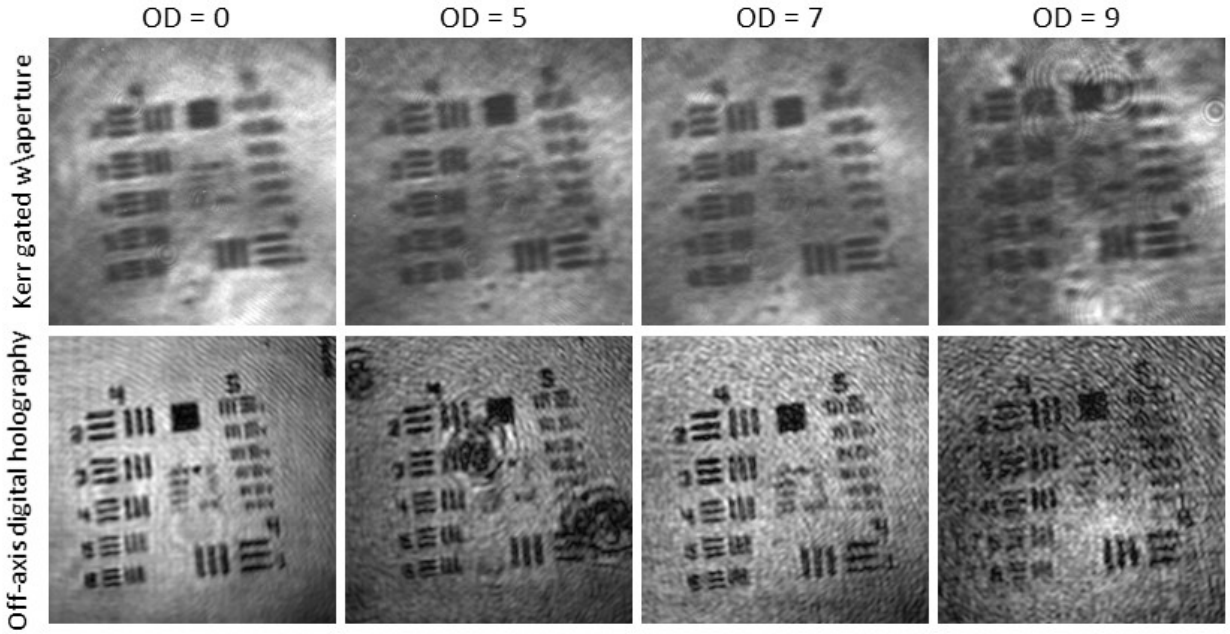

Figure 49- Ultra-short pulse off-axis digital holography and Kerr effect ballistic imaging of group 4 USAF resolution target through 0.6 micron scattering particles media of various optical depths.

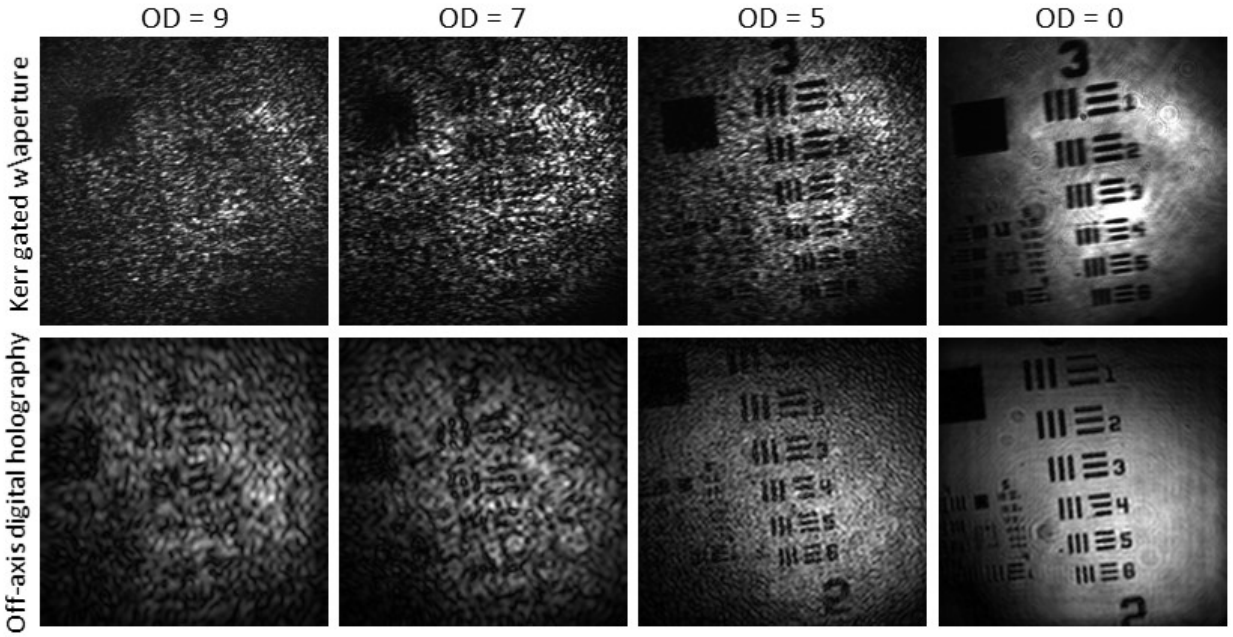

Figure 50- Ultra-short pulse off-axis digital holography and Kerr effect ballistic imaging of group 3 USAF resolution target through 6 micron scattering particles media of various optical depths.

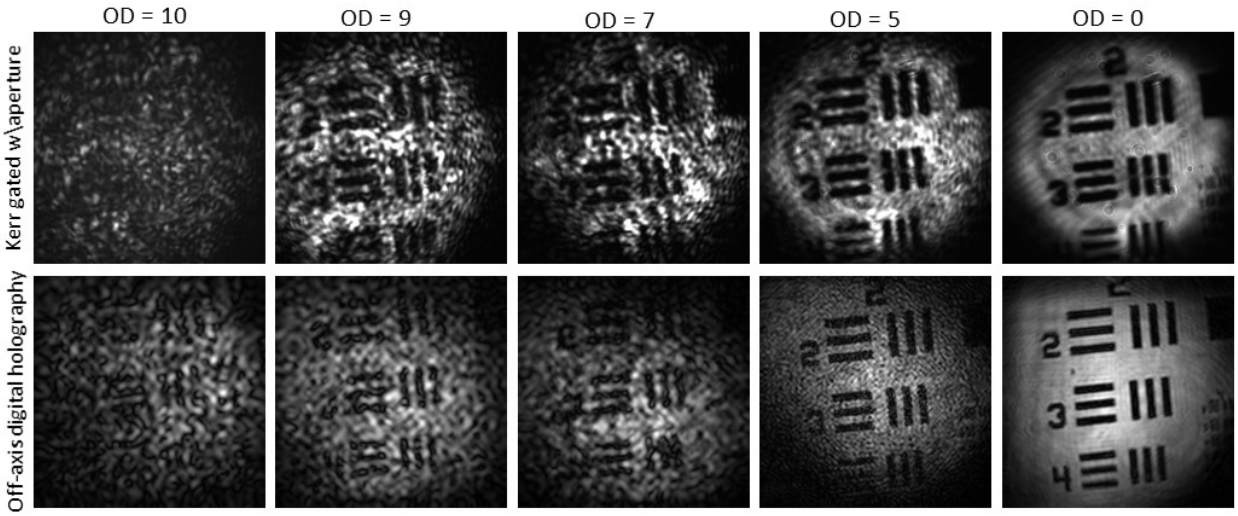

Figure 51- Ultra-short pulse off-axis digital holography and Kerr effect ballistic imaging of group 2 USAF resolution target through 6 micron scattering particles media of various optical depths.

CHAPTER 6

Summary and Conclusions

Imaging the formation region of dense sprays (e.g., Diesel sprays) is an important element to understand the fluid dynamic process of spray disintegration. Because of complicated nonlinear fluid dynamics governing equations in liquid phase disintegration, no theoretical solution to the process has been found to the date. Numerical solutions of the governing equations include substantial simplifying assumptions. Therefore, experimental results are required to validate the numerical simulations and their inherent simplifications. The optically thick cloud of droplets surrounding the formation region of dense sprays makes non-intrusive experimental data acquisition extremely difficult in this region. One major barrier for optical access to the formation region of dense sprays is the phenomenon of multiple scattering. That is, at least figuratively, most of the light photons which intrude into the formation region of dense sprays are bounced off the surrounding droplets so many times (multiple scattering noise) that they can no longer be used for forming an intelligible image of the liquid structure. Statistically, a few photons that have not been scattered by the surrounding droplets, and whose original characteristics (such as propagation direction) have not been altered significantly (signal) can be used to form a "ballistic" image of the liquid structure of the formation region. Filtering techniques are required, however, to filter out the multiple scattering noise and produce a signal to noise ratio sufficient for the detector to record an image. The simplest and most effective way to reduce the multiple scattering noise is spatial filtering. Reducing the numerical aperture of

the imaging system in order to filter high frequency noise helps to improve the signal to noise ratio because photons scattered widely are blocked in favor of those contained in the narrow solid angle around the optical axis. These near-axis photons have generally been scattered less frequently. The most important limitation of spatial filtering is sacrificing the resolution of the imaging system as the high frequency image components are removed, especially in severe scattering conditions.

Another way to filter out the multiple scattering noise, which is highly accredited in the dense sprays diagnostics literature, is to time gate the imaging signal. When an ultra-short laser pulse intrudes into a highly scattering medium its length stretches by the time it exits the scattering environment as a result of multiple scattering phenomena. The multiply scattered photons (corrupted photons) are therefore mostly in the tail of the output pulse, since they have travelled a longer path through the scattering medium as they are delayed from the bouncing off many droplets. The non-corrupted photons are mostly in the forehead of the output pulse, as they have travelled a shorter path through the scattering environment. Using an ultra-fast shutter, it is possible to only let the forehead of the output pulse proceed to the detector and to block the output pulse tail, thereby improving the signal to noise ratio. Carbon disulfide (CS_2) liquid is commonly used in glass window cells to construct an ultra-fast Kerr effect optical shutter using ultra-short pulsed Ti:Sapphire lasers. The transmission window of these Kerr effect shutters is limited to the relaxation time of CS_2 molecules (around 1 picosecond). Using numerical simulation of birefringence phenomenon a Kerr effect ballistic imaging setup was carefully designed and constructed at UC Irvine. The full width at half maximum (FWHM) transmission window of the apparatus

was measured to be 1.1 picoseconds, which matched the results of companion numerical simulations. The majority of the published literature on ballistic imaging in dense sprays does not provide a direct comparison between ballistic images and regular shadow imaging of the subject examples (e.g. Linne et al. 2005, Linne et al. 2006, Linne et al. 2010, Linne et al. 2013, Paciaroni 2004, Paciaroni et al. 2004). These published works present time-gated ballistic images of the subject sprays, but no regular shadow images are presented for comparison. In addition, some published work demonstrates comparison between ballistic imaging and regular imaging without careful reporting of the numerical aperture used in each case (e.g. Linne et al. 2009, and Mathieu et al. 2014). The contrast improvement shown in these works can be partially related to the smaller effective numerical aperture of the imaging system in time-gated mode considering that limiting the numerical aperture of imaging systems is specifically effective for reducing the scattering noise, particularly for relatively small scattering particles (e.g., 0.6 micron scattering particles used in Mathieu et al. 2014). Some published research studies have also claimed measured improvement contrast ratio of the ballistic images compared to the regular shadow images without demonstrating the images (e.g. Rahm et al. 2014, Rahm et al. 2015). The contrast ratio is not always a good measure of image quality and it is often difficult to relate contrast ratio improvement with visible image quality improvement. In this dissertation results of Kerr effect ballistic imaging through various scattering conditions were presented in both gated and open gate modes to provide a direct comparison and investigate the effectiveness of the technique. An adjustable aperture was used in the lens plane of the imaging system in both modes and results are presented, both in the presence of the aperture and when the aperture is removed, to demonstrate the effect of spatial filtering (limiting the numerical

aperture). The Kerr effect ballistic imaging apparatus was demonstrated to effectively improve the contrast and resolution of images captured from USAF test targets veiled behind scattering hydrosols of polystyrene particles with optical depths (OD) between 7 to 10 (harsh scattering condition). The image quality improvement, however, was not as significant as implied by the literature. Multiple scattering noise is solely reported as the barrier for imaging through highly scattering media in dense spray diagnostic literature. Results presented in this dissertation suggests however that, especially in case of ultra-harsh scattering conditions (OD > 10), the scattering medium becomes so dense that regardless of the multiple scattering, effective imaging of the targets veiled behind or inside the medium is not possible. For the case of relatively small ratio (< 20) of target features' sizes (around 60 micron for group 2 and 3 of USAF chart) to scattering particles size (e.g. 6 micron polystyrene particles) when the scattering environment is extremely dense (OD > 10) the scattering particles come so close to each other that they act like larger objects and they block the view of target features behind them even if all multiple scattering noise is filtered out. For the case of smaller scattering particles (e.g. 0.6 micron) as the number density of polystyrene particles in water becomes extremely high (OD > 10) the hydrosol acts more like a uniformly defusing medium (i.e., rather than as a scattering medium) with an index of refraction higher than that of the carrier liquid water, and there is no longer ballistic and snake photons at the forehead of the output pulse to be singled out and used to form an image of the imaging target.

Ultra-short pulse off-axis digital holography is an alternative technique, proposed in this dissertation, to image 3D structured targets surrounded by or veiled behind highly

scattering media. The 3D structure of the liquid core in the formation region of dense sprays is a good example of such imaging targets. Holography is an interference based wave optics technique which requires a coherent light source. The extremely short coherence length of ultra-short pulsed lasers (around 30 microns for 100 fs pulses) such as Ti:Sapphire amplifiers do not make them best choices for holographic imaging. The limited work that has been published on ultra-short pulse digital holography has focused on inline digital holography (Nicolas et al. 2007), as short coherence length light sources cause less difficulty for inline holography. Relatively recently, an attempt to integrate inline digital holography with Kerr effect time gating was made at UC Irvine (Trolinger et al. 2011). The light source used in the UC Irvine ballistic holography setup generated 10 ps duration pulses which are too long for effective ballistic imaging. Theoretical and experimental studies presented in this dissertation show that off-axis femtosecond digital holography is a more suitable choice for imaging through highly scattering media. Although very careful alignment is required for 100 fs pulses to properly record an off-axis digital hologram and while limited hologram size and achievable spatial resolution is caused by the ultra-short coherence length of the light source, the separation of the cross term in frequency domain, which takes place only in off-axis holography, creates an opportunity for ultra-short (100fs) coherence time-gating which is much more effective for imaging through moderate and harsh scattering conditions ($5 < OD < 10$) compared to the more standard 1 ps time-gate window in Kerr-effect time gating. The results presented in this dissertation demonstrate significant improvement of image contrast and spatial resolution for the case of imaging through smaller scattering particles (in order of magnitude of imaging light wavelength) compared to regular spatial filtered optical lens shadow imaging and Kerr

effect ballistic imaging. Due to larger forward scattering and speckle noise, in the case of larger scattering particles (around 10 times larger than the imaging wavelength) the image quality improvement is not as significant, but the gain is still considerable compared to Kerr effect time gating. Considering the unlimited depth of field of the holography setup proposed in this dissertation (i.e., where forward scattered light from the imaging target is used to form holograms), and recognizing the capability of reconstructing the target object field at different depths (3D), the ultra-short pulse off-axis digitally holography technique proposed in this dissertation was demonstrated to be a reliable choice for imaging 3D target structures such as intact liquid cores through highly scattering media.

Future Directions

Applying ultra-short pulse off-axis digital holography on atomizing sprays, such as in high pressure Diesel sprays, would help to characterize the technique under real conditions. Imaging through high-pressure environments requires dealing with additional difficulties such as pulse broadening which needs to be addressed in order to design an optimized 3D imaging apparatus for high pressure Diesel sprays. Numerical simulation of the digital holograms made through highly scattering media helps to study and optimize the technique more accurately. Monte Carlo simulations commonly used for modeling light propagation in scattering environments neglect the interference phenomenon, which is not an accurate assumption when using partially coherent light sources such as the ultra-short pulsed lasers used for Kerr effect ballistic imaging, especially when scattering particles have large forward scattering lobes. Neglecting interference makes Monte Carlo simulations in the format they are currently applied incapable of simulating holographic

imaging in turbid media. Therefore theoretical modifications are required to make the simulations results more reliable under realistic operating conditions.

BIBLIOGRAPHY

Berrocal E. (2006). Multiple scattering of light in optical diagnostics of the dense sprays and complex turbid media. PhD thesis, Cranfield University, Cranfield, UK.

Cai W., Powell C.F., Yue Y., Narayanan S., Wang J., Tate M.W., Renzi M.J., Ercan A., Fontes E., and Gruner S.M. (2003). Quantitative Analysis of Highly Transient Fuel Sprays by Timeresolved X Radiography, Appl. Phys. Lett., 2003, 83, 1671–1673.

Calba C., Mees L., Roze C., and Girasole T. (2008). Ultrashort pulse propagation through a strongly scattering medium: simulation and experiments, J. Opt. Soc. Am., 2008, A, 25**,** 1541.

Connon C.S., Dunn-Rankin D. (1996). Droplet Stream Dynamics at High Ambien Pressures, Atom. and Sprays, 1996, 6, 4, 485–497.

Demos S., Alfano R. (1996).Temporal gating in highly scattering media by the degree of optical polarization, Optics Letters 1996;21(2):161e3.

Faeth G. (1996). Spray combustion phenomena, Twenty-Sixth Simposium (International) on Combustion, 26:1596–1612.

Faeth G., Hsiang L.P., and Wu P.K. (1995). Structure and breakup properties of sprays, Int. J. Multiphase Flow, 21:99–127.

Falgout Z, Rahm M, Wang Z, Linne M. (2013). Ballistic imaging in the spray formation region for the ECN spray A, in: Proc ILASS Europe September 2013.

Galland P.A., Liang X., Wang L., Breiasacher K. L., Ho P., et al. (1995). Time-resolved optical imaging of jet sprays and droplets in highly scattering medium, in: Proc. ASME Heat Transfer and Fluids Engineering Divisions ;vol. HTD- 321. p. 585e8.

Idlahcen S., Rozé C., Méès L., Girasole T., Blaisot J.B. (2012). Sub-picosecond ballistic imaging of a liquid jet, Experiments in Fluids 2012;52:289298.

Kohse-Hoeinghaus K. and Jeffries J.B. (2002). Applied Combustion Diagnostics, Taylor & Francis, New York, 2002.

Kristensson E., Berrocal E., Aldén M. (2012). Quantitative 3d imaging of scattering media using structured illumination and computed tomography, Optics Express 2012;20(13):14437e50.

Labs J. and Parker T. (2006). Two-dimensional droplet size and volume fraction distributions from the near-injector region of high pressure diesel sprays, Atomization and Sprays, To appear.

Lefebvre A. (1989). Atomisation and Sprays, Taylor & Francis.

Linne M. (2013). Imaging in the optically dense regions of a spray: A review of developing techniques, Journal of Progress in Energy and Combustion Science 39 (2013) 403e440.

Linne M., Paciaroni M., Gord J., Meyer T. (2005). Ballistic imaging of the liquid core for a steady jet in cross flow, Applied Optics 2005;44(31):6627-34.

Linne M., Paciaroni M., Sedarsky D., Berrocal E., and I. M. (2006). Ballistic imaging of the liquid core in the dense spray region, PECS, paper in progress.

Linne M., Paciaroni M., Sedarsky D., Gord J., and Meyer T. (2005). Ballistic imaging of the liquid core for a jet in cross flow, Proceedings of the 18th ILASS-America (Institute for Liquid Atomization and Spray System).

Linne M., Rahm M., Falgout Z., Wang Z., Paciaroni M., Matlok S., et al. (2013). Correlation of internal flow and spray breakup for a fuel injector used in ship engines, in: The 8th US National Combustion Meeting 2013.

Linne M., Paciaroni M., Berrocal E., and Sedarsky D. (2009). Ballistic imaging of liquid break up processes in dense sprays, Proceedings of Combustion Institute 32 (2009) 2147-2161.

Linne M., Sedarsky D., Meyer T., Gord J., Carter C. (2010). Ballistic imaging of the flow in the interior of the near-field of an effervescent spray, Experiments in Fluids 2010;49(4):911-23.

Mathieu F., Reddenmann M.A., Palmer J., and Kneer R. (2014). Time-gated ballistic imaging using a large aperture switching beam, Optics Express Mar 2014;7058-7074.

Mulhem B., Khoja G., Fritsching U., and Schulte G. (2004). Photographic observation of breakup of hollow cone suspension sheet, Proceedings of the 19th ILASS-Europe (Institute for Liquid Atomization and Spray System).

Nicolas F., Coetmellec S., Brunel M., and Lebrun D., (2007). Supression of the Moire effect in sub-picosecond digital in-line holography, Optics Express Feb 2007; Vol.15, No.3; 887 -895.

Paciaroni M. (2004). Time-gated ballistic imaging through scattering media with application to liquid spray combustion. PhD thesis, Colorado School of Mines.

Paciaroni M., Linne M. (2004). Single-shot two-dimensional ballistic imaging through scattering media, Applied Optics 2004;43:5100e9.

Parker T.E., Duran S., Porter J. (2012). Ballistic imaging of sprays at diesel relevant conditions, in: ICLASS 2012, 12th Triennial International Conference on Liquid Atomization and Spray Systems, Heidelberg, Germany 2012.

Powell C.F., Yue Y., Poolab R., Wang J. (2000). Time-resolved measurements of supersonic fuel sprays using synchrotron X-rays, Journal of Synchrotron Radiation 2000;7:356e60.

Rahm M., Paciaroni M., Wang Z., Sedarsky D., Linne M. (2014), Optical Arrangements for Time-Gated Ballistic Imaging, Imaging and Applied Optics.

Rahm M., Paciaroni M., Wang Z., Sedarsky D., Linne M. (2015), Evaluation of optical arrangements for ballistic imaging in sprays, Optics Express Aug 2015;Vol. 23,No. 17;22444-22462.

Rizk N. (1976). Studies on liquid sheet disintegration in airblast atomizers. PhD thesis, Cranfield University.

Rossmeissl M., and Wirth K.E. (2004). Influence of the nozzle geometry on the atomization of superheated liquids, Proceedings of the 19th ILASS-Europe (Institute for Liquid Atomization and Spray System).

Ruff G., Sagar A., and Faeth G. (1989). Structure of the near-injector region of pressure atomized sprays, J.Prop.Pow, 7:221–230.

Schiller L. (1922). Untersuchungen ueber laminare und turbulente stromung. VDI Forshungsarbeit, 248.

Sedarsky D., Paciaroni M., Linne M., Gord J, Meyer T (2006). Velocity imaging at the fluid/gas interface of the liquid core in an atomizing spray, Optics Letters 2006;31(7):906e8.

Schmidt J., Schaefer Z., Meyer T., Roy S., Danczyk S., Gord J. (2009).Ultrafast time-gated ballistic-photon imaging and shadowgraphy in optically dense rocket sprays, Applied Optics 2009;48(4):B137-44.

Schnars U., Jueptner W. (2005). Digital Holography.Springer. ISBN: 3-540-21934-x

Sedarsky D., Paciaroni M., Linne M., Gord J., Meyer T. (2006). Velocity imaging at the fluid/gas interface of the liquid core in an atomizing spray, Optics Letters 2006;31(7):906e8.

Sirignano W.A. (1999). Fluid dynamics and transport of droplets and sprays. Cambridge University Press.

Sobol I. The Monte Carlo method. Chicago: The University of Chicago Press; 1974.

Suzzi D., Berg E., Pastor J., Bianchi G., and Tatschl R. (2004). Simulation of primary breakup of diesel jets by a hybrid method combining vof-calculations and the classical ddm rate approach with 3d cfd code, Proceedings of the 19th ILASS-Europe (Institute for Liquid Atomization and Spray System).

Toal V. (2011). Introduction to Holography. CRC press. ISBN: 978-1-4398-1868-8

Trolinger J.D. and Bachalo W.D. (1977). Particle Field Diagnostics Systems for High Temperature/Pressure Environments, presented at EPA/ERDA Symposium on High Temperature/Pressure Particulate Control, Washington D.C., September 20–21, 1977.

Trolinger J., Buckner B., Tomov I. , Van der Veer W. , Dunn-Rankin D. and Garman J. (2011). Probong dense sprays with gated, picoseconds, digital particle field holography, Int. Journ. Of spray and comb. Dynamics, 2011, Vol. 3, Number 4, p. 351-366.

Tseng L.K., Ruff G., and Faeth G. (1992). Effects of gas density on the structure of liquid jets in still gases, AIAA, 30:1537–1544.

Tyler F. (1933). Instability of liquid jets, Phylosophical Magazine, 16:504–518.